Microfabrication of Surface Electrode Ion Traps for Quantum Manipulation

by

Yufei Ge

M.E. Microelectronics and Optoelectronics
Nanjing University, 2005

B.S. Physics
Nanjing University, 2002

Submitted to the Department of Physics
in partial fulfillment of the requirements for the degree of

Master of Science in Physics

at the

MASSACHUSETTS INSTITUTE OF TECHNOLOGY

February 2015

Signature redacted

Author .....
Department of Physics
September 3, 2014

Signature redacted

Certified by .....
Isaac L. Chuang
Professor, Departments of Physics and EECS
Thesis Supervisor

Signature redacted

Accepted by .....
Krishna Rajagopal
Professor of Physics, Associate Department Head for Education

Microfabrication of Surface Electrode Ion Traps for Quantum Manipulation

by

Yufei Ge

Submitted to the Department of Physics
on September 3, 2014, in partial fulfillment of the
requirements for the degree of
Master of Science in Physics

Abstract

Trapped ions are a promising approach to quantum computation. This approach uses a qubit state which is the atomic state and quantum motional state of a trapped ion to encode information, and uses laser-ion interactions to manipulate the qubit state. A major obstacle to the realization of a practical ion trap quantum computer is decoherence. In trapped ion quantum computation experiments, decoherence is dominated by the uncontrolled heating of ion motional states. In this thesis, we present the detailed microfabrication of several series of surface electrode linear Paul traps made from different electrode materials, followed by the ion motional heating experiment results for these traps. We demonstrate that the ion motional heating strongly depends on fabrication process. In particular, we explore how grain size and grain orientation affect the ion motional heating rate.

This thesis is divided into two parts. In the first part, we describe the fabrication of gold, silver, aluminum and niobium traps from different processes, which results in various surface morphologies and grain structures. Ion motional heating rate measurements are then conducted both at cryogenic temperatures and at room temperature. We employ a physical model based on the fluctuating patch potential theory to explain the ion heating behavior. We use gold traps to study the temperature and frequency dependence of the ion heating. We use aluminum traps to study the ion heating dependence on the amorphous dielectric layer. And we use silver traps to study the ion heating dependence on the grain structure. These results suggest that excess ion heating could possibly be suppressed by suitable fabrication selection.

In the second part, we present the process of using SU8 to fabricate a multilayer surface electrode point Paul trap, which has the advantage of allowing ion height variation within the same trap and enables testing of the distance dependence of ion heating.

Thesis Supervisor: Isaac L. Chuang
Title: Professor, Departments of Physics and EECS

Acknowledgments

This thesis presents my research work in Quanta Lab, supervised by Prof. Isaac Chuang. There are many people to thank, and the work could not have been done without their help. First, I would like to thank Prof. Isaac Chuang for his guidance in my scientific work. He has given me opportunities and freedoms to test my ideas. He taught us to use wiki to keep a complete and accurate record of the experimental methods and data from which I benefited a lot. I am deeply impressed by his thoughtful insight and dedication to high standard. Jaroslaw Labaziewicz has been a patient and creative mentor. He has also had a profound impact on me. His determination, enthusiasm and creativity have influenced me a lot. I started ion trap fabrication in EML. Kurt Broderick deserves thanks for teaching me the art of microfabrication. He has the know-how to fix all the equipments in EML. And he is always eager to help and provided me with useful insight. I would also like to thank James Daley for his help provided in NSL. Peter Herskind, Tony Kim, Shannon Wang and Molu Shi deserve thanks for providing useful insights and helpful discussions. I would also like to thank Catherine Modica and she is the person who I can always turn to for help. I am so fortunate to have met you all at MIT.

Finally, to my family, I owe the most. My dad and mom have provided all of the support they can give. I also thank my husband Zhengcheng and my son Alex for their support and sacrifices.

Contents

1 Introduction **17**

1.1 Why Quantum Computation 19

1.2 Requirements for the Physical Implementation of Quantum Computation - DiVincenzo Criteria 20

1.3 Ion Trap Approaches to Quantum Computer 21

1.4 Prior Art about Trapped Ion Fabrication 22

1.5 Main Contributions to This Work 24

1.6 Outline of the Thesis 25

2 Surface Electrode Ion Traps and Experimental Demonstration of Them with Sr^+ Ion **27**

2.1 The Linear Paul Trap 27

2.1.1 Solution: The Mathieu Equation 30

2.2 Surface Electrode Linear Paul Trap 31

2.2.1 The Pseudo-Potential Approximation 32

2.3 Sr^+ Ion Energy Level Structure 33

2.4 Motional State of Ion Trap 35

2.5 Laser - Ion Interactions 35

2.5.1 Doppler Cooling 36

2.5.2 Resolved Sideband Cooling 37

2.6 Cryogenic Ion Trap Experiment Apparatus 39

2.6.1 Surface Electrode Linear Paul Trap Design and Geometry . . 39

2.6.2 Cryostat 42

2.6.3 Ion Source 43
2.6.4 RF 43
2.6.5 Laser and Optics 44

3 Microfabrication of Surface Electrode Ion Traps 45
3.1 Facilities Used for the Fabrication of Surface Electrode Ion Traps . . 45
3.2 Surface Electrode Ion Trap Substrate Preparation 46
3.3 Surface Electrode Ion Trap Fabrication 50
3.3.1 Lithography 50
3.3.2 Etching 52
3.3.3 Lift-off 55
3.3.4 Electroplating 58
3.3.5 Annealing 60
3.4 Trap Dicing and Packaging 63

4 Ion Motional Heating Rate and its Relation to Fabrication Processes 67
4.1 Ion Motional Heating Rate and Electric Field Noise 68
4.2 Sources of Electric Field Noise 70
4.2.1 Thermal Electronic Noise 70
4.2.2 Fluctuating Patch-Potential Noise 75
4.3 Ion Motional Heating Rate Dependence on Fabrication Process 82
4.3.1 Electrode Materials 83
4.3.2 Electrode Morphology 84

5 Ion Motional Heating Rate Measurement 85
5.1 Ion Motional Heating Rate Measurement Method 86
5.2 Gold Traps 88
5.3 Aluminium Traps 94
5.4 Silver Traps 96
5.5 Niobium Traps 100
5.6 Discussion 101

6 Fabrication of Multilayer Ion Traps with SU8 **103**

6.1 Surface Electrode Point Paul Trap 104

6.2 Multilayer Structure of Surface Electrode Point Paul Trap and Trap Design 107

6.3 Multilayer Point Paul Trap with SU8 Fabrication Process 109

6.3.1 Bottom Layer Electrode 110

6.3.2 SU8 Application 110

6.3.3 Soft Bake 111

6.3.4 Exposure 112

6.3.5 Post Exposure Bake 113

6.3.6 Development 114

6.3.7 Hard Bake 114

6.3.8 Top Layer Electrode Sputtering 114

6.3.9 Top Layer Electrode Patterning and Dry Etch 115

6.4 Fabrication Summary 116

7 Conclusions and Future Work **119**

List of Figures

2-1 Schematic of quadrupole potential 28

2-2 Schematic of a linear Paul trap with two end cap electrodes 29

2-3 Schematic of a planar geometry for linear Paul trap 32

2-4 Energy level diagram for $^{88}Sr^{+}$ ion 34

2-5 Schematic of surface electrode linear Paul trap tested in our experiment 40

2-6 Schematic of a liquid helium bath cryostat and picture of the 4K base plate 43

3-1 Schematic of a contaminant particle sticking to the substrate surface with the presence of the adsorbed hydrocarbons 47

3-2 A comparison of AFM tests on fused silica substrates cleaned by different methods 49

3-3 A comparison of SEM tests on the edge qualities of different electrode materials patterned by wet etch 54

3-4 Optical picture of electrode edges with uniform glows and SEM image of nano sized "bubble" zone that causes the uniform glows 56

3-5 Schematic of shadow effect 57

3-6 SEM images of NR9-3000PY used for lift-off 58

3-7 Electroplating setup for gold including cathode, anode, and plating bath 60

3-8 Optical microscope image and SEM image of an electroplated gold electrode 61

3-9 (a)Heating plate of the annealing oven with tungsten wire underneath. Samples are put on the heating plate for annealing. (b) Annealing oven with lid removed. The annealing oven will be kept in a vacuum chamber. Samples can be heated up to 800 °C in the oven. 62
3-10 SEM images of silver trap before annealing and after annealing 63
3-11 Photo of a niobium trap which is mounted and wire bonded in a CPGA with heating resistors and temperature sensor on trap surface 65

4-1 Skin depth for gold, silver, aluminum and copper subjected to electric fields of different frequencies both at room temperature and at cryogenic temperature 72
4-2 Grain size dependence of resistivity contribution from grain boundary scattering 74
4-3 Comparison of the temperature dependence of the resistivities ρ_i, ρ_{FS} and ρ_{MS} 75

5-1 Average motional quantum number versus delay time 87
5-2 Temperature dependence of the noisy electric field spectrum of 75 µm electroplated gold trap II 89
5-3 Temperature dependence of the heat capacity of solids 90
5-4 Temperature dependence of the noisy electric field spectrum of 75 µm electroplated gold trap I 91
5-5 Arrhenius temperature dependence of the noisy electric field spectrum of 75 µm electroplated gold trap I after cleaning in an ultrasonic bath 93
5-6 SEM photos of electroplated gold electrodes (a) before (b) after cleaning in an ultrasonic bath 94
5-7 Frequency dependence of ion heating at different temperatures on 75 µm electroplated gold trap II 95
5-8 Electric field noise dependence on the evaporated oxide thickness . . . 97
5-9 The ion-electrode distance dependence of the ion heating rate on four 760°C annealed silver traps 100

6-1 Schematic of a surface electrode point Paul trap with three concentric electrodes 104
6-2 Schematic diagram of the superposition of electric fields generated by the two RF electrodes 106
6-3 Eagle design that we sent to Hughes Circuits Company for a surface electrode point Paul trap 108
6-4 Mask design for the multilayer Point Paul trap with SU8 109
6-5 Fabrication flow diagram of a multilayer surface electrode point Paul trap with SU8 117
6-6 Optical picture of a multilayer surface electrode point Paul trap with SU8 118

List of Tables

5.1 Electric field noise spectrum of electroplated gold traps measured at different temperatures 92
5.2 Electric field noise of the aluminum traps with native oxide layer and with evaporated oxide layer of different thickness 96
5.3 Electric field noise of Au, Ag, Al, Nb ion traps 101

Chapter 1

Introduction

In classical information and computation theory, information is encoded in the classical state of a physical system. For example, in a classical computer, information is encoded in voltage levels as a bit which has two distinct values, either a one or a zero. However, the classical information theory developed by Turing [Tur36], Shannon [Sha48], and von Neumann [Neu55] has its limitation, since quantum phenomenon are not taken into account. The physical world is fundamentally quantum mechanical. Thus the classical information theory needs to be generalized to a theory which is based on quantum principles. In 1982, Richard Feynman first proposed the idea of a quantum computer [Fey82]. Since that work, quantum theory has a profound impact on our understanding of information and computation.

In a quantum computer, information is encoded in the quantum state of a physical system. Different from a classical bit, a qubit can exist not only in classical zero and one states, but also in a coherent superposition of both. This unusual property gives quantum information and computation various advantages over classical computation, such as quantum algorithm, quantum simulations and quantum cryptography.

Experimental physicists have proposed several physical systems to realize a quantum computer. These experimental approaches include Nuclear Magnetic Resonance (NMR) approaches [DGCH97, War97, GC97], ion trap approaches [CZ95], neutral atom approaches [DDJ00], cavity QED approaches [PGCZ], quantum optical approaches [AGWK99] and superconducting approaches [NPT99]. And small compu-

tations have been demonstrated on these systems.

A big obstacle to the realization of a practical quantum computer is decoherence. The quantum information encoded in qubit will be damaged when the system interacts with the surroundings. A quantum computer is much more fragile to the surrounding noises compared to a classical computer. Theoretical physicists have proposed quantum error correction schemes to correct the decoherence errors [Ste03]. Experimental physicists are also working on different schemes to protect the entanglement of the qubits and reduce the decoherence [MDRS12]. In ion trap approach, ion is trapped in a harmonic potential and decoherence is dominated by the uncontrolled heating of ion motional states. We hypothesize that the decoherence in ion trap depends on the fabrication process of the ion trap and can be reduced accordingly. To determine how the fabrication process affects ion heating rate, we prepared several batches of ion traps using different fabrication processes with different materials. Ion heating rates of these ion traps were measured for comparison. We found that an ion trapped in a microfabricated surface electrode ion trap is only tens of microns above the electrode surface, thus the ion heating rate is very sensitive to the surface properties, for example, the patch size, grain structure, surface adsorption, surface oxidation and surface contamination. All these surface phenomena are strongly related to the ion trap fabrication process. Therefore, we conjecture one can suppress the ion heating rate by developing a suitable fabrication process.

This chapter introduces ion trap approaches to quantum information processing and quantum computing and describes the contents of this thesis. Section 1.1 introduces the concept of a quantum computer and describes the advantages of a quantum computer over a classical computer. Section 1.2 describes the requirements for the physical implementation of a quantum computer. Section 1.3 reviews the history of ion trapping. Section 1.4 reviews the prior art about ion trap fabrication. Section 1.5 and Section 1.6 outline the main contents of this thesis and list my main contribution of this work.

1.1 Why Quantum Computation

In 1982, Feynman first proposed the idea of using a quantum computer as a quantum simulator to solve problems that will be exponentially hard to simulate on a classical computer [Fey82]. David Deutsch furthered this idea in 1989 by proposing a model of quantum Turing machine [Deu89]. In a classical computer, information is encoded in binary bits which are manipulated by binary Boolean logic gates. In a quantum computer, information is encoded in qubits which are executed by quantum gates through unitary transformations.

Unlike the binary bit which represents either a one or a zero, qubit can represent any superposition of zero and one state. The superposition can result in quantum parallelism. For a n-qubit system, 2^n states can exist simultaneously. Linear increase in the system size results in exponential increase in potential processing power. Another consequence of the superposition is the non-cloning property, which is the basis of the quantum cryptography.

Many efforts have been made to study the algorithm that can exploit the power of quantum computing. For example, Peter Shor's algorithm enables a quick factoring of large numbers, which has profound impact on cryptography [Sho94]. On a quantum computer, it takes time $\mathcal{O}\left(\log\left(N\right)^3\right)$ to factor an integer N, which is exponentially faster than the time $\mathcal{O}\left(e^{1.9(\log N)^{1/3}(\log\log N)^{2/3}}\right)$ that a classical computer takes using the best known classical algorithm. Lov Grover proposed another algorithm which enables a quantum computer to search an unsorted database with N entries in time $\mathcal{O}\left(\sqrt{N}\right)$ which is shorter than the time $\mathcal{O}\left(N/2\right)$ needed by a classical computer [Gro97].

1.2 Requirements for the Physical Implementation of Quantum Computation - DiVincenzo Criteria

Experimental physicists have been working on the physical realization of the quantum computer from many different routes. The routes are all based on the same fundamental quantum principles. A set of seven general criteria have been developed by David DiVincenzo and his coworkers to guide the search for physical implementation of quantum computation [DiV00].

1. Be a scalable physical system with well defined qubits
2. Be initializable to a pure state
3. Decoherence time is much longer than the gate operation time
4. Have a universal set of quantum gates
5. Have a qubit specific measurement capability
6. Have the ability to interconvert stationary and flying qubits
7. Have the ability to faithfully transmit flying qubits between specific locations.

The first five criteria are sufficient for quantum computing. The last two criteria are necessary for quantum communications.

A qubit can be represented by a well characterized two level quantum system, for example, pairs of energy levels of an ion, spin states of a quantum dot or polarizations of a photon. Qubits can mainly be initialized to pure states. Physical schemes such as a sequence of interactions need to be designed to realize these unitary transformations. After that, computation results can be measured, accessible to all qubits. However, qubits can not be separated from the environments. Decoherence time characterizes how a qubit interacts with its environment. Once the coherence is lost, the quantum computer will behave classically.

1.3 Ion Trap Approaches to Quantum Computer

In 1995, Cirac and Zoller first proposed a quantum computer based on trapped ions [CZ95]. Ion traps can meet most of the DiVincenzo criteria and thus are a promising candidate for quantum computing and quantum information processing.

A linear string of ions is trapped in a linear Paul trap inside a vacuum system. The spacing between ions is determined by a balance between the trap potential and the Coulomb interaction between two neighboring ions. A qubit is defined by two well characterized electronic states of an ion. Besides the internal qubit state, an ion in a harmonic trap has quantized motion. And ions tapped in the same trap interact via their Coulomb interaction, creating collective vibrational modes of the ion string - motional state quantum bus [CZ95].

Initialization of the internal qubit state is achieved by optical pumping. Initialization of external motional state to its ground state is accomplished by laser cooling [WI79]. The initialization process can be performed with extremely high fidelity ($> 99\%$) [CFRB06].

A quantum computation can be expressed as a sequence of unitary transformations, each acting on one or two qubits. Such unitary transformations can be realized by laser-atom interactions inducing couplings between qubit states or between qubit state and motional state. An arbitrary single qubit rotation is often done by magnetic dipole transitions or electric quadrupole transitions. Gate fidelity can be as high as $> 99\%$ [MMK$^+$96]. There are several schemes to realize two qubit entangling gates. A two qubit controlled-NOT quantum gate was first demonstrated with a single trapped ion, using two internal atomic states and two external motional states. The controlled-NOT gate is realized by applying Raman pulses in sequence [MMK$^+$95]. The controlled-NOT gate can also be realized between two ions. The qubit state of the first ion can be mapped onto the motional quantum bus with the use of laser, and then a gate operation is conducted between the motional quantum bus and the second ion qubit state. Thereby information is transferred between two ions through a shared motional quantum bus [LDM$^+$03]. The fidelity of these implementations can

be as high as $> 99\%$ [BKRB08].

The measurement of ion qubit state is accomplished by a quantum jump scheme [BZ88]. Photons emitted during quantum jumps will be collected by a photomultiplier tube (PMT) or a charge-coupled device (CCD).

The decoherence in ion trap is composed of qubit state decoherence and motional state decoherence. The decoherence time is fundamentally limited by the spontaneous emission time of qubit state, and is also affected by the unstable laser beam, fluctuating external magnetic fields, unstable RF drive frequency and amplitude in experiments [WMI+98]. Decoherence time of $\mathcal{O}(10^{-3})$ is experimentally achieved [TKK+00], which is much longer than the gate operation time.

1.4 Prior Art about Trapped Ion Fabrication

The ion trap has been shown as a promising building block for a practical quantum computer. However, the first ion trap was invented as a component of a mass spectrometer by Wolfgang Paul [PS53]. This 3 dimensional hyperbolic trap consists of two hyperbolic electrodes and a hyperbolic ring electrode half way between them. The metal electrodes are usually fabricated from stainless steel and the surfaces are machined using CNC lathe. Experimentally, the 3 dimensional hyperbolic ion trap has some variations, such as ring and fork trap and needle trap [Kie96]. The hyperbolic shape of the electrodes can provide perfect quadrupole potential. However, hyperbolic shaped electrodes are difficult to machine with precision. The Paul trap evolves to a linear ion trap consisting of four rods and two end caps. The circular metal rods are easy to fabricate and can provide a quadratic potential to a good approximation. All the ion traps mentioned above have bulk metallic electrodes, which makes the trap size can not be very small. The most easily used bulk material for electrodes is stainless steel. The electrode surfaces in the trapping region are carefully polished as good as possible with abrasive metal paste [Kir07]. There are some other material options for the electrodes, such as tungsten [DOS+06], beryllium-copper [PBIW96], molybdenum [TKK+00]. All these electrode materials have strong strength, non-

magnetic property, good thermal and electrical conductivity. Beryllium copper has an advantage of good metalworking, forming and machining quality. Molybdenum is a refractory metal of extreme hardness. Molybdenum also has another advantage that the work function of metal and oxide are identical [JC71].

So far, all the above ion traps are bulky and difficult to scale up to ion trap arrays. In order to overcome this obstacle, an alternative planar geometry for linear Paul trap was proposed [CBB+05]. This surface-mounted electrode geometry makes it possible for an ion trap to scale up to ion trap arrays and also enables the capability of building ion traps with microfabrication techniques. A straightforward variation of the four rod linear Paul trap is a multi-layer trap. This multi-layer geometry can further evolve to a single layer trap with electrodes all lying in a single plane.

The fabrication process can be divided into two classes: monolithic and non-monolithic. The non-monolithic processes involve assembling patterned substrates by mechanical clamping [TKK+00] or wafer bonding [MDH11]. Substrates could be alumina [BOV+09], ceramic layer [SHO+06] or silicon [Sti07] and be patterned by laser machining or deep reactive-ion etching (DRIE). Electrode materials can be evaporated, sputtered or electroplated.

The monolithic processes are more widely used. One simple example of the monolithic process is the printed circuit board (PCB). The substrate is a 800 μm thick Rogers 4350B with pre-coated copper foil [Rog]. Copper in the unwanted area is removed by mechanical milling or wet chemical etch. The Rogers substrate can be further milled to achieve a slot structure. The smallest feature size of the PCB process is 100 μm [BCL+07].

Smaller structures can be achieved with microfabrication techniques including lithography, sputtering, evaporation, electroplating, wet etching and dry etching. The first microfabricated ion trap was fabricated on a fused quartz substrate with 6 μm gold electroplated onto the patterned copper seed layer [SCR+06]. The first ion trap on silicon-on-insulator (SOI) substrate was reported by Leibfried [LKOW07]. The patterned substrate is first dry etched of the top silicon layer in an anisotropic way followed by an isotropic wet chemical etch of the oxide layer. Deposit a metal layer

(1 μm gold) on top to reduce the resistance of the trap electrode. Another scheme that also uses the SOI substrate was proposed by Stick [SHO+06]. A conductive ground aluminum layer is patterned on the SOI substrate with a thin insulator layer underneath, followed by the deposition of a thick structured insulator layer. Overhanging trap electrodes are then placed on top of the thick insulator layer. Vias are used to connect the static trap electrode and the ground layer. The thin insulator layer could be silicon oxide or silicon nitride. The thick insulator layer would usually be silicon oxide. The conductive electrode material can either be aluminum or semiconductor. In addition, a backside etch can be performed to create a slot in the substrate for optical access or ion loading [SHO+06].

1.5 Main Contributions to This Work

This thesis mainly consists of two parts. The first part is about fabricating surface electrode linear Paul traps from different electrode materials and using them to study the relationship between ion motional heating and fabrication process. I did all the ion trap fabrication in the Nanostructures Laboratory (NSL) and Exploratory Materials Laboratory (EML) at MIT. Eric Dauler helped me in growing niobium films. Paul Antohi, Waseem Bakr built the cryogenic ion trap testing apparatus. Jaroslaw Labaziewicz built the laser systems. Jaroslaw Labaziewicz did all the ion heating measurements in electroplated gold traps and annealed silver traps. Shannon Xuanyue Wang did the ion heating measurements in aluminum traps and niobium traps. To explain the ion heating measurement results, I proposed a physical model based on the fluctuating patch potential theory to take grain size and grain orientation into account. And several possible options are proposed to suppress the ion heating from the fabrication perspective. The second part of the thesis is about fabricating a multi-layer point Paul trap with SU8. Tony Hyun Kim proposed the scheme of applying two RF potentials to two RF electrodes in order to vary the ion height within the same trap. I fabricated the multi-layer trap in the Nanostructures Laboratory (NSL) and Exploratory Materials Laboratory (EML) at MIT.

1.6 Outline of the Thesis

The remainder of this thesis consists of two parts. The first part, including Chapter 2, Chapter 3, Chapter 4 and Chapter 5, describes in detail the surface electrode ion trap fabrication process, the ion heating rate measurement and the relationship between them. The surface electrode ion traps discussed in the first part only have one-layer electrodes on insulating substrates. The second part, Chapter 6, describes in detail the fabrication process designed for multi-layer ion traps. The multi-layer ion traps provide more novel possibilities for the realization of a large scale quantum computer.

Chapter 2 first describes the theory of the linear Paul trap and the surface electrode linear Paul trap. Then according to the DiVincenzo criteria for ion trap approaches, a qubit state stored in a Strontium ion, ground state initialization, quantum gate operation and qubit measurement are presented. Finally, the geometry of our surface electrode linear Paul traps and their testing apparatus are covered.

Chapter 3 is about the microfabrication of surface electrode ion traps. This chapter describes the substrate preparation and the electrode fabrication in detail, followed by the ion trap dicing and packaging.

Chapter 4 is about the ion motional heating rate and its correlation with fabrication processes. In trapped ion quantum computation experiments, decoherence is dominated by the uncontrolled heating of ion motional states. This chapter begins by describing how the ion is heated due to the noisy electric field, including the thermal electronic noise and the fluctuating patch-potential noise. An extended patch potential model is proposed trying to explain the different ion motional heating behaviors we have observed in our ion heating measurements.

Chapter 5 first describes the ion motional heating rate measurement method. Then it presents experimental measurement results of the electric field noise in several batches of ion traps fabricated using different fabrication processes from different materials. This chapter concludes with a discussion about the sensitivity of the ion heating rate to the surface properties, for example, the patch size, grain orientation, surface adsorption, surface oxidation and surface contamination, which are strongly

related to the ion trap fabrication process.

Chapter 6 first introduces a variation of the linear Paul trap - surface electrode point Paul trap. This chapter describes the multi-layer structure and fabrication challenges of the point Paul trap, followed by the fabrication process in detail.

Chapter 7 concludes with a brief summary of the fabrication of surface electrode linear Paul traps made from different electrode materials. Using the physical model based on the fluctuating patch potential theory, we discuss our ion motional heating experimental results and an outlook on future work in this direction.

Chapter 2

Surface Electrode Ion Traps and Experimental Demonstration of Them with Sr^+ Ion

The linear Paul trap was first proposed in 1953 for trapping ions with oscillating electric field [PS53]. Such a quantum system has been shown promising in the realization of a quantum computer [CZ95]. In this chapter, we first give a general overview of linear Paul trap in Section 2.1. By using Mathieu equation, the ion motion is demonstrated to include both slow secular motion and fast micromotion. The surface electrode linear Paul trap is then introduced in Section 2.2 and its ion motion calculated using pseudo-potential approximation. Section 2.3 and Section 2.4 describe the well defined qubit with Strontium ion. Section 2.5 presents how ion and laser interact to achieve ground state initialization, quantum gate operation and qubit measurement. Finally, the geometry of our surface electrode ion traps and their testing apparatus are described in Section 2.6.

2.1 The Linear Paul Trap

The simplest way to trap a charged particle is to place it in a parabolic potential, which for an electric potential corresponds to an electric quadrupole Φ as shown in

Figure 2-1. In Cartesian coordinates

$$\Phi = \frac{\Phi_0}{2r_0^2}\left(\alpha x^2 + \beta y^2 + \gamma z^2\right) \tag{2.1}$$

where Φ_0 is the applied potential, and r_0 is the distance from the electrode to the center of the trap. In free space, the Laplace equation of the electrostatic potential must equal to zero $\Delta\Phi = 0$. Thus we get $\alpha + \beta + \gamma = 0$.

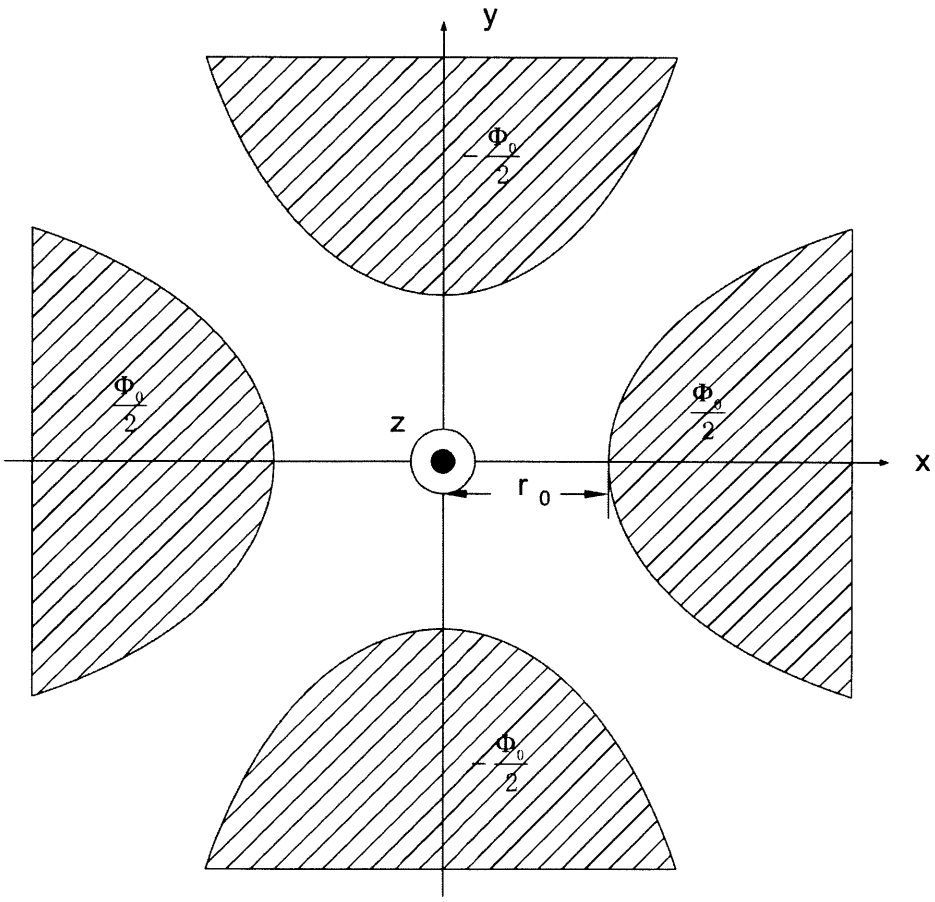

Figure 2-1: Schematic of a quadrupole potential. Φ_0 is the applied potential, and r_0 is the distance from the electrode to the center of the trap.

In the case $\alpha = -\beta$ and $\gamma = 0$,

$$\Phi = \frac{\Phi_0}{2r_0^2}\left(x^2 - y^2\right) \tag{2.2}$$

It is obvious that the ion will loose confinement in the y direction. This can be avoided if a periodic potential is applied. Figure 2-2 shows the schematic drawing of a linear Paul trap [Pau90]. Electrodes 1 and 3 are carrying a RF voltage V_0 with driving frequency Ω and a DC bias U_0, and electrodes 2 and 4 are grounded. Two end cap electrodes are carrying a DC voltage U_{endcap}. The radial quadrupole potential is thus

$$\Phi\left(x, y, t\right) = \frac{1}{2}\left[V_0 \cos\left(\Omega t\right) + U_0\right]\left(1 + \frac{x^2 - y^2}{r_0^2}\right) \tag{2.3}$$

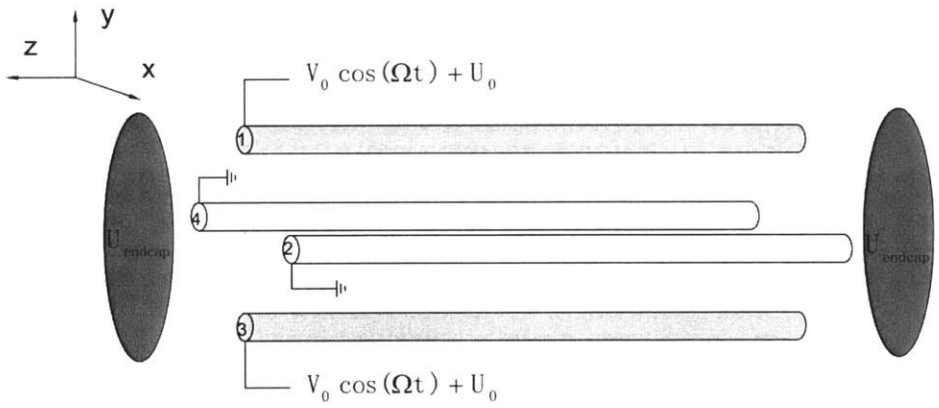

Figure 2-2: Schematic of a linear Paul trap with two end cap electrodes. Electrodes 1 and 3 are carrying $V_0 \cos\left(\Omega t\right) + U_0$. Electrodes 2 and 4 are grounded. Two end cap electrodes are carrying U_{endcap}.

Given that potential, the equation of motion for an ion with mass m and charge Q is:

$$\begin{aligned} \frac{\mathrm{d}^2 x}{\mathrm{d}\tau^2} + \left[a_x - 2q_x \cos\left(2\tau\right)\right] x = 0 \\ \frac{\mathrm{d}^2 y}{\mathrm{d}\tau^2} + \left[a_y - 2q_y \cos\left(2\tau\right)\right] y = 0 \end{aligned} \tag{2.4}$$

where $a_x = -a_y = \frac{4QU_0}{mr_0^2\Omega^2}$, $q_x = -q_y = \frac{2QV_0}{mr_0^2\Omega^2}$ and $\tau = \frac{\Omega t}{2}$.

Equation 2.4 is the canonical form for Mathieu's differential equation [Mat68]. Let us solve Mathieu's equation in both x and y direction and combine the results. For $a_{x,y} = 0$ (there is no DC bias U_0 at the four rod electrodes), the ion is trapped when $0 < |q_{x,y}| \leq q_{max} = 0.908$ [Mac47].

In z direction, two static potential U_{endcap} are applied to confine the ion axially. In this case, $\alpha = \beta = -\frac{1}{2}$ and $\gamma = 1$. The static electric quadrupole potential is

$$\phi(x, y, z) = \frac{\epsilon U_{endcap}}{Z_0^2}\left[z^2 - \frac{1}{2}\left(x^2 + y^2\right)\right] \tag{2.5}$$

where ϵ is a geometrical factor which is smaller than 1. Z_0 is the distance between the trap center and the end cap electrode.

Taking both the strong RF electric quadrupole potential and the weak static electric quadrupole potential into account and letting $U_0 = 0$, the final equation of motion for an ion with mass m and charge Q is:

$$\frac{\mathrm{d}^2 u_i}{\mathrm{d}t^2} + [a_i - 2q_i \cos(\Omega t)]\frac{\Omega^2}{4}u_i = 0 \qquad i = x, y, z \tag{2.6}$$

where $u_i\,(i = x, y, z)$ represent x, y and z coordinates.

$$a_x = -a_y = \frac{1}{2}a_z = \frac{4Q\epsilon U_{endcap}}{mZ_0^2\Omega^2} \tag{2.7}$$

$$q_x = -q_y = \frac{2QV_0}{mr_0^2\Omega^2}, q_z = 0 \tag{2.8}$$

2.1.1 Solution: The Mathieu Equation

When $|a_i| \ll 1$ and $|q_i| \ll 1$, the first order solution to Equation 2.6 is [Flo83]

$$u_i(t) \approx u_{1,i}\cos(\omega_i t)\left[1 - \frac{q_i}{2}\cos(\Omega t)\right] \tag{2.9}$$

where $\omega_i \cong \frac{\Omega}{2}\sqrt{a_i + \frac{1}{2}q_i^2}$.

The ion trajectory is the sum of the slow secular motion at frequency ω_i and the fast micromotion at the RF frequency Ω. The secular frequency ω_i is determined by

the values of a_i and q_i and by the frequency of the driven RF Ω. Thus the ion can see a harmonic potential in all three dimensions. Since $|q_i| \ll 1$, the micromotion has a much smaller amplitude than the secular one.

Equation 2.6 describes the case when there is no static stray electric field. However, in an actual ion trap experiment, a bias field cannot be avoided. Taking account the bias field $\vec{E}_{stray}$, the equation of motion for an ion with mass m and Q can be written as

$$\frac{\mathrm{d}^2 u_i}{\mathrm{d}t^2} + [a_i - 2q_i \cos(\Omega t)] \frac{\Omega^2}{4} u_i = \frac{QE_{stray,i}}{m} \qquad i = x, y, z \tag{2.10}$$

Similarly, the first order solution to Equation 2.10 is [BMB+98]

$$u_i(t) \approx u_{1,i} \cos(\omega_i t) \left[1 - \frac{q_i}{2} \cos(\Omega t)\right] + \frac{QE_{stray,i}}{m\omega_i^2} + \frac{QE_{stray,i}}{m\omega_i \Omega} \cos(\Omega t) \tag{2.11}$$

The presence of stray bias field changes the average ion position and increases the micromotion, however, it does not change the secular motion amplitude. This excess micromotion which is different from the intrinsic one can be avoided by applying compensation potentials.

2.2 Surface Electrode Linear Paul Trap

As mentioned in Section 1.4, this four rod linear Paul trap has limitations in scaling up to a practical quantum computer. An alternative planar geometry for the linear Paul ion trap was proposed [CBB+05]. In this surface mounted electrode geometry, all RF and DC electrodes lay in the same plane as shown in Figure 2-3. The four rod geometry is deformed into five wire design. The five wires are of alternating potentials (DC, RF, GND, RF, DC). The quadrupole potential in Equation 2.3 is revised. We induce the pseudo-potential approximation to characterize the the trapping potential.

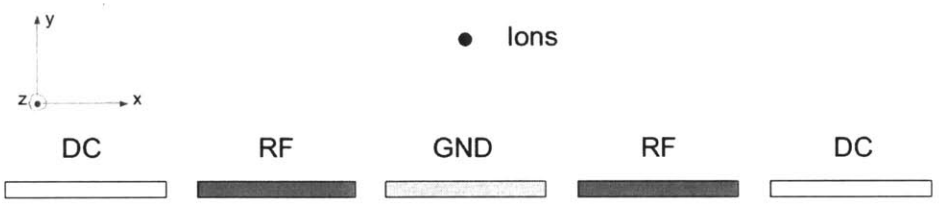

Figure 2-3: Schematic of a planar geometry for the linear Paul trap. The five electrodes in the sequence of DC, RF, GND, RF and DC lay in the same plane. Ions are trapped above the center GND.

2.2.1 The Pseudo-Potential Approximation

In a linear Paul trap, the ion is confined by a combination of oscillating potential V_{RF} at frequency Ω and a static potential U_{dc}. When RF voltage V_{RF} and DC bias U_{dc} are applied, the total electric potential is

$$\phi(\vec{u}, t) = V_{RF}\phi_{RF}(\vec{u})\cos(\Omega t) + \sum_n U_{dc,n}\phi_{dc,n}(\vec{u}) \tag{2.12}$$

where ϕ_{RF} and $\phi_{dc,n}$ are the shape functions of trap electrodes.

At the trap center, the gradient of both ϕ_{RF} and ϕ_{dc} is zero. The total electric potential can be expanded to the second order [Deh67].

$$\phi(\vec{u}, t) = \frac{V_{RF}\cos(\Omega t)}{2}\sum_{i,j}\left(\frac{\partial^2\phi_{RF}}{\partial u_i \partial u_j}\right)u_i u_j + \sum_n \frac{U_{dc,n}}{2}\sum_{i,j}\left(\frac{\partial^2\phi_{dc,n}}{\partial u_i \partial u_j}\right)u_i u_j \tag{2.13}$$

Thus the oscillating part $\cos(\Omega t)$ is averaged. We can rewrite the equation of motion for the trapped ion and get a similar canonical form of vector Mathieu's equation

$$\frac{\mathrm{d}^2\vec{u}}{\mathrm{d}\tau} + [a - 2q\cos(2\tau)]\,\vec{u} = 0 \tag{2.14}$$

where

$$a_{ij} = \frac{4QU_{dc}}{m\Omega^2}\left(\frac{\partial^2\phi_{dc}}{\partial u_i u_j}\right) \tag{2.15}$$

$$q_{ij} = -\frac{2QV_{RF}}{m\Omega^2}\left(\frac{\partial^2\phi_{RF}}{\partial u_i u_j}\right) \tag{2.16}$$

When $|a_{ij}| \ll 1$ and $|q_{ij}| \ll 1$, the mathematical solution for Equation 2.12 is the secular potential

$$\psi(x,y,z) = \frac{Q^2V_{RF}^2}{4m\Omega^2}\left|\nabla\phi_{RF}(x,y,z)\right|^2 + \sum_i QU_{dc,i}\phi_{dc,i}(x,y,z) \tag{2.17}$$

If the ion is trapped in an ion trap with complicated geometry, we use charged particle optics(CPO) program [CPO] to calculate the shape functions $\phi_{RF}(x,y,z)$ and $\phi_{dc}(x,y,z)$ of trap electrodes when RF and DC potentials are applied. Then the pseudo-potential approximation is induced to determine the secular potential and thus the secular frequencies and trap depth.

2.3 Sr^+ Ion Energy Level Structure

According to the DiVincenzo criteria in Section 1.3, a well characterized qubit is required to build a physical quantum computer. In ion trap approaches, qubit levels are usually chosen to be either two hyperfine levels in the electronic ground state or a ground state and an excited state of a weakly allowed optical transition. Several ions have been used and demonstrated by different groups, such as $^9Be^+$ [WMI+98], $^{40}Ca^+$ [RZR+99], $^{88}Sr^+$ [Ber02] and $^{111}Cd^+$ [DHL+04]. In our experiment, $^{88}Sr^+$ is used. ^{88}Sr is stable and has a nature abundance of 82.6% [Lid05]. The $^{88}Sr^+$ ion has one valence electron and no nuclear spin, thus it is hydrogen like and has a simple energy structure. More importantly, the relevant transitions are easily accessible with laser diodes, which enables the following ion manipulations by laser. Figure 2-4 shows the energy level structure of $^{88}Sr^+$ ion, and its relevant transition wavelengths.

According to the selection rule, transition $5^2P_{1/2} \rightarrow 5^2S_{1/2}$, $5^2P_{1/2} \rightarrow 4^2D_{3/2}$,

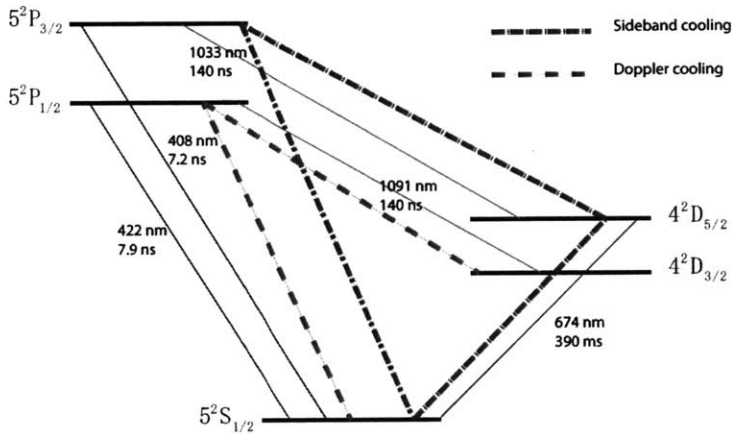

Figure 2-4: Energy level diagram for $^{88}Sr^+$ ion. 422 nm and 1091 nm transitions are used for Doppler cooling, shown in grey. Sideband cooling transition is shown in green. Transition $5^2P_{1/2} \rightarrow 5^2S_{1/2}$, $5^2P_{1/2} \rightarrow 4^2D_{3/2}$, $5^2P_{3/2} \rightarrow 5^2S_{1/2}$ and $5^2P_{3/2} \rightarrow 4^2D_{5/2}$ are all electric dipole transitions and the excited states have very short lifetimes [GJ91].

$5^2P_{3/2} \rightarrow 5^2S_{1/2}$ and $5^2P_{3/2} \rightarrow 4^2D_{5/2}$ are all allowed electric dipole transitions and the excited states have very short lifetimes [GJ91]. Transition $5^2P_{1/2} \rightarrow 5^2S_{1/2}$ and $5^2P_{1/2} \rightarrow 4^2D_{3/2}$ are used for Doppler cooling and ion detection. Transition $4^2D_{5/2} \rightarrow 5^2S_{1/2}$ is a forbidden electric quadrupole transition and $4^2D_{5/2}$ has a long lifetime (390 ms) [LWGS05]. This transition used as the qubit transition is for qubit manipulations, in addition, it can also be used for sideband cooling.

When the Sr^+ ion absorbs a 422 nm photon, it will be excited from $5^2S_{1/2}$ to $5^2P_{1/2}$ and then spontaneously decay back to the ground state $5^2S_{1/2}$ emitting a 422 nm photon. The overall result of the absorption and emission process is to reduce the speed of the ion. However, when the Sr^+ ion is in $5^2P_{1/2}$ state, it has a probability of 1/14 to decay to $4^2D_{3/2}$, thus 1092 nm laser is used to repump the ion back to $5^2P_{1/2}$ state. This process can also be used for ion internal state detection. Only if the ion is in the ground state, it will scatter a 422 nm photon collected by the photo-multiplier tube(PMT).

The ion is excited from $5S_{1/2}\,(m = -1/2)$ to $4D_{5/2}\,(m = -5/2)$ coherently by a π pulse on the red sideband of the 674 nm laser, followed by an optical pumping from $4D_{5/2}\,(m = -5/2)$ to $5P_{3/2}\,(m = -3/2)$ using 1033 nm laser (where m is the angular

momentum quantum number). The ion then preferentially decays back to the ground state $5S_{1/2}$ (m $= -1/2$). The result of this process is changing the phonon number by 1.

2.4 Motional State of Ion Trap

As shown in Section 2.1, the amplitude of the micromotion is much smaller than the secular motion and thus can be neglected. The trapped ion with mass m can be described by a simple harmonic oscillator.

The Hamiltonian for the harmonic oscillator oscillating at frequency ω_ν is

$$H_0 = \hbar\omega_\nu \left(a^\dagger a + \frac{1}{2}\right) \tag{2.18}$$

where $a^\dagger$ and a are the raising and lowering operators. The position of the ion can be written as

$$x = x_0(a + a^\dagger) \tag{2.19}$$

where $x_0 = \sqrt{\frac{\hbar}{2m\omega_\nu}}$ is the characteristic length scale of the harmonic motion.

2.5 Laser - Ion Interactions

Let us approximate the internal electronic structure of an ion by a two-level system with levels $|g\rangle$ and $|e\rangle$ of energy difference $\hbar\omega_{eg}$. When the ion is trapped and interacts with a single mode coherent light at frequency ω_L, the Hamiltonian has two parts, $H = H_0 + H_I$, and

$$H_0 = \hbar\omega_{eg}\sigma^z + \hbar\omega_\nu \left(a^\dagger a + \frac{1}{2}\right) \tag{2.20}$$

where $\sigma^z = \frac{1}{2}\left(|e\rangle\langle e| - |g\rangle\langle g|\right)$. The laser-atom interaction Hamiltonian can be written as

$$H_I = \frac{\hbar\Omega_{(Rabi)}}{2}\left(|e\rangle\langle g| + |g\rangle\langle e|\right)\left(e^{i(\vec{k}_L\cdot\vec{x}-\omega_L t+\phi)} + c.c\right) \tag{2.21}$$

and

$$\Omega_{(Rabi)} = \frac{eE_0}{\hbar}|\langle e|\vec{r}_e \cdot \hat{\epsilon}|g\rangle| \tag{2.22}$$

where $\vec{k}_L$ is the wave vector of light. ω_L is the light frequency. $\vec{x}$ is the relative position of the ion to the trap. And ϕ is the phase of light. E_0 is the electric field amplitude. $\vec{r}_e$ is the relative position of the electron to the nucleus. $\hat{\epsilon}$ is the light polarization.

By doing the Rotating Wave Approximation (RWA), H_I is rewritten as

$$H_I = \frac{\hbar\Omega_{(Rabi)}}{2}\left(|e\rangle\langle g|e^{-i\delta t}e^{i(\vec{k}_L\cdot\vec{x}+\phi)} + |g\rangle\langle e|e^{i\delta t}e^{-i(\vec{k}_L\cdot\vec{x}+\phi)}\right) \tag{2.23}$$

where $\delta = \omega_L - \omega_{eg}$.

2.5.1 Doppler Cooling

We can treat Equation 2.23 classically. As mentioned in Section 2.1, the trajectory of the ion consists of the secular motion and the micromotion. $x \approx x_0\cos(\omega_\nu t)$ when $|q| \ll 1$.

$$e^{ik_Lx} = e^{ik_Lx_0\cos(\omega_\nu t)} = J_0(k_Lx_0) + iJ_1(k_Lx_0)\,e^{\pm i\omega_\nu t}... \tag{2.24}$$

where $J_n\,(n = 0, 1, 2...)$ are Bessel functions.

When considering Doppler cooling, we only take into account $J_0(k_Lx_0)$ part.

The population of the excited state can be written as [MvdS99]

$$\begin{aligned}\rho_{ee}(\delta) &= \frac{1}{2}\frac{\Omega^2_{(Rabi)}J_0^2(k_Lx_0)}{\Omega^2_{(Rabi)}J_0^2(k_Lx_0) + 2\delta^2 + \Gamma^2/2} \\ &\approx \frac{1}{2}\frac{s_0}{1+s_0+(2\delta/\Gamma)^2}\end{aligned} \tag{2.25}$$

where Γ is the decay rate of the excited state. And

$$s_0 = \frac{2\Omega^2_{(Rabi)}}{\Gamma^2} \tag{2.26}$$

A moving ion experiences a Doppler shift thus δ will be rewritten as $\delta = \omega_L -$

$\omega_{eg} - \vec{k}_L \cdot \vec{v}$, where $\vec{v}$ is the velocity of the ion. The force exerted by the light due to the photon absorption and following spontaneous emission is [MvdS99]

$$F = -\hbar k_L^2 \frac{2s_0 \left(2\delta/\Gamma\right)}{\left(1 + \left(\frac{2\delta}{\Gamma}\right)^2\right)^2} \tag{2.27}$$

assuming $s_0 \ll 1$. The Doppler cooling limit is achieved when $\delta = -\frac{\Gamma}{2}$

$$k_B T_D = \frac{\hbar\Gamma}{2} \tag{2.28}$$

2.5.2 Resolved Sideband Cooling

In the interaction picture, the laser-atom interaction Hamiltonian is

$$H_I^{int} = \frac{\hbar\Omega_{(Rabi)}}{2} \left(|e\rangle\langle g| e^{-i(\delta t - \phi)} \exp\left(i\eta\hat{a}^\dagger e^{i\omega_\nu t} + i\eta\hat{a}e^{-i\omega_\nu t}\right) + H.c.\right) \tag{2.29}$$

where $\eta = k_L x_0$ is the Lamb-Dicke parameter. Thus the internal atomic states ($|g\rangle$ and $|e\rangle$) and the external motional states ($|m\rangle$ and $|n\rangle$) are coupled by the laser. Define $\Omega_{m,n}$ the effective Rabi frequency that corresponds to the transition from motional state $|m\rangle$ to $|n\rangle$

$$\Omega_{m,n} = \Omega_{(Rabi)} |\langle n| e^{i\eta\left(\hat{a} + \hat{a}^\dagger\right)} |m\rangle| \tag{2.30}$$

Equation 2.29 can be rewritten as

$$H_I^{int} = \frac{\hbar}{2} \sum_{m,n=0} \Omega_{m,n} e^{-i[(\delta - (n-m)\omega_\nu)t - \phi]} \sigma^+ |n\rangle\langle m| + H.c. \tag{2.31}$$

where $\sigma^+ = |e\rangle\langle g|$. The Rabi frequency scales like $\left(\eta\sqrt{n}\right)^{n-m}$. For $\eta \ll 1$, only $|n - m| = 1$ is considered. Make a Taylor expansion of $\Omega_{m,m\pm1}$ with η up to the

second order in η

$$n \rightarrow n \qquad \Omega_{n,n} = \Omega_{(Rabi)}\left(1 - \eta^2 n\right) \tag{2.32}$$

$$n \rightarrow n+1 \qquad \Omega_{n,n+1} = \Omega_{(Rabi)}\eta\sqrt{n+1} \tag{2.33}$$

$$n \rightarrow n-1 \qquad \Omega_{n,n-1} = \Omega_{(Rabi)}\eta\sqrt{n} \tag{2.34}$$

When the trapped ion is Doppler cooled to reach the Lamb-Dicke regime, the motional sidebands become resolvable [DBIW89]. In our experiment, the 674 nm laser is detuned on the red sideband to cause a coherent transition from $|5S_{1/2}\,(m = -1/2)\rangle|n\rangle$ to $|4D_{5/2}\,(m = -5/2)\rangle|n-1\rangle$, followed by an optical pumping from $|4D_{5/2}\,(m = -5/2)\rangle$ $|n-1\rangle$ to $|5P_{3/2}\,(m = -3/2)\rangle|n-1\rangle$. Then the ion preferentially decays from $|5P_{3/2}$ $(m = -3/2)\rangle|n-1\rangle$ to $|5S_{1/2}\,(m = -1/2)\rangle|n-1\rangle$ thus removing one phonon in the process.

Let us use Equation 2.31 to calculate the on resonance transition probability on the first blue sideband when $n - m = 1$ and $\delta = \omega_\nu$

$$P_{BSB} = \sum_0^\infty P(n)\,\frac{1}{2}\frac{\Omega_{(Rabi)}\eta^2\,(n+1)}{\Omega_{(Rabi)}\eta^2\,(n+1) + \Gamma^2/2} \tag{2.35}$$

where $P(n) = \frac{1}{1+\bar{n}}\left(\frac{\bar{n}}{1+\bar{n}}\right)^n$ is the thermal distribution of motional states and $\bar{n}$ is the expectation value of the motional quanta number n.

Similarly, let us calculate the on resonance transition probability on the first red sideband when $n - m = -1$ and $\delta = -\omega_\nu$

$$\begin{aligned} P_{RSB} &= \sum_1^\infty P(n)\,\frac{1}{2}\frac{\Omega_{(Rabi)}\eta^2\,(n)}{\Omega_{(Rabi)}\eta^2\,(n) + \Gamma^2/2} \\ &= \frac{\bar{n}}{1+\bar{n}} P_{BSB} \end{aligned} \tag{2.36}$$

Thus the expectation value of motional quanta number $\bar{n}$ is given by

$$\frac{P_{RSB}}{P_{BSB}} = \frac{\bar{n}}{\bar{n}+1} \tag{2.37}$$

In our experiment, P_{RSB} and P_{BSB} are the on resonance transition probabilities of $5S_{1/2}\,(m = -1/2) \rightarrow 4D_{5/2}\,(m = -5/2)$ on the first red and blue motional sideband.

2.6 Cryogenic Ion Trap Experiment Apparatus

The ion trap for ion heating tests in our experiment is a five wire surface electrode linear Paul trap. Traps are fabricated using microfabrication techniques and then mounted in a cermaic pin grid array (CPGA) carrier. The ion heating rate measurement is done in a liquid helium bath cryostat [Bak06]. Ion heating rates have been shown to be significantly reduced when ion trap electrodes are cooled to the cryogenic temperature [LGA+08]. The trapped ion is loaded by photoionization of neutral strontium atoms. A helical resonator is built to provide the potential confinement for the ion. Lasers are delivered by the optics system for ion cooling and ion manipulation, and outgoing signals are collected by PMT and CCD [LGA+08].

2.6.1 Surface Electrode Linear Paul Trap Design and Geometry

The trap for the ion heating measurement in our experiment is shown in Figure 2-5. The five electrodes DC, RF, GND, RF and DC all lay in the same $y = 0$ plane. The outer DC electrodes are segmented in the z direction for the axial ion confinement and better compensation.

Let us consider a rectangular electrode with opposite corners at positions $(x_1, 0, z_1)$ and $(x_2, 0, z_2)$, the shape function of this electrode geometry can be described by

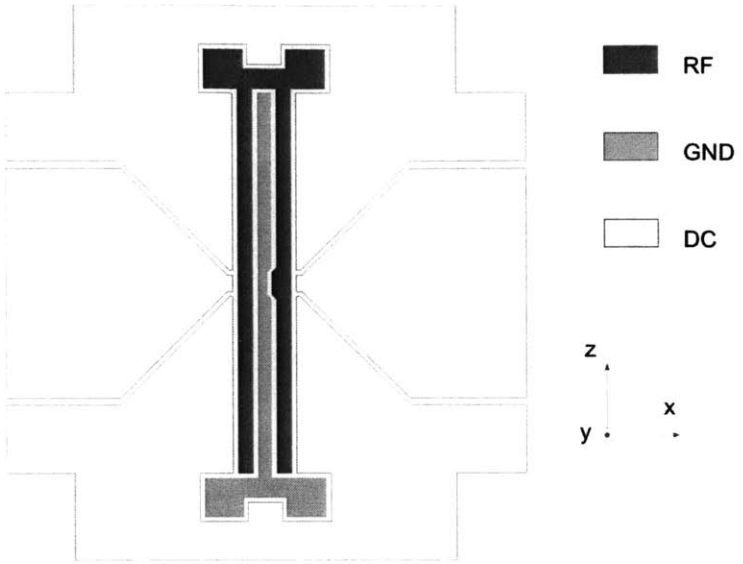

Figure 2-5: Schematic of a surface electrode linear Paul trap tested in our experiment. The five electrodes DC, RF, GND, RF and DC all lay in the same plane. The outer DC electrodes are segmented for axial ion confinement in z direction and for better compensation. The notch in the center ground electrode is designed to tilt the principle axes of the ion trap in $x-y$ plane to achieve laser cooling of the ion in y direction when the laser beam is parallel to the electrode surface.

[Hou08]

$$\begin{aligned}\phi(x,y,z) = \frac{1}{2\pi}\{&\arctan\left[\frac{(x_2-x)(z_2-z)}{y\sqrt{y^2+(x_2-x)^2+(z_2-z)^2}}\right]\\ &-\arctan\left[\frac{(x_1-x)(z_2-z)}{y\sqrt{y^2+(x_1-x)^2+(z_2-z)^2}}\right]\\ &-\arctan\left[\frac{(x_2-x)(z_1-z)}{y\sqrt{y^2+(x_2-x)^2+(z_1-z)^2}}\right]\\ &-\arctan\left[\frac{(x_1-x)(z_1-z)}{y\sqrt{y^2+(x_1-x)^2+(z_1-z)^2}}\right]\}\end{aligned} \tag{2.38}$$

To simplify the calculation, assume that the center GND and RF electrodes are infinite and there are no gaps between electrodes. In the space $y > 0$, the electric potential

can be described by

$$\phi(x,y) = \frac{1}{\pi}\left[\arctan\left(\frac{x_2 - x}{y}\right) - \arctan\left(\frac{x_1 - x}{y}\right)\right] \tag{2.39}$$

Apply the boundary condition

$$\phi(x,0,t) = \begin{cases} 0 & x < -c \\ V_{RF}\cos(\Omega t) & -c < x < 0 \\ 0 & 0 < x < a \\ V_{RF}\cos(\Omega t) & a < x < a+b \\ 0 & x > a+b \end{cases} \tag{2.40}$$

(where a,b and c are the widths of the center GND and two RF electrodes correspondingly) and get the electric potential

$$\begin{aligned} \phi(x,y) &= \frac{V_{RF}\cos(\Omega t)}{\pi}\{\arctan\left(\frac{a+b-x}{y}\right) - \arctan\left(\frac{a-x}{y}\right) - \arctan\left(\frac{x}{y}\right) \\ &\quad + \arctan\left(\frac{c+x}{y}\right)\} \end{aligned} \tag{2.41}$$

Taking derivative of Equation 2.41, the trapped ion position is given by

$$x_0 = \frac{ac}{b+c}, y_0 = \frac{\sqrt{abc(a+b+c)}}{b+c} \tag{2.42}$$

According to the outer DC control electrodes, as shown in Section 2.1.1, the presence of stray bias field will change the average ion position and induce the excess micromotion. Thus the outer DC electrodes not only confine the ion in z direction, but also push the ion toward the RF node to reduce micromotion.

The simplification is made by the assumption that there are no gaps. However, explicit calculations have shown that the gaps only have small effects on the overall potential field near the trap center.

In our experiment, as shown in Figure 2-5, there is a notch in the center electrode,

thus $a = 100$ µm, $b = 200$ µm and $c = 150$ µm, and the ion will be trapped at $x_0 = 42.8$ µm and $y_0 = 105.0$ µm. This notch is meant to tilt the principle axes of the ion trap in $x - y$ plane, thus the laser cooling beam that is parallel to the electrode surface can cool the ion in y direction.

According to the real trap geometry, CPO is used to calculate the shape functions $\phi_{RF}(x, y, z)$ and $\phi_{dc}(x, y, z)$ [CPO]. Then MATLAB is used to calculate the pseudo secular potential. Thus the secular frequencies, ion height and trap depth are all achieved. For a 150 µm trap, with $V_{RF} = 240$ V_{amp}, $V_1 = V_2 = 25$ V, $V_3 = -25$ V, $V_4 = -20$ V, the numerically calculated secular frequencies are 1 MHz along z direction and 2.5 MHz and 2.3 MHz in $x - z$ plane [Lab08].

2.6.2 Cryostat

A cryostat is an efficient means of reaching an ultra high vacuum using cryogenic temperatures. It usually takes four weeks for a room temperature trapping apparatus to achieve an ultra high vacuum (10^{-10} torr) including the pumping and baking time [LLC+09]. Outgassing also needs to be considered when choosing materials for the room temperature setup. However, the cryostat can easily achieve 10^{-10} torr within one day, which significantly reduces the testing time. In addition, outgassing is no longer a problem at a cryogenic temperature.

Our ion heating rate tests are carried out in a liquid helium bath cryostat [Bak06]. It mainly consists of a liquid helium tank surrounded by a metal 77 K nitrogen shield which is heat sunk to a liquid nitrogen tank. On the bottom of the helium tank there is a 4 K baseplate where the CPGA socket, electrical DC filters and a charcoal getter are mounted. The ion trap packaged in a CPGA carrier is directly mounted onto the socket. This testing space is surrounded by the metal 77 K nitrogen shield which can absorb the black body radiations and sink them to the liquid nitrogen tank. There are four openings on the shield. Three of them are used for optical access and the rest one is used for an electrical feedthrough. A RF helical resonator and a charcoal getter are also mounted on the shield. The cryostat has three side windows for delivering lasers and one bottom window for ion imaging [Lab08].

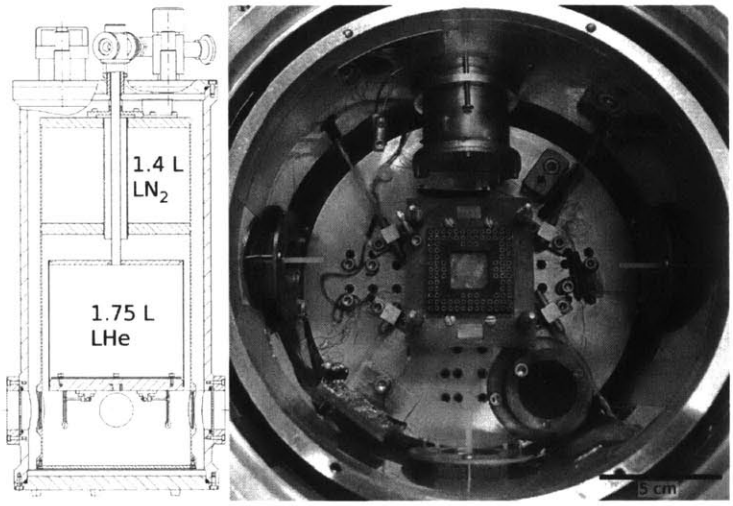

Figure 2-6: Left is the schematic of a liquid helium bath cryostat [Bak06, Lab08]. The liquid nitrogen tank and the 77 K nitrogen shield enclose the liquid helium tank. And on the bottom of the helium tank there is a 4 K base plate. Right is the picture of the 4 K base plate. On the 4 K base plate, the CPGA socket, DC filters and the getter are mounted. The RF helical resonator and another getter are mounted on the 77 K nitrogen shield.

2.6.3 Ion Source

In our experiment, the trapped ion is loaded by photoionization of neutral strontium atoms. Strontium vapor atoms are produced by applying a high current 5 A to the resistive oven where the strontium metal is wrapped. The resistive oven shielded by a copper box is mounted on the front of the RF helical resonator and is also heat sunk to the 77 K shield. The neutral strontium atoms are photoionized in a two stage process by 405 nm and 460 nm lasers [Lab08]. This photoionization method has advantages over other loading methods in less metal deposition onto electrodes and small stray electric fields.

2.6.4 RF

The confinement of an ion in a linear Paul trap requires a stable and high voltage radio frequency potential. A helical resonator with the desired frequency and a maximal quality factor is built to match the impedance between the RF source and the ion trap

and to filter out non-resonant components. In our experiments, the helical resonator is mounted on the 77 K Nitrogen shield in vacuum. The input RF source is 10 V_{amp} and the output potential to the RF electrode is approximately 200 V, thus the gain is around 20 [Bak06].

2.6.5 Laser and Optics

As described in Section 2.6.2, the cryostat has three side windows for delivering lasers and one bottom window for ion imaging. The doppler cooling 422 nm laser is split into two orthogonal ones to enable cooling in three dimensions. 1033 nm and 1093 nm IR lasers are coupled to one of them. The 674 nm laser for resolved sideband cooling and ion manipulation is applied along x direction. And the outgoing scattered signals are split by beam splitter so that 70% of the light goes to PMT and the rest 30% goes to CCD [Lab08].

Chapter 3

Microfabrication of Surface Electrode Ion Traps

The geometry of surface electrode ion trap not only makes it possible for ion traps to scale up to ion trap arrays but also enables the capability of building ion traps with microfabrication techniques. According to the schemes proposed for a large scale quantum computer, one challenge is to reduce the ion trap size. In this chapter, we present the microfabrication techniques we have used to miniaturize ion traps. We start with the facilities used for the fabrication of surface electrode ion traps in Section 3.2. We describe the ion trap substrate preparation in Section 3.2. We then detail the process of fabricating a planar ion trap in Section 3.3. In this section, techniques including lithography, etching, lift-off, electroplating and annealing are presented along with their advantages and disadvantages. This chapter closes with the trap dicing and packaging in Section 3.4.

3.1 Facilities Used for the Fabrication of Surface Electrode Ion Traps

The fabrication of surface electrode ion traps is conducted in the Nanostructures Laboratory (NSL) and Exploratory Materials Laboratory (EML) at MIT. The facilities

include optical lithography (spinner, Tamarack, the Karl Suss aligner MA-4, Heidelberg μ101), thin film deposition (Ebeam evaporator, AJA sputtering system, plasma enhanced chemical vapor deposition), dry etching (Technics Planar Etch II plasma asher, Plasma Therm RIE), wet etching (RCA cleaning station, chemical bench), thermal processing (annealing), microscopy and imaging (optical, scanning electron microscope, atomic force microscope), materials characterization (X-ray photoelectron spectroscopy), packaging (die-saw, wire bonder), and electroplating.

3.2 Surface Electrode Ion Trap Substrate Preparation

The fabrication process starts with the substrate cleaning. Substrate cleaning is one of the most important steps in the fabrication process of surface electrode ion traps, since the substrate surface chemistry and morphology can influence the adhesion, film formation process and resulting film properties. Cleaning is the removal of surface contaminants. There are several types of contaminants such as particles, fingerprints, chemical residues, water stains, adsorbed water vapor and adsorbed hydrocarbons.

The standard cleaning process for UHV components starts with a degreasing step in the ultrasonic bath using DI water with 10% detergent for 15 minutes. It is followed by a DI water spray rinse. After that, the substrate is transferred to a DI water ultrasonic bath for 15 minutes, which is followed by an acetone spray rinse. Then the substrate is transferred to an acetone ultrasonic bath for another 15 minutes. Spray rinse the substrate with Isopropanol and transfer it to an Isopropanol ultrasonic bath for 15 minutes. Substrates are blown dry with compressed nitrogen.

However, this standard cleaning process has its limitations. The detergent aims to loose the contaminants from the surface and take them into suspension by reducing the interfacial energy between particles and the substrate. Unfortunately, the detergent cannot completely remove the hydrocarbons that are strongly adsorbed to the oxide surfaces. With the presence of the adsorbed hydrocarbons, particles are easily stuck

in the hydrocarbon contaminations due to surface tension forces. As shown in Figure 3-1, assume that R is the radius of the particle and θ is the contact angle of the hydrocarbon contamination between the substrate surface and the particle. A is the contact area between the particle and the contamination and γ is the surface tension. Thus the surface tension force can be written as

$$F_s = \frac{2\gamma A}{r} \tag{3.1}$$

where r is the fluid surface radius and can be derived from the contact angle. Assume $\theta = 30°$, $r = \frac{2-\sqrt{3}}{2+\sqrt{3}}R$ and $A = \pi R^2\left(2-\sqrt{3}\right)$. For water, $\gamma = 0.072$ N/m, the surface tension force is $F_s \approx 1.69R$.

However, the force of drag experienced by a particle in free-flow fluid is

$$F_d = \frac{1}{2}\rho v^2 A C_d \tag{3.2}$$

where ρ is the density of the fluid. v is the speed of the particle relative to the fluid flow. C_d is the drag coefficient. A is the contact area [Bat67]. In our cleaning process, assume $C_d = 0.2$ and $v = 0.1$ m/s. The total force of drag can be described as $F_d \approx 1.6 \times 10^8 R^4$. Thus the surface tension is much bigger than the hydrodynamic force, and only large particles ($R > 2$ mm) can be removed by the drag force of fluid.

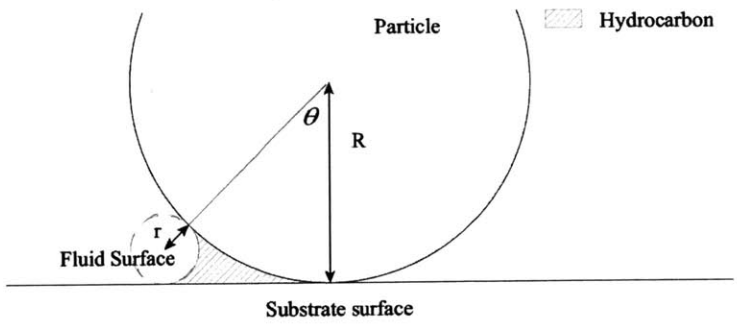

Figure 3-1: Schematic of a contaminant particle sticking to the substrate surface with the presence of the adsorbed hydrocarbons. Assume the contaminant particle has a radius R and the fluid surface has a radius r. The contact angle of the hydrocarbon contamination between the substrate surface and the particle is θ.

As for the ultrasonic bath, it involves growing and collapsing of cavitation bubbles [RK10]. When the cavitation bubbles collapse on the substrate surface, they provide a high pressure jet of fluid against the surface, which can remove loosely adsorbed particles. The ultrasonic bath we are using ($\sim$ 40 KHz) is good at removing large particles; however, it is less efficient when the particle size decreases to microns. In order to remove smaller particles, MHz frequency is required. Thus the previous cleaning process cannot work efficiently. Oxidative cleaners must be used to remove the remaining hydrocarbons, reducing the adhesion of particles.

In our cleaning process, we use Piranha solution as the oxidative cleaner which can clean organic residues off substrates. Piranha solution is a mixture of concentrated sulfuric acid (H_2SO_4) and 30% hydrogen peroxide (H_2O_2) solution in a 3 : 1 volumetric ratio. There is no need to heat the solution since mixing the solution is exothermic and resultant temperature goes up to 80 °C from room temperature. The hydrogen peroxide boosted by sulfuric acid provides free atomic oxygen for cleaning. The oxidation process allows Piranha solution to dissolve carbon atoms. Piranha cleaning must be followed by a thorough DI rinsing.

An alternative way to do reactive cleaning is using reactive oxygen plasma to react with contaminations and form volatile species which leave the surface. Oxygen plasma is also efficient in removing hydrocarbons and adsorbed water.

A series of atomic force microscope (AFM) tests are conducted on fused silica substrates cleaned by different methods. As shown in Figure 3-2, fused silica substrate cleaned by Piranha achieves the lowest surface roughness.

Our standard cleaning process for the substrate preparation is:

1. Mount the substrate to a spinner and set the spinning speed to 500 rpm. Clean the substrate surface with a q-tip soaked with detergent. When the q-tip sweeps over the surface, the friction is proportional to the force that presses the q-tip to the surface. This friction plays an important role in particle removal. Rinse the substrate thoroughly with DI water to remove the residue detergent.

2. Soak in Piranha solution for 15 minutes to get ride of the hydrocarbon and other

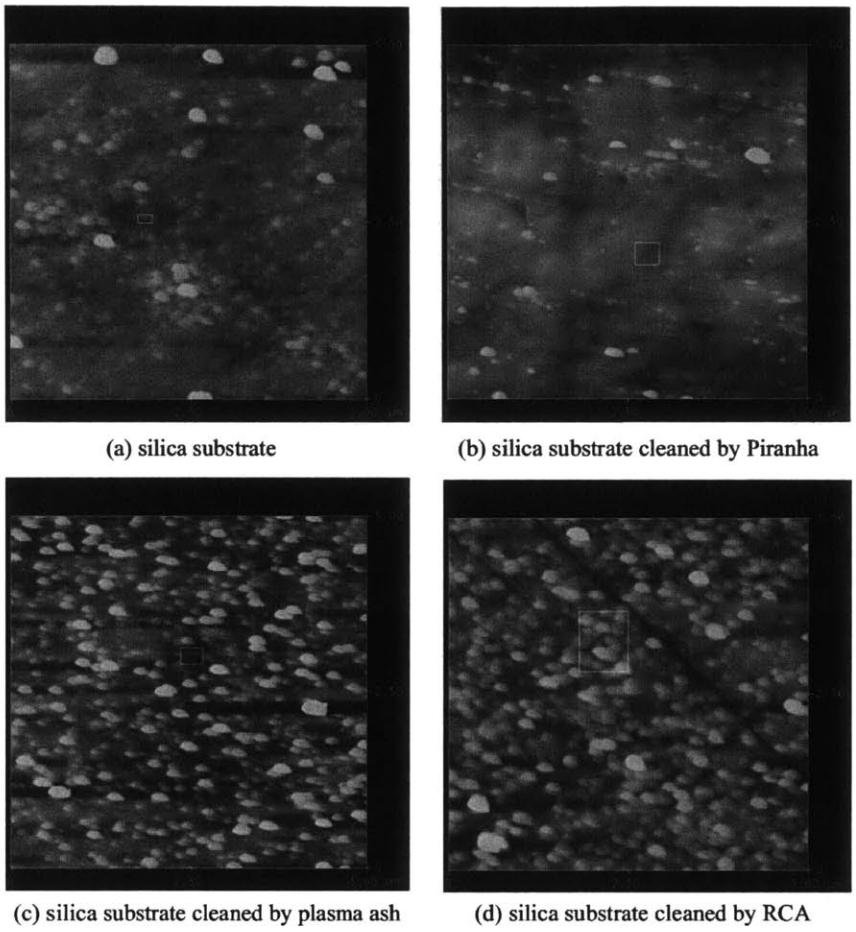

Figure 3-2: A comparison of AFM tests on fused silica substrates cleaned by different methods. (a) is the silica substrate without any cleaning process. (b) is the silica substrate cleaned by Piranha. (c) is the silica substrate cleaned by plasma asher. (d) is the silica substrate cleaned by RCA. Same AFM scanning parameters are used on four substrates.

organic contaminations. Substrates are then thoroughly rinsed in DI water for at least 3 minutes.

3. Drying. It is important to dry the substrate surface quickly in order to prevent the wafer surface from collecting particles. And those particles collected during drying will adhere tenaciously. That is also the reason why we need to keep the substrate surface wet during the cleaning process; normally, we use the solution in next step to displace the surface layer of residue in last step. Surfaces are

usually blown dry using a high velocity (10000 feet per min) dry nitrogen gas.

After the cleaning and drying process, we check the particle contamination on the substrate surface by observing scattered light, which is capable of detecting particles as small as 0.1μm.

3.3 Surface Electrode Ion Trap Fabrication

The substrate cleaning is followed by the electrode fabrication. Our surface-mounted electrode geometry is compatible with the planar fabrication process. The planar fabrication process usually consists of two steps: lithography and pattern transfer. Pattern transfer can be accomplished by either etching or lift-off. Ebeam evaporation and sputtering are usually used for thin film deposition. When dealing with a thick film deposition, electroplating is introduced. If wet etch is used for pattern transfer, annealing is conducted afterwards for better trap performance.

3.3.1 Lithography

Photoresists for optical lithography have micron-sized resolution and are commonly used at ultraviolet spectrum. All photoresists (PR) are polymeric, changing properties upon the exposure to the light. Optical photoresists have two tones: positive and negative. Once exposed to the light, positive photoresists become soluble in the developer, while negative photoresists become insoluble to the developer. After the development, the remaining photoresist resists etching, or metal deposition thus protecting the area underneath. Positive photoresists have the advantages of better resolution and better step coverage. Negative photoresists have the advantages of good adhesion to substrates and better wet chemical resistance [Mad02]. Thus photoresist can be appropriately selected according to the pattern transfer process.

The most commonly used positive tone photoresists in our fabrication are AZ4620 and S1813. Positive AZ4620 has unmatched capabilities in applications requiring thick PR layer($>$ 6 μm). It has good resolution and remains good adhesion in acidic

plating baths, which makes it an ideal electroplating mold. In contrast, S1813 is approximately 1 µm thick, perfect for contact pads lift-off. The most commonly used negative tone photoresists in our fabrication are NR9-3000PY and NR9-3000P. Both are from Futurrex [Fut]. After the development, NR9-3000PY exhibits a negative-sloping resist sidewall profile which can be controlled by the exposure energy, enabling a lift-off process. NR9-3000P shows good adhesion and chemical resistance, ideal for etching [Fut].

The standard optical lithography process involves photoresist application, soft baking, mask alignment, exposure, post exposure baking, development and hard baking. Before photoresist application, substrates are heated on a hotplate to dehydrate the surface and improve the adhesion. Due to the feature size of our surface electrode ion traps, micron sized defects are fatal. There are several factors affecting the PR coating process which might result in fatal defects. Air bubbles in photoresist, particles existing on substrate surface prior to application, too high spin acceleration and off center PR application will cause air bubbles, pinholes and streaks in the PR layer which should be carefully avoided. The spin speed and the spin time will determine the final PR layer thickness. Coated wafers are soft baked on a hotplate or in an oven to eliminate the solvent inside the photoresist.

There are two ways to do the exposure: a parallel lithography using a mask and a serial lithography written directly by a focused laser beam. The parallel lithography using a mask is more efficient for pattern replication and is widely used in our ion trap fabrication. Mask is a soda-lime glass plate with chrome metal layer on one side, which will be in contact with PR layer in the contact exposure mode. According to the tone of photoresist, dark field or clear field mask is selected. Ion trap design patterns are generated by Autocad and saved in dxf format. The designing rule for drawing masks using Autocad is that all features should be composed of closed polylines with zero linewidth. Patterns are directly written to a commercial chrome plate coated by AZ1518, using Heidelberg μ101 which is capable of exposing high resolution design with minimum feature of 1 µm. The common exposure time for a 4" $\times$ 4" mask is 16 hours with unidirectional writing mode. After the exposure, the chrome plate is

developed and chrome etched. The final pattern on the mask is 1 : 1 image of the real pattern.

Substrates coated with PR are then exposed in hard contact mode by Karl Suss aligner MA-4. The direct contact between the photoresist and the mask enables a high resolution. The wafer held on a vacuum chuck is brought into contact with the mask for exposure and lowered to the separation level for alignment. (In separation mode, the spacing between the mask and the photoresist is around 100 μm.) The Karl Suss aligner MA-4 uses a 350 W high pressure mercury lamp and has a calibrated exposure intensity of 9.3 mW/cm^2. The alignment system consists of an IR light and a microscope. The exposure time is set according to the exposure dose needed. In case no alignment is needed, Tamarack is an alternative exposure tool with a calibrated exposure intensity in a range of 0.9 mW/cm^2 to 3.4 mW/cm^2.

As for the serial lithography, pattern is directly written by Heidelberg μ101 onto the PR coated wafer after soft bake.

After the exposure, post exposure bake the sample if necessary. The last step in optical lithography process is development. Development time is also critical in achieving desired side wall profile.

3.3.2 Etching

After the lithography is done, etching can be used to remove metal from areas unprotected by photoresist, forming gaps between electrodes. Either wet chemical etching or reactive ion etching (RIE) can be used in the patterned etching of metal films.

Wet chemical etching is conducted in a chemical bath. In most cases, the etching rate is the same in all directions. The lateral etch ratio $R_L = \frac{\text{Horizontal etch rate}}{\text{Vertical etch rate}} = 1$, which results in a large undercut when etching a thick film. In addition, etchant needs to be properly chosen for a good selectivity - high ratio of etch rate of the target material to etch rate of other materials.

As mentioned in Section 3.3.1, NR9-3000P is a good masking material with excellent resistance to most metal etchants, for example, gold etchant, aluminum etchant, chrome etchant, silver etchant and copper etchant. For an ion trap purpose, electrodes

must have good edge quality thus can carry a high breakdown voltage. However, due to the isotropic property of wet etching, the undercut can not be precisely controlled and the edge quality is not guaranteed. We have done several wet etching tests on the edge qualities of different electrode materials. When etching polycrystalline metal layer, the etch rate is different for different crystal planes, thus the edge is zigzag. As shown in Fig.3-3, the test results indicate that faster etching rate produces better edge quality. Among all the tested electrode materials, silver has the largest etch rate. However, silver ion traps made by wet chemical etch still have glow points when a high RF voltage ($\sim 200\ V_{amp}$) is applied. To get ride of the sharp edge points resulting from wet chemical etching process, an annealing process is performed afterwards which is discussed in section 3.3.5.

Evaporated aluminum is etched by a phosphoric acid-based etchant, which is a mixture solution of 85% phosphoric acid(H_3PO_4), 70% nitric acid (HNO_3), 99% acetic acid (CH_3COOH) and H_2O in a $16:1:1:2$ volumetric ratio [Tra].

Evaporated gold is etched by AU-5. Gold etchant AU-5 from Cyantek is a mixture of $5\%I_2 + 10\%KI + 85\%H_2O$ [Cya].

Evaporated copper is etched by a solution of Aqua Regia, which is a mixture of 70% hydrogen chloride (HCl), 70% nitric acid (HNO_3) and DI water (H_2O) in a $3:1:2$ volumetric ratio.

Evaporated silver is etched by a mixture solution of 29% ammonium hydroxide (NH_4OH), 30% hydrogen peroxide (H_2O_2) and DI water (H_2O) in a $1:1:4$ volumetric ratio.

The dry etching method is fundamentally different. Dry etching is conducted in a vacuum chamber ($10 \sim 100$ mtorr) and the metal in unprotected areas is removed by ion bombardment and chemical reaction. During RIE, a plasma is ignited by applying a RF oscillating electromagnetic field. Reactive species including ions and radicals are generated in the plasma. The reactive species arrive at the metal surface due to the voltage difference and react with the metal. The reaction products are volatile and desorbed from the surface. Etching gas is selected so that it can react with the metal to be etched and the reaction product is volatile. Due to the vertical delivery

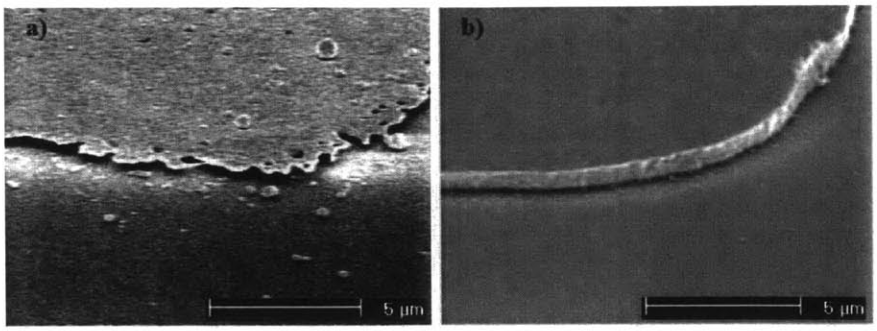

Figure 3-3: A comparison of SEM tests on the edge qualities of different electrode materials patterned by wet etch. (a) is the edge of gold electrode wet etched by AU-5. (b) is the edge of silver electrode wet etched by a mixture solution of ammonium hydroxide, hydrogen peroxide and DI water. Silver etchant has faster etching rate resulting in better edge quality. However, defect points can still be observed at the edge of silver electrode which will glow when a high RF voltage is applied.

of the reaction species, reactive ion etching can provide an anisotropic etch profile comparing to an isotropic wet etch. Reactive ion etching is automatically stopped when the underneath substrate is reached. The selectivity of dry etch is not so good that photoresist can be etched in the same RIE process. We ensure that the initial Photoresist layer is thick enough to survive the entire RIE process [Mad02].

Aluminum, niobium and niobium nitride ion traps have been successfully fabricated using RIE. Aluminum layer can either be evaporated by Ebeam evaporator or sputtered using AJA sputter onto a clean quartz substrate before lithography. Then the patterned aluminum layer is reactive ion etched, using the recipe $BCl_3 = 5$ sccm, $Cl_2 = 5$ sccm, Ar = 3 sccm, chamber pressure $p = 5$ mtorr, RF power $P = 50$ W. The etch rate of aluminum is 8.3 Å/second.

Niobium or niobium nitride layer is sputtered onto a clean sapphire substrate before lithography. The patterned niobium or niobium nitride layer is reactive ion etched, using the recipe $CF_4 = 15$ sccm, $O_2 = 1$ sccm, chamber pressure $p = 10$ mtorr, RF power $P = 150$ W. The etch rate of niobium is 6 nm/min.

After the dry etching process, a thorough rinse in DI water is necessary followed by stripping of photoresist with acetone and isopropanol.

3.3.3 Lift-off

Lift-off process is an alternative way to pattern metals that are difficult to etch. The lift-off process involves patterning substrate surface with photoresist, followed by metal layer deposition and immersion in solvent to remove photoresist together with metal film regions on top of it. Thus only films that are deposited directly on the substrate are left. Compared to the etch process, the lift-off process has excellent precision and there is no observed sharp edge point as long as the resist has a negative sidewall.

The negative-sloping resist sidewall profile that NR9-3000PY has facilitates a simple resist lift-off process. The negative sidewall angle can be precisely controlled by the exposure dose [Fut]. The successful lift-off process also requires a metal deposition with poor step coverage. In Ebeam evaporation, materials evaporate in a high vacuum chamber in which vapor particles reach the substrate almost at the same angle resulting in a poor step coverage. However, in sputtering, energetic atoms arrive at the substrate at random angles, thus sidewalls of photoresist will be covered and "ears" are formed. Those ears will remain connected to the electrodes after the lift-off process and affect ion trap performance. In the last immersion step, solvent penetrates the metal film and dissolves the photoresist underneath. The film quality can affect the lift-off speed.

Breakdown voltage is a very important factor to be considered in the ion trap fabrication. Usually, a breakdown voltage of around 200 V is observed in a silver ion trap fabricated by the lift-off process. Contrary to the point glow due to the sharp edge point resulting from wet chemical etch, uniform glows along electrode edges are observed when a voltage higher than the breakdown voltage is applied as shown in Figure 3-4(a). SEM results show that those uniform glows at low breakdown voltage are correlated to the isolated nano-sized "bubbles" in the proximity of electrodes. Those bubbles shown in Figure 3-4(b) are due to using an overhang structure in conjunction with the normal incidence evaporation of metal. As shown in Figure 3-5, there is a gap between the electrode edge and the photoresist sidewall, called vale

of death [Mat98]. Bubbles existing in this gap probably result from the shadow of imperfectly collimated metal source against the resist edge. In addition, the presence of the gap allows the energetic atoms on the substrate surface to diffuse or enables the deposition of metal atoms that are reflected off other surfaces in the chamber and approach the surface at other than normal incidence.

This bubble issue is especially severe when depositing noble metals. Noble metal exhibits a low adhesion energy to the oxide surface. Thus adatom-adatom interactions are stronger than those of adatom-oxide surface, leading to the formation of isolated adatom islands [Cam97]. As the deposition goes on, the isolated islands grow and coalescence into continuous film. The metal deposition in vale of death is so small that only isolated islands are formed. In our experiments, isolated islands are observed in gold and silver evaporation, however, not in aluminum and copper deposition.

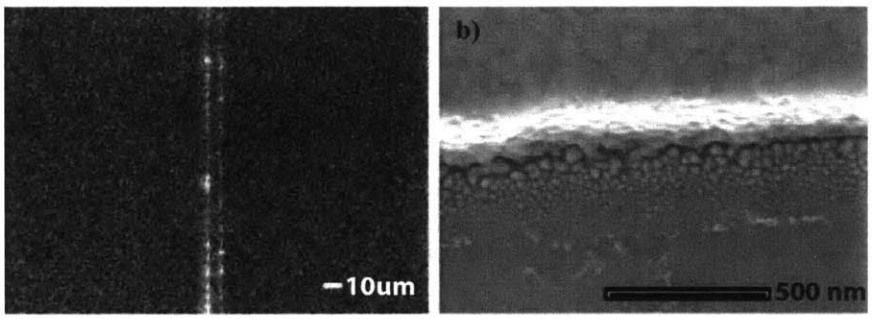

Figure 3-4: (a) is an optical picture of electrode edges with uniform glows when 100 V is applied. At some places, glows are brighter than elsewhere. Those bright glows are due to the sharp edge points of the electrode. (b) is the SEM image of the nano-sized "bubble" zone. The bubble zone is 200 nm wide, adjacent to the electrode edge. The nano-sized "bubbles" are correlated to the uniform glows in (a). Electrode edges with bubble zones have low breakdown voltage.

The glow observed along the electrode edge is a form of surface flashover, which occurs over the surface of dielectric materials between two adjacent electrodes. The surface flashover usually starts from the electron emission from the interface where the dielectric material, conducting electrode and vacuum are in close proximity [MDH11]. In our noble metal electrode case, electron emission from the electrode edge will strike the oxide surface in the proximity, resulting in charging of those isolated metal islands.

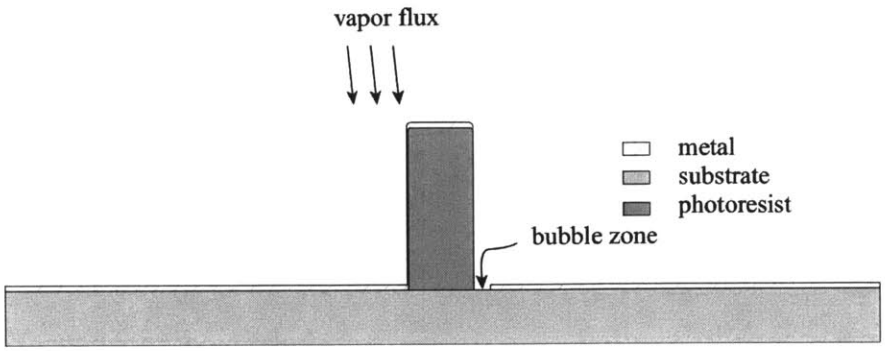

Figure 3-5: Schematic of shadow effect. The bubble zone is due to the shadowing of the deposition flux by the photoresist. In Ebeam evaporation, vapor particles reach the substrate almost at the same angle.

Charging keeps building up without an efficient way to dissipate since islands are isolated. However, the RF voltage is oscillating and when the RF potential changes it polarity, there will be a large voltage difference between the RF electrode and the isolated island. There is a distance dependence of the breakdown voltage with $V_b \propto d^{0.5}$ [Mil93]. The distance between the electrode edge and the isolated island d is on the order of hundreds of nanometers, thus the breakdown voltage V_b has been significantly lowered.

The solution to this problem is to use a photoresist with vertical sidewall. S1813 can provide vertical sidewall; however, it is too thin for a thick electrode lift-off. We stick with NR9-3000PY and find that a re-entrant sidewall can be achieved with properly controlled exposure intensity and time. A series of tests are done on the combination of exposure intensity and time. The breakdown voltage really relies on the shape of the photoresist sidewall. Figure 3-6 shows the ideal sidewall profile. This is achieved using 7 minutes exposure at 850 $\mu W/cm^2$. Development time (22 seconds) must be carefully controlled and over development will ruin this profile resulting in low breakdown voltage. This process is not repeatable. The working parameter window is really small.

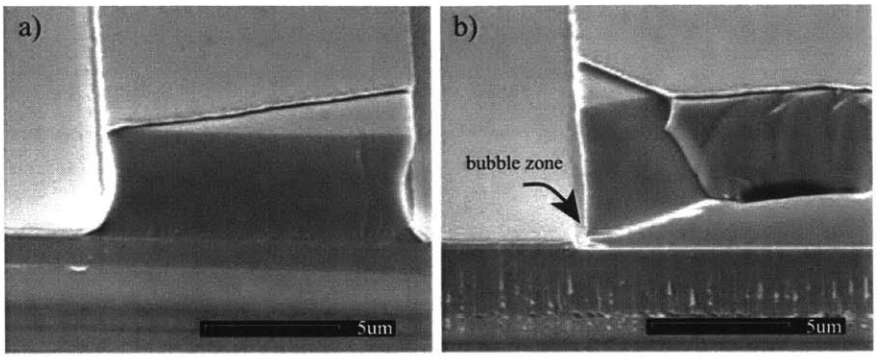

Figure 3-6: SEM images of NR9-3000PY used for lift-off. (a)NR9-3000PY exhibits a reentrant sidewall profile. After lift-off, ion trap has a high breakdown voltage. (b)NR9-3000PY exhibits a negative-sloping sidewall profile. Bubble zone is observed due to the shadow effect, resulting in low breakdown voltage.

3.3.4 Electroplating

The pattern transfer methods discussed in Section 3.3.2 and Section 3.3.3 involve a physical vapor deposition (evaporation or sputtering). However, due to stress accumulation, a thickness of more than 2 μm can hardly be achieved using these processes. For thicker film deposition, electroplating is used.

In the electroplating setup, anodes and cathodes are immersed in an electroplating bath which contains a reducible form of ion of the desired metal. They are both connected to an external direct current supply. The anode is connected to the positive terminal of supply, while the cathode is connected to the negative terminal. The metal ions are reduced at the cathode and deposited at the cathode surface.

In our experiment, gold electroplating solution Transene TSG-250 containing a sulfite-based electrolyte $[Au(SO_3)_2]^{3-}$ is used to plate soft gold, and it does not attack the photoresist mold. Figure 3-7 shows the electroplating setup. Platinized titanium mesh is used as the anode. The reaction at the anode is the oxidation of water.

$$2H_2O \rightleftharpoons 4H^+ + O_2 + 4e \tag{3.3}$$

The concentration of Au^+ will decrease with time. In real electroplating process, the situation is more complicated. Ions will align in solution near the electrode surface

to screen the applied potential forming an electrical double layer, called Helmholtz double layer [Per04]. It is followed by a diffusion layer. In sulfite-based electrolyte, Au^+ and ligand $[(SO_3)^{2-}]$ form an Au(I) complex by $Au^+ + 2SO_3^{2-} \rightarrow [Au(SO_3)_2]^{3-}$. At the cathode, this complex must diffuse through the double layer to reach at the cathode surface. The presence of the ligand slows the diffusion of gold ion in both layers. In the Helmholtz layer, the Au(I) complex will be derived of the ligand, and the resulting gold ion is reduced and adsorbed at the cathode surface. The heating and agitation will help improving the complex diffusion rate. pH control is used to control the complex formation. Thus temperature, heating and pH need to be carefully controlled. In our gold electroplating, electroplating bath is heated on a hotplate to 130 F. We use magnetic stirrer for agitation and the stirring speed is set to 400 rpm. pH is inspected between 6.0 and 7.0 by a pH indicator. If the plating starts before the plating bath achieves uniformity by agitation, there will be weird strip patterns observed on the surface of the plated gold layer. In addition, the substrate is wetted by water before immersion in plating bath to get rid of the bubbles which will result in defects in the following plating process.

For electrolytic plating, all features need to be electrically connected. In our experiment, a titanium/silver layer is Ebeam-evaporated on a clean single crystal quartz substrate. Then the sample is patterned using 6 µm thick AZ4620 positive photoresist. In principle, copper and gold could also be chosen as the seed layer. However, we found, in our electroplating setup, the plating bath will react with copper and become contaminated without applying any potential. The contaminated plating bath is green due to the existence of copper ions. In principle, gold ion is easier to reduce than a copper ion and will plate out first due to the lower electromotive potential. However, in our plating bath, the formation of the Au(I) complex will result in a shift of the reduction potential, which enables both ions to deposit. Later, those copper ions will be reduced together with gold ions on the cathode surface resulting in a black surface. Gold seed layer is abandoned since the electroplated gold layer will also be attacked in the wet chemical etch of gold seed layer. The titanium/silver seed layer with the PR mold on top is working as the cathode.

The thickness of electroplated gold on the substrate is determined by the electroplating current density and the plating duration time. A constant current is provided by a DC supply with an intensity of 1.0 mA/cm^2 (calculated by $\frac{\text{current}}{\text{electroplated area}}$). The deposited gold layer is polycrystalline with grain features as shown in Figure 3-8(a). The grain size is controllable, and it decreases with increasing electroplating current density. The effect of the grain size of electroplated gold film on ion heating is discussed in Section 5.2.

After the electroplating, photoresist AZ4620 is removed by acetone, followed by a rinse in isopropanol and a compressed nitrogen blow. In the last step, silver seed layer which is used to electrically connect all features is removed by wet chemical etch. The silver etchant $NH_4OH : H_2O_2 : H_2O = 1 : 1 : 4$ will selectively etch silver away without attacking electroplated gold layer on top. The sample is dipped in a diluted HF ($HF : H_2O = 1 : 4$) to remove titanium adhesion layer, and then is rinsed thoroughly in DI water for at least 3 minutes to completely remove chemical residues.

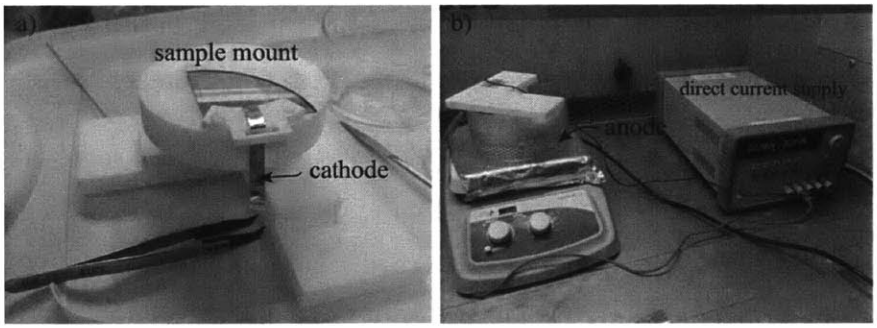

Figure 3-7: (a) A titanium/silver seed layer on quartz substrate patterned by AZ4620 is mounted as the cathode. The sample mount is made of Teflon. Sample is connected to the direct current supply through a copper tape. (b) The plating bath is kept in the beaker and heated on the hotplate to 130 F. Platinized titanium mesh, used as the anode, is immersed in the plating bath, surrounding the cathode.

3.3.5 Annealing

As mentioned in Section 3.3.2, there will be sharp edge points on the electrode resulting from wet chemical etching process, and an annealing process is performed

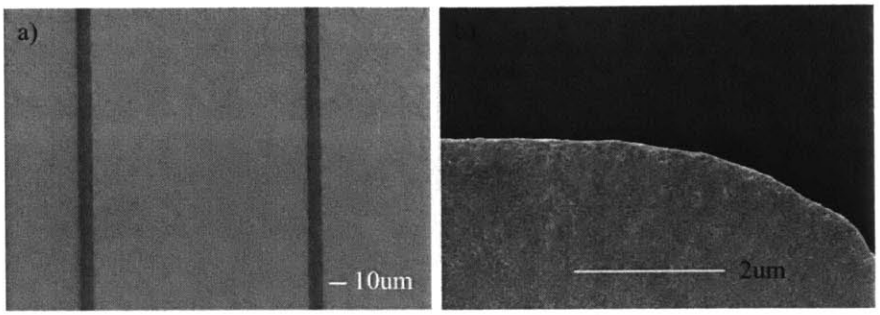

Figure 3-8: (a) Optical microscope image of an electroplated gold electrode. Grain features can easily be observed. (b) SEM image of an electroplated gold electrode. There is no sharp edge point even at the corner of the electrode.

afterwards. Annealing is done by substantially heating the sample for a duration of time and allowing it to cool. To avoid the oxidation of metal surface due to the high temperature of annealing, annealing is carried out in a small vacuum chamber. As shown in Figure 3-9, a copper oven is built with 60 turns of tungsten wire as the heating element. A thermocouple is attached to the oven to monitor the annealing temperature. With 300 W dissipated in the 6.2 ohm tungsten wire, the oven can be heated to a temperature higher than 650 °C. It takes one hour for the annealing setup to achieve the desired temperature and then the trap is annealed at that desired temperature for another hour. Once the annealing process has been successfully completed, the sample is left in oven to cool to room temperature before it is taken out of the vacuum chamber. The cooling process usually takes one hour.

When metal is heated, atoms begin to migrate and rearrange themselves to reduce the surface and grain boundary free energies. A groove will form on the surface at the intersection of boundary and surface. In addition, when silver is heated in vacuum at high temperature, the evaporation of silver atoms without condensation in vacuum will deepen the boundary groove. As the grain growth occurs, the groove moves forward with the grain boundary. the grain boundaries are delineated by grooves formed at the intersection of the boundary and the surface.

If the annealing temperature goes up further and reaches a particular temperature for recrystallization, new stain free grains start to grow, with each grain representing

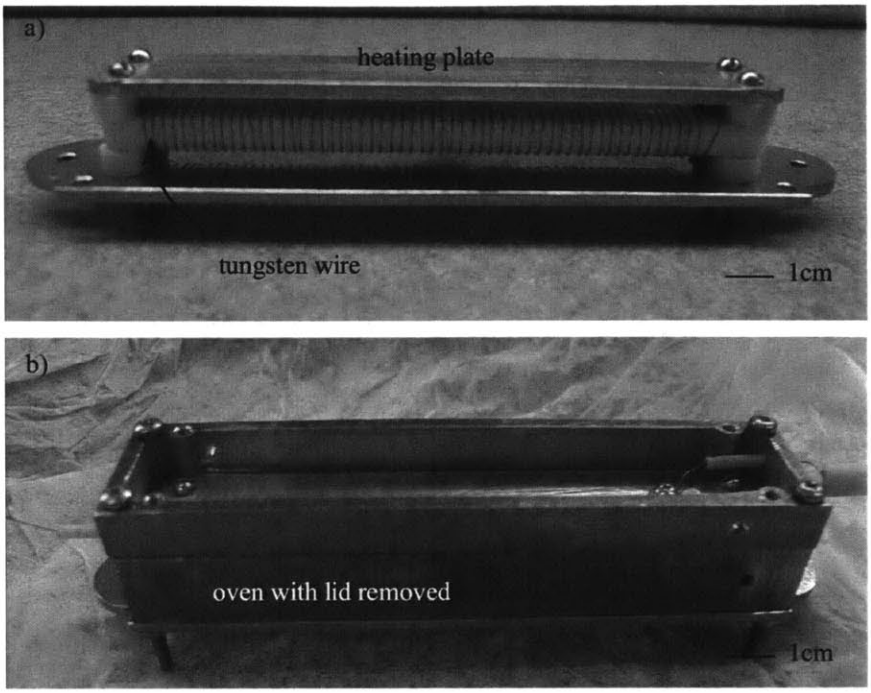

Figure 3-9: (a)Heating plate of the annealing oven with tungsten wire underneath. Samples are put on the heating plate for annealing. (b) Annealing oven with lid removed. The annealing oven will be kept in a vacuum chamber. Samples can be heated up to 800 °C in the oven.

a single crystal. The recrystallization temperature is usually between $\frac{1}{3}$ to $\frac{1}{2}$ of the melting point which is 1235 K for silver.

Different annealing temperatures result in different stages of recrystallization, thus different surface topographies. As shown in Figure 3-10, evaporated silver films annealed at 720 °C and 760 °C have different morphologies, thus having different gloss appearances. The surface condition can influence the spectacular reflection. A 650 nm laser hits the silver surface at 90 degree and the reflection power is measured [Lab08]. For evaporated silver surface, approximately 90% of light is reflected, making them appear shiny. For 720 °C annealed silver surface, approximately 75% of light is reflected, however, for the 760 °C annealed silver surface, only 5% of light is reflected, since the rough surface causes the light to scatter at different angles, making them appear dull. The visible light has a wavelength range of 400 to 700 nm, thus surface

roughness in micrometer range will influence the specular reflection.

For normal incidence, the path difference between rays reflected from the top and bottom of the surface bumps is $2h$, where h is the characteristic roughness height. For 650 nm laser, when the phase difference $\frac{4\pi h}{\lambda}$ is close to π, these two rays will cancel each other, resulting in very low intensity of specular reflection. For the 760°C annealed silver, the characteristic roughness height is around 80 nm.

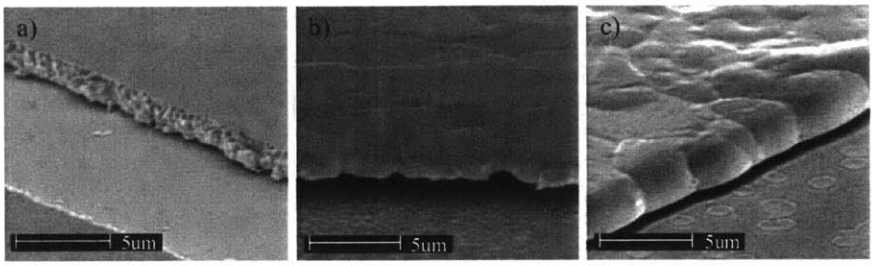

Figure 3-10: SEM images of the silver trap before annealing and after annealing. (a) Silver trap after wet etch without annealing. (b) Silver trap after annealing at 720 °C for 1 hour. (c) Silver trap after annealing at 760 °C for 1 hour.

The influence of silver annealing process on the ion heating rate is discussed in Section 5.4.

3.4 Trap Dicing and Packaging

The fabrication process closes with trap dicing and packaging. Most of our ion traps have a dimension of 1 cm × 1 cm. Wafers are diced into individual chips using the diesaw either before or after fabrication. Before cutting, wafers are coated with photoresist NR9-3000P and baked on a hotplate at 100 °C for 5 min to cure. This photoresist layer protects the sample surface from contamination. The coated wafer mounted on a 265 µm thick tape is held to the diesaw chuck by vacuum. Glass mode is selected and a black blade for glass is mounted. The die streets are approximately 200 µm wide. One die consists of 3 cuts, and each cut deepens 0.5 mm into the thick quartz substrate. After dicing, tape is removed by the exposure to UV light. Before removing the protective photoresist layer with acetone, diesaw cut pieces are held

under a running DI water for 3 minutes to avoid the diesaw dust sticking to the trap surface. In the case of cutting small pieces, such as an ion trap array mounted in an optical cavity which has a dimension of 18 mm $\times$ 3 mm, wafer coated with photoresist is first glued to a clean 4 inch silicon wafer with the same photoresist. The stack structure is then mounted on the tape. The presence of the silicon wafer is for better adhesion of small pieces, since diesawing is a violent operation and the small pieces will be washed away if directly mounted on tape.

The diced ion traps are cleaned with acetone and isopropanol. Spare ion traps are coated with photoresist NR9-3000P and baked. Coated ion traps are then kept in a clean container for storage.

The final ion trap is mounted as shown in Figure 3-11 in a ceramic pin grid array (CPGA) carrier (Global Chip Materials IPKX0F1-8180AB) with a copper or niobium spacer underneath using Torr Seal (Varian Torr Seal Vacuum Equipment High Vacuum Epoxy, Good to 1×10^{-9} torr) for cryogenic test and using epoxy EPO-TEK 353ND for room temperature test. Both epoxies can be cured at 75 °C for 40 min. For the surface temperature measurement, heating resistors and RuO_2 temperature sensors are mounted to the ion trap surface using solder paste (Indium 5.8LS pb-Free Solder Paste). Solder paste is applied to the ion trap surface using bonding wires under wire bonder microscope. Solder paste melts and bonds at 240 °C. 1 nF capacitor is glued to the CPGA ceramic with one end connecting to the outer gold plated CPGA ground ring and the other end connecting to ion trap DC electrode to reduce RF pickup and filter noise.

All the electrical connections are made by wire bonding. Two types of wire bonders have been used, one is West Bond Model 7476D using aluminum wedge wire bonding, and the other is West Bond 454647E using gold ball bonding. The gold ball bonding has a non-directional property and the tip is smaller, thus it is easier to use for small feature wire bonding. However, the gold ball bonding has adhesion problem on several pads, such as aluminum, copper, silicon and niobium. Thus gold contact pads are necessary in these cases. Aluminum wedge bonding applies an ultrasonic energy to the wire for a specific duration when the wire is held down to the pad by

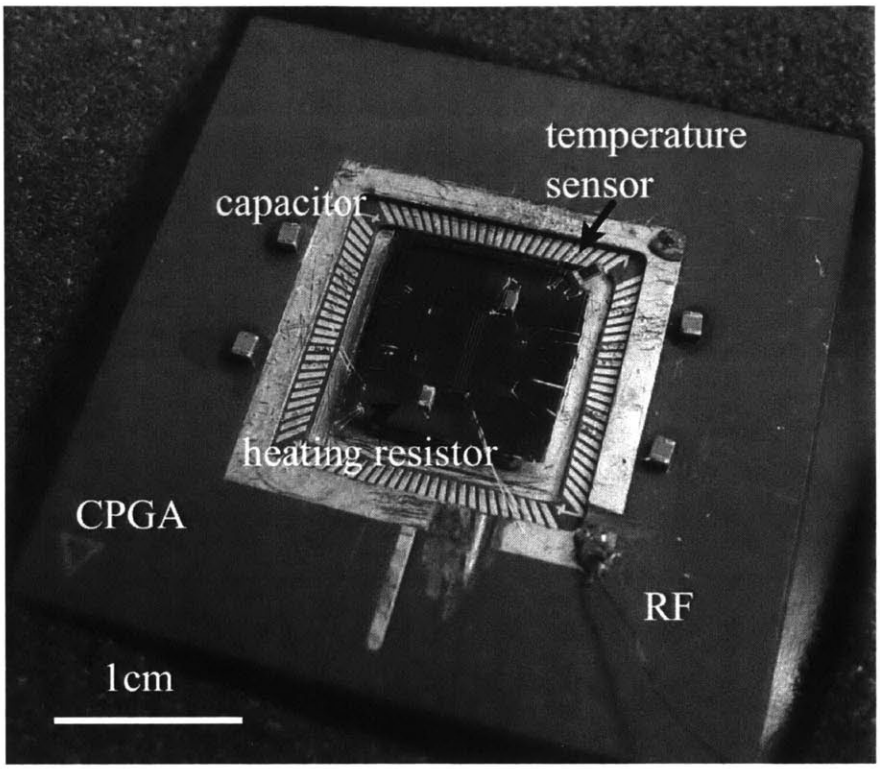

Figure 3-11: A niobium trap is mounted and wire bonded in a CPGA. Heating resistors and RuO_2 temperature sensor are also mounted to the niobium ion trap surface.

a specific amount of force. It works well on niobium, copper, silicon and aluminum pads. However, the aluminum wedge bonding is directional, and the tip is bigger.

Chapter 4

Ion Motional Heating Rate and its Relation to Fabrication Processes

Trapped ion quantum computation faces several challenges. One is to reduce trap size as discussed in Chapter 3, by using microfabrication techniques to miniaturize ion traps with planar geometry. Another big obstacle is decoherence. In trapped ion quantum computation experiments, decoherence is dominated by the uncontrolled heating of ion motional states which is a consequence of the electric field noise at the ion position. As the trap size becomes smaller, the ion gets closer to the trap electrode surface, and the electric field noise from the trap electrodes has greater influence on the ion. In this chapter, two different ion heating sources, the thermal electric noise and fluctuating patch potential noise, are presented. Different ion heating source results in different distance, temperature and frequency dependence behaviors. A physical model based on the fluctuating patch potential theory is proposed, and the relationship between ion heating and fabrication process is discussed, seeking ways to suppress excess ion heating.

Section 4.1 starts with the statement that an ion will be heated when the frequency spectrum of the noisy electric field at the ion position overlaps the secular frequency [TKK+00]. The Hamiltonian for a trapped ion subject to a fluctuating electric field is then introduced. Using perturbation theory, the motional heating is shown related to the power spectral density of electric field fluctuation. Thus noisy electric field can

be used as a probe to investigate ion heating.

Section 4.2 first presents two different ion heating sources. Source one is the thermal electric noise. The thermal electric noise derived using fluctuation-dissipation theorem is a thermal noise related to temperature and resistance in trap electrodes and connecting circuits [Nyq28]. It is independent of frequency. However, at cryogenic temperature, the resistance of thin trap electrode deviates from bulk value, and contributions from surface scattering [Son52] and grain boundary scattering [AM70] are discussed in detail. The magnitude of the ion heating due to thermal electric noise is estimated. Source two is the fluctuating patch potential noise. It is due to the randomly distributed patches with fluctuating potentials which are caused by varying work functions or adsorbate dipole fluctuations [TKK+00]. Based on the fluctuating patch potential theory, a model is proposed to derive the frequency dependence and temperature dependence of the dipole fluctuation spectrum. The consideration of grain size and grain orientation is introduced. The effect of thin amorphous dielectric layer on ion heating is also discussed.

Section 4.3 discusses the relationship between ion heating and fabrication process. We finally conjecture that ion heating could possibly be suppressed by properly choosing electrode materials and corresponding fabrication process.

4.1 Ion Motional Heating Rate and Electric Field Noise

As a building block of a quantum computer, ion trap uses coherent superposition of atomic state and motional state to encode information. According to the DiVincenzo criteria [DiV00], the speed and fidelity of an operation are limited by the decoherence of the quantum superposition states. In trapped ion quantum computation experiments, the decoherence is composed of qubit state decoherence and motional state decoherence, in which uncontrolled heating of motional states is the dominant one. As shown in Section 2.6.1, ion is trapped above the planar electrode surface in a har-

monic potential generated by oscillating and static electric fields. When the frequency spectrum of the fluctuating electric field at the ion position overlaps the trap secular frequency, the secular motion of the ion will be heated due to the noisy electric field [TKK+00]. In ion heating measurement, trapped ion will first be cooled to its ground motional state by Doppler cooling and resolved sideband cooling. The ion heating rate is then defined as the gained motional quantum number in a given time.

The Hamiltonian for a trapped ion at oscillating frequency ω_ν is $H_0 = \hbar\omega_\nu \left(a^\dagger a + \frac{1}{2}\right)$. When the trapped ion is subject to a uniform fluctuating electric field $\epsilon(t)$, the Hamiltonian is changed to

$$H(t) = H_0 + q\epsilon(t)\, x = \hbar\omega_\nu \left(a^\dagger a + \frac{1}{2}\right) + q\epsilon(t)\, x_0 \left(a^\dagger + a\right) \tag{4.1}$$

where $x_0 = \sqrt{\frac{\hbar}{2m\omega_\nu}}$, q and m are the charge and mass of the trapped ion. $a^\dagger$ and a are raising and lowering operators.

The transition rate from the ground state $|n=0\rangle$ to the first excited state $|n=1\rangle$ is calculated using the first order perturbation theory [TST97].

$$\Gamma_{0\to 1} = \frac{q^2}{\hbar^2}\int_{-\infty}^{\infty} d\tau e^{i\omega_\nu \tau} \langle \epsilon(t)\, \epsilon(t+\tau)\rangle \left|\langle 0|x_0\left(a^\dagger + a\right)|1\rangle\right|^2 \tag{4.2}$$

where τ is the time lag.

The definition of the power spectral density of the fluctuating electric field is

$$S_E \equiv 2\int_{-\infty}^{\infty} d\tau e^{i\omega\tau} \langle \epsilon(t)\, \epsilon(t+\tau)\rangle \tag{4.3}$$

where $\langle \epsilon(t)\, \epsilon(t+\tau)\rangle = \int_0^\infty dt \epsilon(t)\, \epsilon(t+\tau)$ is the autocorrelation function of the fluctuating electric field and ω is the frequency of the electric field. Thus the heating rate is given by

$$\dot{\bar{n}} = \frac{q^2}{4m\hbar\omega_\nu} S_E(\omega_\nu) \tag{4.4}$$

where $\dot{\bar{n}}$ is the rate of change of the average motional quantum number.

The above calculation [TST97] is based on ion motion in an ideal harmonic po-

tential with frequency ω_ν. Ion traps use an oscillating RF potential at frequency Ω to produce the dynamic secular potential, thus there are additional contributions to heating from the coupling of RF and noise fields [WMI+98]. The ion heating has two terms

$$\dot{\bar{n}} = \frac{q^2}{4m\hbar\omega_\nu}\left(S_E(\omega_\nu) + \frac{\omega_\nu^2}{2\Omega^2}S_E(\Omega \pm \omega_\nu)\right) \tag{4.5}$$

However, since $\frac{\omega_\nu^2}{\Omega^2} \approx \frac{1}{4}a + \frac{1}{8}q^2$ and Mathieu $|q| \ll 1$, the second term $\frac{\omega_\nu^2}{2\Omega^2}S_E(\Omega \pm \omega_\nu)$ can be ignored. Thus the power spectral density of electric field fluctuation might be used as a probe to investigate the sources of ion heating.

4.2 Sources of Electric Field Noise

There are most likely mainly two ion heating sources that are widely accepted. Each has a different heating behavior due to the different microscopic origin. The different microscopic origin thus results in different scaling behavior, temperature dependence and frequency spectrum.

4.2.1 Thermal Electronic Noise

One of the ion heating sources is the so called Johnson-Nyquist noise which is a type of thermal noise derived using fluctuation-dissipation theorem. Johnson noise in a solid is caused by fluctuations in the velocity of electrons at thermal equilibrium. Thus the Johnson noise is related to the temperature and resistance of the conductor.

The power spectral density of Johnson noise is [Nyq28]

$$S_V(\omega) = 4k_BTR(\omega) \tag{4.6}$$

where k_B is Boltzmann's constant, T is the temperature and $R(\omega)$ is the resistance of conductor. In the case of ion traps, ω is the secular frequency.

Since $E \propto \frac{V}{d}$, the power spectral density of electric field is

$$S_E(\omega) = \frac{4k_BTR(\omega)}{d^2} \tag{4.7}$$

where d is the characteristic distance from the trap electrode to the ion and $R(\omega)$ is the resistance in trap electrodes and connecting circuits.

A microscopic model can give a more precise electric field fluctuation for arbitrary ion-electrode distance using fluctuation-dissipation theorem [TKK+00]. The thermal electric field noise in a plane parallel to the electrode surface and at a distance d from the surface is

$$S_E(\omega, d) = \frac{k_B T \rho}{8\pi d^3} \left(\frac{1}{2} + \sqrt{\frac{1}{4} + \frac{d^4}{\delta^4}} \right)^{\frac{1}{2}} \tag{4.8}$$

where ρ is the resistivity of conducting electrodes and δ is the skin depth. The skin depth is well approximated as

$$\delta = \sqrt{\frac{2\rho}{\omega\mu}} \tag{4.9}$$

where μ is the absolute magnetic permeability of the conductor. Figure 4-1(a) shows the skin depth for various materials subjected to electric fields of different frequencies at room temperature. Figure 4-1(b) shows the skin depth for various materials at cryogenic temperature. Thus the skin depth is approximately $50 - 100$ μm at 1 MHz for a good conducting electrode material at room temperature, and is dramatically reduced to $1 - 5$ μm at cryogenic temperature, which is the same order of magnitude as our electrode thickness.

At cryogenic temperature, $\delta \ll d$, the thermal electric field noise can be simplified to

$$S_E(\omega) = \frac{k_B T \rho}{8\pi \delta d^2} \tag{4.10}$$

The power spectral density of noisy electric field scales as $\frac{1}{d^2}$ at cryogenic temperature.

The typical Johnson thermal noise is approximately white, meaning that the power spectral density is independent of frequency.

When calculating Johnson noise, bulk resistivity is often used. However, when dealing with thin metal film at cryogenic temperature, resistivity deviates from the bulk value. When conductor has a dimension on the order of the mean free path of electrons, it will exhibit higher resistivity than bulk conductor. The mean free path for conducting electrons in gold is approximately 40 nm at room temperature. At

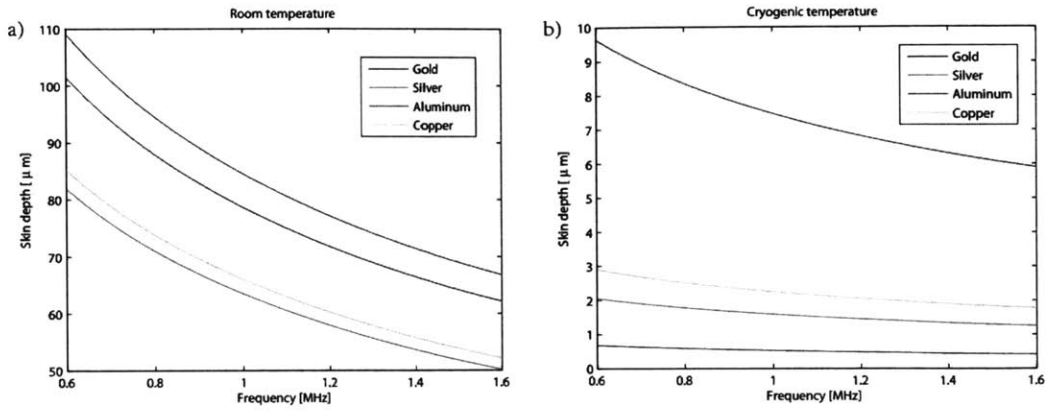

Figure 4-1: (a) Skin depth for gold, silver, aluminum and copper subjected to electric fields of different frequencies at room temperature. (b) Skin depth for gold, silver, aluminum and copper subjected to electric fields of different frequencies at cryogenic temperature.

cryogenic temperature 4.2 K, the resistivity decreases resulting in a mean free path of about 4 μm. The mean free path of conducting electrons is on the same order of magnitude as our trap electrode thickness and deviation from the bulk resistivity needs to be considered.

The temperature dependence of bulk resistivity ρ_i can be achieved using the Bloch-Gruneisen model [JBS90].

$$\rho_i(T) = \rho(0) + A\left(\frac{T}{\Theta_D}\right)^5 \int_0^{\frac{\Theta_D}{T}} \frac{x^5}{(e^x - 1)(1 - e^{-x})} dx \tag{4.11}$$

where $\rho(0)$ is the residual resistivity due to defect scattering, and Θ_D is the Debye temperature. In a high temperature regime ($T > \Theta_D/10$), the resistivity $\rho_i(T)$ is proportional to T due to electron-phonon scattering, however, in a low temperature regime ($T \ll \Theta_D/10$), the resistivity $\rho_i(T)$ is proportional to T^5. For gold, numerical calculation shows that $\rho_i \propto T$ when $T > 30$ K.

When the electrode dimension is on the same order of magnitude as the mean free path of electrons, surface and grain boundary scattering become important.

The contribution from surface scattering ρ_{FS} can be described by the Fuchs and

Sondheimer model [Son52].

$$\rho_{FS} = \rho_i \left[1 - \left(\frac{3\lambda}{2t} \right) (1-p) \int_1^\infty \left(\frac{1}{t^3} - \frac{1}{t^5} \right) \frac{1 - \exp\left(-\frac{tx}{\lambda}\right)}{1 - p\exp\left(-\frac{tx}{\lambda}\right)} dx \right]^{-1} \tag{4.12}$$

where t is the thickness of the conductor, p is a specular scattering coefficient and λ is the mean free path of the conducting electrons due to phonon and impurity scattering. Those electrons that scatter diffusely will contribute to the increased resistivity. When the surface becomes rough, more electrons scatter diffusively to increase the resistivity. When $t > \lambda$, $\rho_{FS} = \rho_i \left[1 + \frac{3(1-p)\lambda}{8t} \right]$. When $t < \lambda$, $\rho_{FS} = \frac{4\rho_i(1-p)\lambda}{3t(1+p)} \times \left[\ln\left(\frac{\lambda}{t}\right) + 0.4228 \right]$.

The contribution from grain boundary scattering ρ_{MS} can be described by the Mayadas and Shatzkes model [AM70].

$$\rho_{MS} = \rho_i \left[1 - \frac{3}{2}\alpha + 3\alpha^2 - 3\alpha^3 \ln\left(1 + \frac{1}{\alpha}\right) \right]^{-1} \tag{4.13}$$

where $\alpha = \frac{\lambda}{g} \frac{R}{1-R}$. λ is the mean free path of conducting electrons, g is the average grain size and R is the reflection coefficient which gives the reflection probability at the grain boundary. The electron reflection coefficient for gold is about 0.2 [AM70]. The resistivity will be approximately increased by 10 times when the grain size is changed from 2 μm to 40 nm. As shown in Figure 4-2, when the grain is bigger than 1 μm, grain size has less effect on the resistivity due to grain boundary scattering.

When the film is thin and grain size is small, at cryogenic temperature, the resistivities due to surface and grain boundary scattering are dominant. Figure 4-3 shows the comparison of the temperature dependence of the resistivities due to different origins. When the free mean path decreases as temperature goes up, the resistivities due to the surface and grain boundary scattering become approximately constant. While at room temperature, the bulk resistivity becomes dominant. When film is thick and grain size is big, the surface and grain boundary scattering will be reduced.

At cryogenic temperature, the Johnson thermal noise should take all these excess resistivities into account. Assuming the electrode has a dimension 6 mm × 100 μm × 1 μm and ion-electrode distance is $d = 100$ μm, if only bulk resistivity is considered,

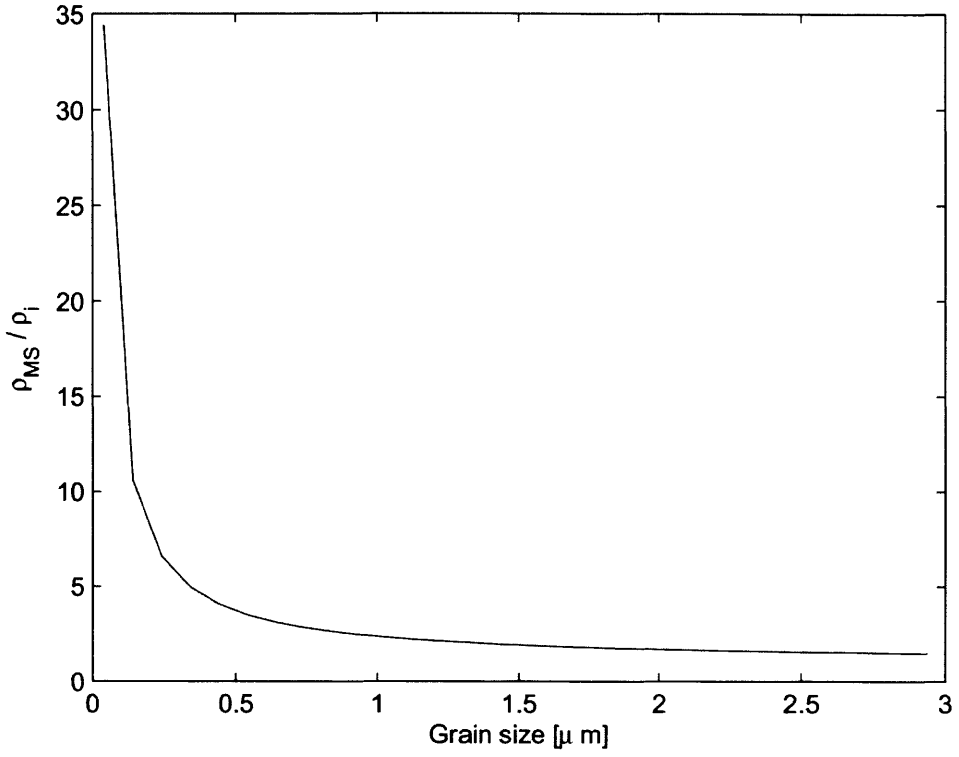

Figure 4-2: Grain size dependence of resistivity contribution from grain boundary scattering. When the grain is bigger than 1 μm, grain size has less effect on the resistivity due to grain boundary scattering.

$S_E \approx 5 \times 10^{-20}$ V^2/m^2/Hz. If all excess resistivities are considered, S_E could be increased by one order of magnitude.

Beside the white Johnson thermal noise, there are some other $1/f$ noises inside metal, which are illustrated by the phenomenological equation [DH81]

$$S_V(f) = \gamma \frac{\langle V \rangle^2}{N_c f} \tag{4.14}$$

where N_c is the number of carriers in the conductor, $\langle V \rangle$ is the average voltage across the electrode and γ is a dimensionless constant with $\gamma \approx 2 \times 10^{-3}$. Comparing to the white Johnson noise, this flicker noise is larger at lower frequencies and appears to be non-thermal. In addition, this excess flicker noise S_V is proportional to $\langle V \rangle^2$ and

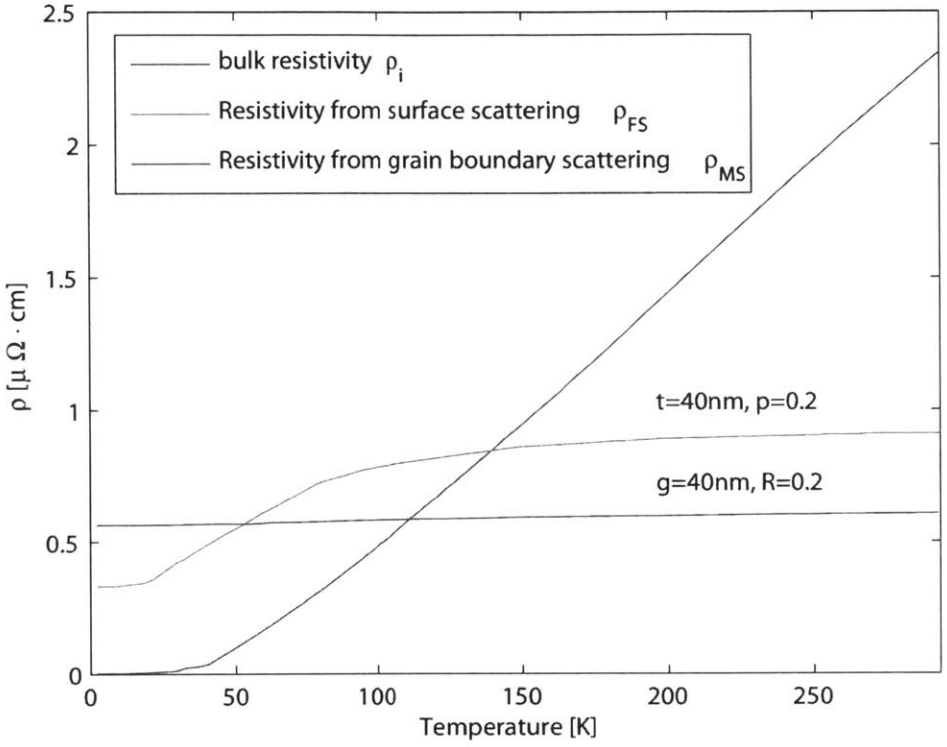

Figure 4-3: Comparison of the temperature dependence of the resistivities ρ_i, ρ_{FS} and ρ_{MS}. ρ_i is the bulk resistivity of gold. ρ_{FS} and ρ_{MS} are the resistivities of a 40 nm thick gold film with 40 nm grain size due to surface scattering and grain boundary scattering. At cryogenic temperature, surface and grain boundary scattering are dominant when the grain size and film thickness are small compared to the mean free path.

is inversely proportional to the sample volume, which means this $1/f$ noise is a bulk effect rather than a surface effect.

Assuming the electrode has a dimension 6 mm $\times$ 100 μm $\times$ 1 μm, $N_c = 3.6 \times 10^{16}$. With $\langle V \rangle^2 = 1$ V^2, $f = 1$ MHz and ion-electrode distance $d = 100$ μm, $S_E \approx 5 \times 10^{-18}$ V^2/m^2/Hz.

4.2.2 Fluctuating Patch-Potential Noise

The second ion heating source is due to randomly distributed patches with fluctuating discontinuous potentials. There are several possible physical origins for these fluctu-

ating potentials. Real metal surface consists of a number of areas of different crystal orientations. The electric double layer is formed at the metal surface, varying from crystal plane to crystal plane and resulting in different work function [CDB91]. Additional surface double layer arises from adsorption. The potential fluctuations may also be due to the adsorbate dipole fluctuations [RO92]. Thus the patch potential fluctuation is not a bulk but a surface phenomenon.

A simple model is given by Turchette et al.[TKK+00]. Trap electrodes are assumed to form a sphere with radius d around the ion. Small patches with radius $r_p \ll d$ are on the inner surface of the sphere. For a single patch with potential V, the electric field at the ion is $E = \frac{V}{\sqrt{d^2+r_p^2}} \approx \frac{V}{d} - \frac{Vr_p^2}{2d^3}$. The electric field noise at the ion due to a single patch with electric potential noise V_p in the direction perpendicular to the patch is

$$E_p(\omega) = -\frac{V_p(\omega) r_p^2}{2d^3} \tag{4.15}$$

Averaging over $N \propto C \times \frac{d^2}{r_p^2}$ randomly distributed patches (where C is the coverage), the power spectral density of the electric field at the ion due to the power spectral density of patch potential $S_V(\omega)$ is

$$S_E(\omega) \propto N \left(\frac{\partial E_p(\omega)}{\partial V_p(\omega)}\right)^2 S_V(\omega) \propto \frac{C r_p^2}{d^4} S_V(\omega) \tag{4.16}$$

which indicates that the power spectral density of the noisy electric field scales as d^{-4}.

This simple patch potential model is further improved by Dubessy et al. with introducing a correlation length ς of the electric potential [RDG09]. This correlation length ς of the noisy potential on the trap electrode surface enables taking the spatial dependence of the noisy electric field into account. Small patches, each with a time dependent electric potential V_i on the area C_i, are randomly distributed on the $x-y$ plane creating a disordered electric potential on trap electrode surface. The spatial autocorrelation function C_ς of the patches has an exponential behavior

$$C_\varsigma(x,y) = e^{-\sqrt{x^2+y^2}/\varsigma} \tag{4.17}$$

The power spectral density of the electric field at the ion due to the potential noise is

$$S_E(\omega, d) = 2\frac{N\varsigma^2}{d} S_V(\omega) \int_0^\infty dk \frac{k^3 e^{-2k}}{(d^2 + \varsigma^2 k^2)^{3/2}} \tag{4.18}$$

where k is introduced by taking Fourier transform of spatial domain. d is the ion-electrode distance and N is the number of patches. S_V is the potential noise.

$$S_E(\omega, d) \approx \begin{cases} \frac{S_V(\omega)}{d\varsigma}, & \text{if } d \ll \varsigma \\ \frac{3\varsigma^2 S_V(\omega)}{4d^4}, & \text{if } d \gg \varsigma \end{cases} \tag{4.19}$$

Both models indicate that the patch size plays an important role in determining the final electric field fluctuation spectrum.

If we consider the single patch as a dipole with dipole moment $\vec{p}$ pointing in random direction normal to the patch surface. The electric field at the position $\vec{r}$ is

$$\vec{E}(\vec{r}) = \frac{1}{4\pi\varepsilon_0} \left(\frac{3(\vec{p} \cdot \hat{r})\hat{r} - \vec{p}}{r^3} \right) \tag{4.20}$$

Assuming that the surface dipole density is ρ_s and $\langle p \rangle = 0$, the expected value of the electric field in the direction normal to the patch surface averaging over randomly pointed dipoles is

$$\langle \left(\vec{E} \cdot \hat{z} \right)^2 \rangle = \frac{2\pi\rho_s \langle p^2 \rangle}{(4\pi\varepsilon_0)^2} \int_0^\infty \frac{(2d^2 - R^2)^2}{(R^2 + d^2)^5} RdR = \frac{3\pi\rho_s \langle p^2 \rangle}{(4\pi\varepsilon_0)^2 4d^4} \tag{4.21}$$

where R is the patch radius and d is the ion-electrode distance. The power spectral density of the electric field at the ion due to the power spectral density of patch dipole $S_p(\omega)$ is

$$S_E(\omega) = \frac{3\pi\rho_s}{(4\pi\varepsilon_0)^2 4d^4} S_p(\omega) \tag{4.22}$$

However, this patch potential model fails to describe the temperature dependence of the power spectral density of the noisy electric field via patch size. Although the fluctuating patch potential noise is a surface phenomenon, all the above models fail to exhibit surface property dependence, for example, the dependence on grain size and

grain orientation. In this work, a model is proposed trying to explain the different temperature dependence behaviors and surface property dependence behaviors we have observed in our ion heating measurement.

The metallic thin films that we use as surface electrodes are composed of grains with different orientations separated by grain boundaries. Grains with different orientations have different crystal planes. At the metal surface, electrons spill out forming a negative dipole layer [NL71], thus the work function is the sum of bulk chemical potential and the dipole potential at the surface [WB35]. The work function varys from crystal plane to crystal plane and can differ by amount from 0.1 eV to 0.5 eV [Lid08]. When a layer of adsorbates is present, an additional dipole layer is formed affecting the total work function. Adatom is adsorbed on the metal surface and thus is trapped in a harmonic surface potential [ASNS11]. Adatom adsorbed on the metal surface has a dipole moment perpendicular to the surface. Being trapped in different vibrational bound surface states will result in different distortion of the electronic wavefunctions and give rise to fluctuating dipole moments. The transition between different vibrational bound states is assisted by phonons inside the metal and is a thermal activation process.

To derive the frequency and temperature dependence of the dipole fluctuation spectrum, assume that the thermal activation process has a characteristic time τ [DH81]. τ is thermally activated,

$$\tau = \tau_0 e^{\frac{\epsilon}{k_B T}} \tag{4.23}$$

where ϵ is the activation energy and τ_0 is the transition attempt time. The dipole fluctuation spectrum has a Debye-Lorentzian shape [DH81].

$$S_p(\omega) = \langle (\delta p)^2 \rangle \frac{4\tau}{\omega^2 \tau^2 + 1} \tag{4.24}$$

where $\langle (\delta p)^2 \rangle$ is the variance of dipole.

Since the fluctuating patch potential is a surface phenomenon, we propose a physical model to extend the patch potential theory by taking grain size and grain orien-

tation into account.

For grains with different orientations, different surface electron densities will result in different surface dipole potentials and different additional dipole potentials caused by adsorbates. If we assume that the electrode is composed of grains with n different orientations. For grains with i^{th} orientation, $i = 1, 2, 3, ..., n$, grains have a dipole p_i and the ratio of the number of grains with this particular orientation to the total number of grains is P_i. The total number of grains is N.

Thus the variance of dipole $\langle (\delta p)^2 \rangle$ can be calculated by

$$\langle (\delta p)^2 \rangle = \frac{1}{N} \left[\sum_{i=1}^{n} P_i p_i^2 - \left(\sum_{i=1}^{n} P_i p_i \right)^2 \right] \tag{4.25}$$

When the electrode has only two grain orientations, the model is simplified. Assume n_1 and n_2 are the random numbers of grains with a dipole p_1 and p_2 respectively. P_1 and P_2 are the corresponding possibilities of a grain with a particular orientation. $n_1 + n_2 = N$ and $P_1 + P_2 = 1$.

The probability of getting $n_1 = k$ grains is

$$f(n_1 = k) = \frac{N!}{k!\,(N-k)!} P_1^k (1 - P_1)^{N-k} \tag{4.26}$$

And the corresponding average dipole is

$$p(n_1 = k) = \frac{1}{N} [k p_1 + (N - k) p_2] \tag{4.27}$$

Thus the distribution of dipole can be calculated and it has a binomial distribution.

By integrating Equation 4.24 over $D(\tau)$ which is the distribution of relaxation times τ, the dipole noise is given by

$$S_p = \int \langle (\delta p)^2 \rangle \frac{4\tau}{\omega^2 \tau^2 + 1} D(\tau)\, d\tau \tag{4.28}$$

Using Equation 4.23 and $D(\tau)\, d\tau = D(\epsilon)\, d\epsilon$ where $D(\epsilon)$ is the distribution of acti-

vation energies ϵ, Equation 4.28 can be rewritten as

$$S_p = \int \langle (\delta p)^2 \rangle \frac{4\tau_0 e^{\frac{\epsilon}{k_B T}}}{\omega^2 \left(\tau_0 e^{\frac{\epsilon}{k_B T}}\right)^2 + 1} D(\epsilon)\, d\epsilon = \frac{2}{\omega} \int \langle (\delta p)^2 \rangle \frac{D(\epsilon)}{\cosh\left[(\epsilon - \bar{\epsilon})/k_B T\right]} d\epsilon \quad (4.29)$$

where $\bar{\epsilon} = -k_B T \ln(\omega\tau_0)$. The spectrum $\frac{1}{\cosh[(\epsilon-\bar{\epsilon})/k_B T]}$ peaks at $\bar{\epsilon}$ with a width of $k_B T$.

If the distribution $D(\epsilon)$ has a width $>> k_B T$, $D(\epsilon)$ varies slowly around $\bar{\epsilon}$ and $D(\epsilon) \approx D(\bar{\epsilon})$. If we assume that $\langle (\delta p)^2 \rangle$ is expected not to depend strongly on ϵ, we have

$$S_p(\omega) = \langle (\delta p)^2 \rangle \frac{k_B T}{\omega} D(\bar{\epsilon}) \quad (4.30)$$

All simplifications are based on the assumption that $D(\epsilon) \approx$ constant. In order to keep $\bar{\epsilon} = -k_B T \ln(\omega\tau_0)$ and $D(\bar{\epsilon}) \propto \frac{\omega}{k_B T} S_p(\omega, T)$ unchanged [DH81],

$$\left(\Delta\omega \frac{\partial}{\partial\omega} + \Delta T \frac{\partial}{\partial T}\right) [k_B T \ln(\omega\tau_0)] = 0 \quad (4.31)$$

$$\left(\Delta\omega \frac{\partial}{\partial\omega} + \Delta T \frac{\partial}{\partial T}\right) [\omega S_p(\omega, T)/k_B T] = 0 \quad (4.32)$$

If we assume $S_p(\omega, T) \propto \omega^{-\alpha}$. Solving these two equations gives

$$\alpha(\omega, T) = 1 - \frac{1}{\ln(\omega\tau_0)} \left(\frac{\partial \ln S_p(\omega, T)}{\partial \ln T} - 1\right) \quad (4.33)$$

where $\omega^{-\alpha}$ is the frequency dependence of the dipole fluctuation spectrum. α has a weak dependence on temperature. For typical $\tau_0 = 10^{-14}$s in solid, $|\ln(\omega\tau_0)| \gg 1$ and $\alpha \approx 1$. If distribution $D(\epsilon)$ is explicitly temperature dependent $D(\epsilon, T)$, frequency dependence α will deviate from 1.

If the distribution $D(\epsilon)$ has a width $<< k_B T$, since $\tau = \tau_0 e^{\frac{\epsilon}{k_B T}}$, Equation 4.24 can be rewritten as

$$S_p(\omega) = \langle (\delta p)^2 \rangle \frac{4\tau}{\omega^2\tau^2 + 1} = 4\langle (\delta p)^2 \rangle \frac{\tau_0 \exp(-\epsilon/k_B T)}{\exp(-2\epsilon/k_B T) + \omega^2\tau_0^2} \quad (4.34)$$

In the region $\omega\tau_0 \ll \exp(-\epsilon/k_B T)$, the spectrum is frequency independent. On the contrary, in the region $\omega\tau_0 \gg \exp(-\epsilon/k_B T)$, the spectrum has ω^{-2} scaling.

An intermediate frequency region is between these two exhibiting an ω^{-1} scaling. When $\omega\tau_0 \geq \exp(-\epsilon/k_BT)$ and the characteristic time $\tau_0 \gg 10^{-14}$s, the fluctuation spectrum exhibits an Arrhenius temperature dependence

$$S_p(\omega) \propto \langle(\delta p)^2\rangle e^{-\epsilon/k_BT} \tag{4.35}$$

As demonstrated above, in Equation 4.30, the $1/\omega$ spectrum is a result of really broad distribution of relaxation times τ. However, when the distribution is in narrow range, the fluctuation spectrum can exhibit a totally different Arrhenius temperature dependence.

When there is a thin amorphous dielectric layer on top of the metal electrode surface, in addition to the dipole fluctuations due to adsorbate atoms that we have discussed above, tunneling mechanism also needs to be taken into account. Electrons trapped inside the amorphous dielectric layer form two level systems [Phi87, DHP13], and switching between two levels also results in dipole fluctuations. As shown in Equation 4.22, the power spectral density of electric field $S_E(\omega)$ is proportional to the surface dipole density ρ_s. With the presence of the thin amorphous dielectric layer, the noisy electric field spectrum is proportional to ρ_{TLS}, the density of tunneling two level systems inside the dielectric layer, which is closely related to the defect density. Electrons tunneling through the amorphous dielectric layer have probabilities being trapped inside forming tunneling two level systems. The probability of being trapped is proportional to $1 - e^{-\frac{d}{\delta}}$, where d is the thickness of the dielectric layer and δ is the characteristic length of the tunneling.

The correlation between the excess electric field noise due to the presence of the amorphous dielectric layer and the dielectric layer thickness is

$$S_p \propto \rho_{TLS}\left(1 - e^{-\frac{d}{\delta}}\right) \tag{4.36}$$

Equation 4.36 indicates that there will be a saturation of the excess noisy electric field spectrum when the thickness of the dielectric layer d exceeds the characteristic tunneling length δ.

4.3 Ion Motional Heating Rate Dependence on Fabrication Process

There are mainly two sources accounting for the ion heating. The thermal electric noise has a d^{-2} scaling. This white noise is determined by temperature and the resistance in trap electrodes and connecting circuits. At cryogenic temperature, thermal electric noise will be significantly suppressed since resistivity is strongly temperature dependent. At room temperature, the resistivity is very close to the bulk resistivity, however, large excess resistivity arises when temperature goes to cryogenic region due to the surface and grain boundary scattering, especially when the electron mean free path is comparable to the grain size and electrode thickness. In order to reduce the thermal electric noise of ion trap operated at cryogenic temperature, the excess resistivity which can be measured via the residual resistance ratio (RRR) needs to be considered during fabrication.

The second ion heating source is the fluctuating patch potential noise. In contrast to thermal electric noise, the fluctuating patch potential noise is rather a surface phenomenon than a bulk one and is frequency dependent. The patch potential noise has a d^{-4} scaling, thus it becomes more important when the ion electrode distance gets smaller comparing to the d^{-2} scaling of thermal electric noise. According to the temperature dependence of the patch potential noise discussed in Section 4.2.2, it can also be dramatically reduced when operating ion trap at cryogenic temperature. Since the patch potential noise is a surface phenomenon, it is determined by the grain orientation, patch size, surface adsorption, surface oxidation and surface contamination, which are strongly related to the fabrication process. Thus suitable fabrication process is key to suppress the excess ion heating.

As for the grain orientation, according to Equation 4.25, there are several ways to suppress the ion heating. One way is to increase the total number of grains N. As N increases, the dipole variance decreases. In fabrication process, deposition of metal at lower temperature can reduce the grain size increasing N. The dipole variance could also be reduced, if $p_1 \approx p_2 \approx ... \approx p_n$. This can be achieved by choosing proper

electrode materials which have same work function regardless of the grain orientations. Another way is to control the grain orientations. If the metallic electrode is mainly composed of grains with one particular orientation. For example, in Equation 4.25, if $P_1 \gg P_i$ ($i = 2, 3, ..., n$), the dipole variance will be dramatically reduced. Details are discussed in Chapter 5.

The surface contamination due to the organic solvent cleaning is also an issue. Orders of magnitude variations on ion heating rate have been observed in the same trap after it has been recleaned. The cleaning process of the ion trap electrode surface is possibly as important as the fabrication process itself, which has also been confirmed by other groups [DHP13].

4.3.1 Electrode Materials

There are several options for choosing ion trap electrode materials. Superconducting materials could be chosen to reduce the thermal electric noise when operated in the superconducting state at cryogenic temperature. Noble metals including gold and silver are resistant to corrosion and oxidation in air. Especially, when the metal has full filled d-bands structure that does not cross the Fermi level [EH05], the metal intends to have a clean surface. Copper also has full filled d-bands, however, the chemical nobility is lower comparing to gold and silver. Aluminum and copper form a passivation layer of metal oxide at the metal surface which is only a few atoms thick. The oxide layer binds tightly to the metal surface passivating the metal against further oxidation. It seems that the thin amorphous passivation layer doesn't affect ion heating too much since the ion heating rates of aluminum and copper traps are on the same order of magnitude as those of gold traps. However, porous oxide layer grown by Ebeam evaporation does increase the ion heating rate due to the trapped electrons in the dielectric layer. Molybdenum is a promising electrode material, since it has the same work function regardless of the grain orientations. Thus the reduced dipole variance could possibly suppress the ion heating.

4.3.2 Electrode Morphology

Once the electrode materials are chosen, corresponding fabrication processes need to be carefully designed. Different fabrication process will result in different electrode morphology and grain structure giving rise to different ion heating behavior. In the case of the patch potential noise, the dipole spectrum is strongly related to the patch size and grain orientation distribution.

When electrode materials are deposited by Ebeam evaporation or sputtering, deposition of metal at lower temperature can reduce the grain size increasing N. As for the deposition method, sputtering will achieve smaller grains than Ebeam evaporation. Usually, the grain size is limited by the film thickness. For example, when 400 nm aluminum is evaporated on the quartz substrate, the average grain size will be less than 400 nm. If electrode materials are deposited using electroplating, the grain size is mostly determined by the plating current and agitation. The grain size decreases with increasing plating current density. The grain size could be further reduced using pulse electroplating.

The distribution of grain orientations is mainly determined by material properties and deposition conditions. We can manipulate the grain orientations by the thermal annealing after deposition. In our experiments, Ebeam evaporated silver traps are annealed at two different temperatures resulting in two different grain structures. The ion heating rates are seen to differ by two orders of magnitude. This is discussed in detail in Section 5.4.

Chapter 5

Ion Motional Heating Rate Measurement

In this chapter, we first describe the measurement method for ion heating rate, followed by a brief introduction about the measurements of the distance, frequency and temperature dependence of the ion heating rate in Section 5.1. Section 5.2 presents the ion heating measurement results for electroplated gold traps both at cryogenic temperature and at room temperature. The measurements of temperature and frequency dependence of ion heating rate are conducted in the temperature range of 6 K to 120 K, and the frequency dependence also shows a weak temperature dependence. Section 5.3 presents the ion heating measurement results for aluminum traps with native oxide layer and with evaporated oxide layer of different thickness. The ion heating rate saturates when the evaporated oxide layer is thicker than a characteristic length of the tunneling. Section 5.4 presents the ion heating measurement results for silver traps annealed at 720°C and 760°C. The inferred values of electric field noise are strongly dependent on the annealing temperature and are seen to differ by two orders of magnitude. Section 5.5 presents the ion heating measurement results for niobium traps at cryogenic temperature. This chapter closes with the comparison of ion heating rates between ion traps made by different materials and fabrication processes.

5.1 Ion Motional Heating Rate Measurement Method

To measure the ion heating rate, the trapped ion is first cooled to its motional ground state. A single $^{88}Sr^{+}$ ion is loaded by photonionization and trapped 75 $\sim$ 100 μm above the trap electrode. The ion is Doppler cooled to < 1 mK by the $5^2S_{1/2} \rightarrow 5^2P_{1/2}$ transition. It is further cooled by resolved sideband cooling on the $5S_{1/2}(m = -1/2) \rightarrow 4D_{5/2}(m = -5/2)$ transition to its motional ground state (as described in Section 2.5.2). The ground motional state is reached when the average number of quanta is less than 1. Once the ground motional state is achieved, the ion heating rate is measured by measuring the average motional quantum number gained with a varied delay time. The expectation value of motional quantum number is determined by measuring relative transition probabilities on blue and red sidebands using a properly detuned laser pulse. The transition probabilities are obtained by repeating the cooling and probing cycles 100 times.

As described in Section 2.5.2, the expectation value of the motional quantum number is

$$\bar{n} = \frac{P_{RSB}}{P_{BSB} - P_{RSB}} \tag{5.1}$$

The transition probabilities on both red (P_{RSB}) and blue (P_{BSB}) motional sidebands are measured immediately after sideband cooling and after a delay time. In order to get the ion heating behavior, different delay time is added between the cooling cycle and the probing cycle. Figure 5-1 shows the expectation value of motional quantum number as a function of delay time, which can be linearly fitted to get the ion heating rate $\dot{\bar{n}}$ in quanta/second unit. Then the heating rate is converted to the power spectral density of the electric field using Equation

$$S_E(\omega_\nu) = \frac{4m\hbar\omega_\nu}{q^2}\dot{\bar{n}} \tag{5.2}$$

where ω_ν is the secular frequency. q and m are the electric charge and mass of the ion.

As shown in Section 4.2, different ion heating sources will have their intrinsic ion-

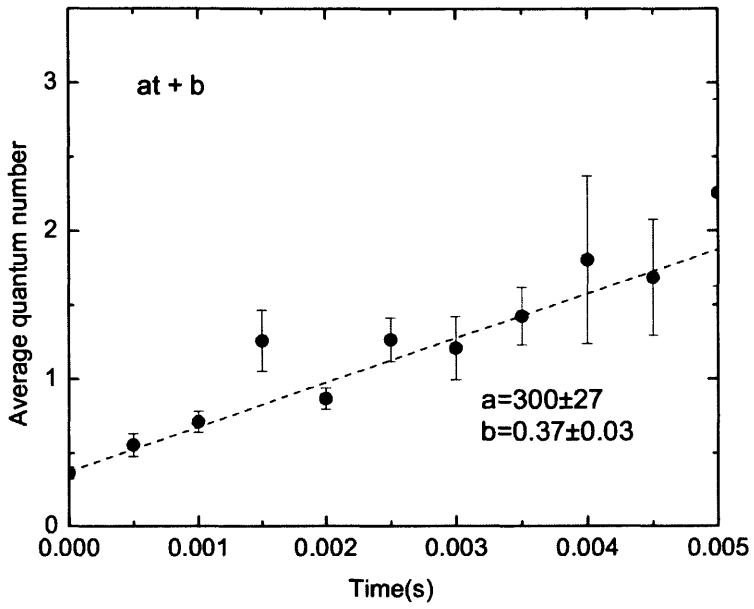

Figure 5-1: Average motional quantum number versus delay time. The ion heating rate can be calculated from the slope of the fit dash line. In this case, the ion heating rate is 300 quanta/s.

electrode distance scaling, frequency dependence and temperature dependence due to different microscopic mechanisms. Thus investigating how ion heating behaves when ion-electrode distance, secular frequency and temperature are changed becomes important.

The ion-electrode distance dependence can be tested by using traps with different ion heights. In our experiments, the widths of the RF and the center ground electrodes are varied to get ion heights of 75 μm, 100 μm and 150 μm. However, this test scheme has its limitation, since different traps are involved. Traps must be microfabricated strictly following the same fabrication process to get rid of the excess ion heating due to factors that are affected by fabrication details.

The measurement of the frequency dependence is carried out by varying the ion trap secular frequency. However, the experimentally accessible secular frequency range is narrow since ions have to be trapped inside the stability region of the Math-

ieu's equation.

The temperature dependence of the ion heating is conducted in a cryogenic testing apparatus to provide a wide temperature range from cryogenic temperature 6 K to 100 K. Ion heating rate can also be measured in a room temperature setup at room temperature. In order to calibrate the temperature of the ion trap, RuO_2 temperature sensors are mounted on the trap surface using solder paste. Heating resistors are also mounted on trap surface to heat the trap by applying a current.

5.2 Gold Traps

Gold traps are fabricated by electroplating 1.2 μm thick soft gold onto 300 nm silver seed layer, followed by silver seed layer removal in the electrode gap. The electroplated gold has polycrystalline structure. The grain size can be mainly controlled by plating bath temperature, agitation and plating current density. Our gold electroplating is conducted in a TSG-250 bath that is set to 130 F with a 400 rpm agitation. The electroplating current is 1 mA/cm^2.

The average grain size for this electroplating condition is calculated from the residual resistance ratio measurement assuming the gold is pure. A rectangular gold wire is fabricated on the ion trap substrate within the same ion trap fabrication process. The resistance of the gold wire is measured both at cryogenic temperature and at room temperature. The residual resistance ratio (RRR) of our electroplated gold wire is

$$RRR = \frac{\rho_{300K}}{\rho_{0K}} \approx \frac{\rho_{300K}}{\rho_{6K}} = \frac{3.7\Omega}{0.2\Omega} = 18.5 \tag{5.3}$$

The RRR of pure gold is approximately 100 [Mat79]. According to Equation 4.13 [AM70], at 6 K

$$\frac{\rho_i}{\rho_{grain}} \approx \frac{RRR_{electroplated}}{RRR_{pure}} = 1 - \frac{3}{2}\alpha + 3\alpha^2 - 3\alpha^3 \ln(1 + \frac{1}{\alpha}) = \frac{18.5}{100} \tag{5.4}$$

Thus $\alpha = \frac{\lambda}{g}\frac{R}{1-R} = 3.25$. At 6 K, taking mean free path $\lambda = 4$ μm and reflection coefficient $R = 0.2$ [AM70], the average grain size $g = 307$ nm assuming the gold is

pure.

Three traps are fabricated with ion-electrode distance of 75 μm. The Sr^+ ion is loaded by photonionization of a neutral strontium vapor. The noisy electric field spectrum is approximately 6×10^{-14} $V^2/m^2/Hz$ [Lab08] at cryogenic temperature 6 K.

In order to investigate the temperature dependence of the ion heating, two RuO_2 temperature sensors are mounted at the trap surface on the opposite side of the trap to monitor the ion trap surface temperature. The temperature calibration uncertainty is within 2%. 1 KΩ heating resistor is also soldered at the edge of the trap to control the temperature ranging from 6 K to 120 K. The typical temperature dependence is shown in Figure 5-2.

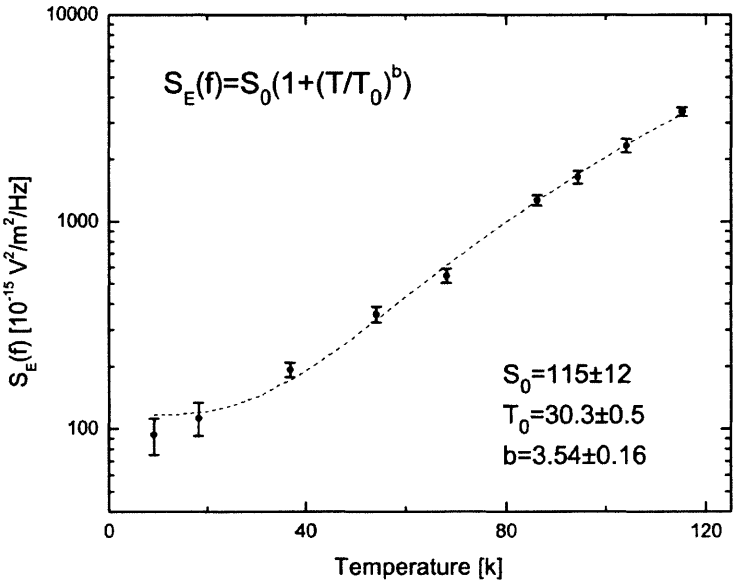

Figure 5-2: Temperature dependence of the noisy electric field spectrum of 75 μm electroplated gold trap II.

When temperature is below $T_0 = 30$ K, electric field noise spectrum varies slowly. The noise field increases rapidly above that point fitting to a polynomial of temperature T. Debye temperature needs to be taken into account when dealing with phonons. Metal gold has a Debye temperature $\Theta_D = 170$ K. Debye temperature is the temperature at which the highest-frequency mode is excited. The typical temperature

dependence of the contribution of phonons to the heat capacity is shown in Figure 5-3. When the heat capacity is $\frac{1}{e}$ (37%) of its maximum value, $\frac{T}{\Theta_D} = 0.2$. In the case of gold, $T = 34$ K. Above that temperature, phonon number increases rapidly. As discussed in Section 4.2.2, the dipole fluctuation is related to a phonon assisted surface adsorption state switching. As the phonon number increases rapidly, the phonon number involved in surface adsorption state switching also increases. The phonon number increases in a polynomial way, so does the electric field noise spectrum.

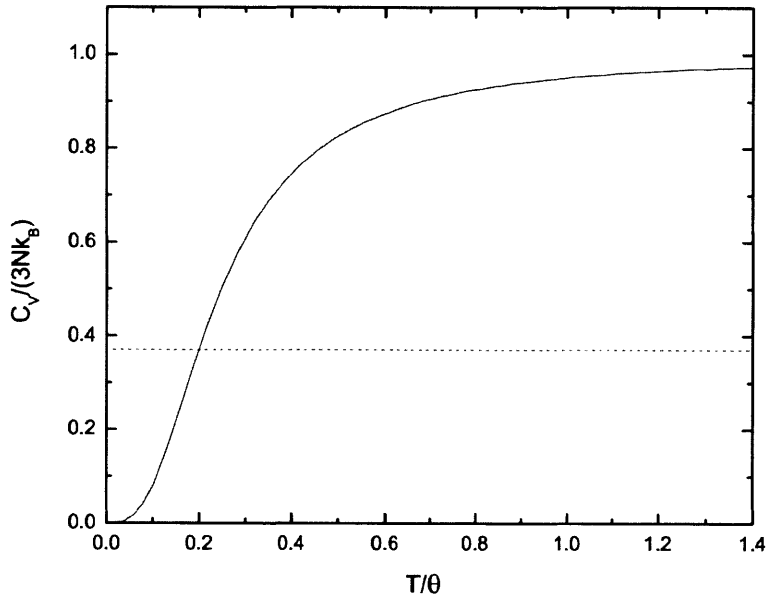

Figure 5-3: Temperature dependence of the heat capacity of solids. Θ_D is the Debye temperature. When the capacity is $\frac{1}{e}$ (37%) of its maximum value, $\frac{T}{\Theta_D} = 0.2$.

Below T_0, 75 μm electroplated gold trap I even has a slightly decreasing $S_E(f)$ when temperature increases as shown in Figure 5-4. When the temperature $T \leq \Theta_D/10 \approx 17$ K, thermally excited phonon number is small and the phonon-phonon scattering is dominant. As the temperature and phonon number slightly increase, the phonon-phonon scattering also increases. Thus the phonon number involved in the surface dipole fluctuations slightly decreases with increasing temperature, which

is observed in Figure 5-4 in the temperature range of 10 K to 17 K.

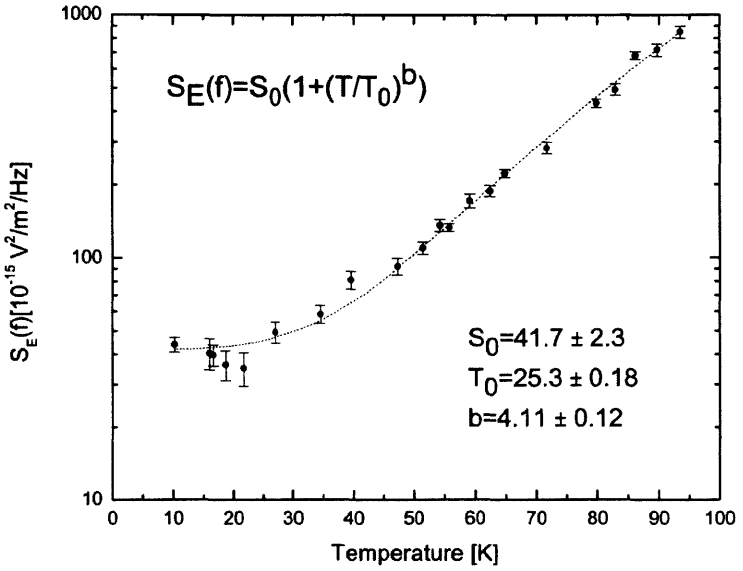

Figure 5-4: Temperature dependence of the noisy electric field spectrum of 75 μm electroplated gold trap I. $S_E(f)$ slightly decreases in the range $T \leq \Theta_D/10 \approx 17$ K. The electric field noise spectrum can be fitted to $S_E(T) = S_0(1 + (T/T_0)^b)$.

When the temperature T is in the range $\theta_D/10 < T < \Theta_D$, the electric field noise spectrum can be fitted to $S_E(T) = S_0\left(1 + (T/T_0)^b\right)$. b varies between traps and between different temperature cycles on the same trap. Table 5.1 shows the summary of fitting parameters to $S_E(T) = S_0\left(1 + (T/T_0)^b\right)$ obtained from ion heating measurements on the same trap in different temperature cycles and from ion heating measurements on different traps.

The ion heating measurements from the initial cool down show that $b \approx 4$, which indicates $D(\bar{\epsilon}) \approx T^3$ in our dipole fluctuation model. As the temperature cycles go on without breaking the vacuum, both S_0 and T_0 decrease slightly, indicating that temperature cycles result in irreversible changes due to the internal strain or stress. The temperature cycles induce defects inside the metal. At cryogenic temperature 6 K, the increase of defects leads to a decrease in mean free path of phonons, thus the number of phonons that assist dipole fluctuations at the surface will be slightly reduced. In addition to the surface and grain boundaries, defects can also cause phonon softening which corresponds to a decrease in crystal symmetry. Softening

Trap	Fitting Parameters S_0 $[10^{-15}$ V^2/m^{2}Hz]	T_0 [K]	b	Notes
I	41.7 ± 2.3	25.3 ± 0.18	4.11 ± 0.12	Initial cooldown*
II a)	166 ± 7.4	33.7 ± 0.3	3.64 ± 0.15	Initial cooldown
b)	115 ± 12	30.3 ± 0.5	3.54 ± 0.16	Temperature cycle to 130 K
c)	53.5 ± 2.9	22.5 ± 0.27	3.16 ± 0.1	Temperature cycle to 340 K
d)	60 ± 3.8	14.9 ± 0.49	2.08 ± 0.12	Cleaning in lab solvents
e)	17.6 ± 2.9	11.2 ± 0.91	1.77 ± 0.1	Cleaning in lab solvents
III	$3.25 \times 10^3 \pm 40$	70.4 ± 0.25	3.2 ± 0.07	Following RT measurements

Table 5.1: Summary of the fitting parameters to $S_E(f) = S_0\left(1 + (T/T_0)^b\right)$ obtained from the ion heating measurements of electroplated gold traps at different temperatures. For comparison, $S_E(f)$ in all measurements are normalized to $S_E(1\text{ MHz})$. Electroplated gold Trap I shows an Arrhenius after cleaning in an ultrasonic bath.*

phonons at the surface, grain boundaries and defects are responsible for the Debye temperature decrease [WMT10]. Thus T_0 also decreases in temperature cycles.

Ion heating rates are also measured at room temperatures on electroplated gold trap III before the cryogenic measurements. Heating element is installed underneath the CPGA, giving a temperature range of 300 K to 400 K. The measured noise field is approximately $62.5 \pm 5 \times 10^{-12}$ V^2/m^2/Hz at 300 K and is approximately $66.5 \pm 5 \times 10^{-12}$ V^2/m^2/Hz at 350 K. The increased ion heating due to the 50 K temperature increase is within the measurement error, indicating that the ion heating saturates above Debye temperature, since every mode is excited and phonon density state truncates above Debye temperature.

Trap cleaning also leads irreversible changes to the ion heating measurement. All the electroplated gold traps we have tested show a temperature dependence fitting to $S_E(T) = S_0\left(1 + (T/T_0)^b\right)$ in the range of 6K to 100 K, except trap I. This trap also exhibited a typical temperature dependence before cleaning. However, after it has been cleaned in an ultrasonic bath, it exhibits a dramatically distinct behavior. The power spectral density of the electric field shows an Arrhenius behavior $S_0 + S_1 e^{-T_0/T}$ and cannot be fitted to a polynomial T^b. This abnormal temperature dependence could be explained by the dipole fluctuation model with a narrow range distribution of activation energies and relaxation times. Equation 4.35 indicates that the dipole

fluctuation spectrum shows an Arrhenius temperature dependence $e^{-\epsilon/k_BT}$. As shown in Fig 5-5, the noise field fits well to $S_0 + S_1 e^{-T_0/T}$, giving $T_0 \approx 40$ K and $S_0 \approx 2.3 \times 10^{-12}$ V^2/m^2/Hz. Thus the activation energy $\epsilon \approx 3.4$ meV. The cleaning process causes visible flakes on the surface as well as surface contamination with solvent residue as shown in Figure 5-6; however, the reason why the distribution of activation energies and relaxation times are narrowed is unclear.

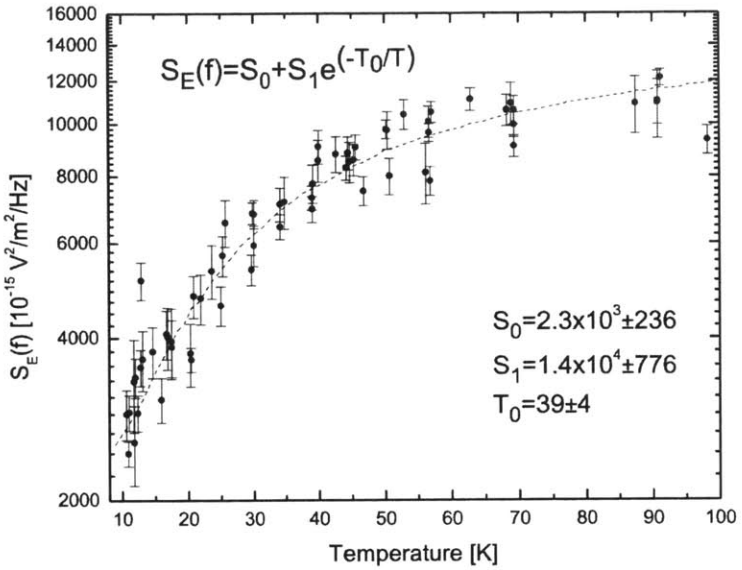

Figure 5-5: Arrhenius temperature dependence of the noisy electric field spectrum of 75 μm electroplated gold trap I after cleaning in an ultrasonic bath. The electric field noise spectrum can be fitted to $S_E(f) = S_0 + S_1 e^{-T_0/T}$.

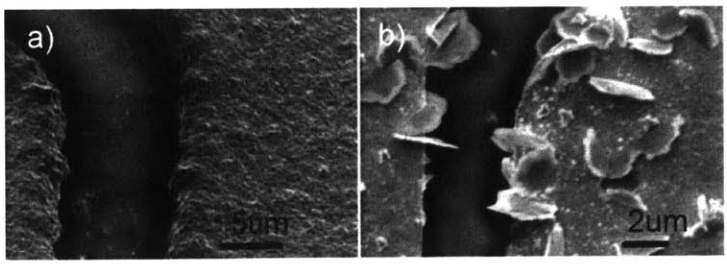

Figure 5-6: SEM photos of electroplated gold electrodes (a) before (b) after cleaning in an ultrasonic bath. After ultrasonication in lab solvents, some unknown flakes and surface contamination with solvent residue appear. Abnormal Arrhenius temperature dependence is observed.

Tests on the frequency dependence of the ion heating are also conducted at different temperatures in the cryogenic apparatus on 75 μm electroplated gold trap II as shown in Figure 5-7. The noise field has a frequency spectrum $f^{-\alpha}$. Equation 4.33 indicates that α has a weak temperature dependence. As discussed in Section 4.2.2, if distribution $D(\epsilon)$ is explicitly temperature dependent $D(\epsilon, T)$, frequency dependence α will deviate from 1 and

$$1 - \alpha(\omega, T) = \frac{1}{\ln(\omega\tau_0)} \left(\frac{\partial \ln S_p(\omega, T)}{\partial \ln T} - 1 \right) \tag{5.5}$$

will be nonzero. When the noise field spectrum $S_E(f)$ grows faster than T in the range $T > T_0$ ($T > 32$ K), $1 - \alpha > 0$. On the contrary, when $T < \Theta_D/10 \approx 17$ K and when T is approaching Debye temperature, $1 - \alpha < 0$. This is exactly what we have observed in Figure 5-7. At $T = 10$ K, $\alpha = 1.04 \pm 0.26$. At $T = 90$ K, $\alpha = 1.02 \pm 0.1$. $1 - \alpha < 0$. In the temperature range between them, $1 - \alpha > 0$. Our noise field temperature dependence and frequency dependence measurement results agree well.

5.3 Aluminium Traps

The aluminum traps are fabricated by the lift-off process. Before the lift-off, 400 nm aluminum is Ebeam evaporated onto the patterned quartz substrates. As mentioned in Section 4.3.1, aluminum forms a native passivation layer of oxide on top which is around $3 \sim 4$ nm. In order to investigate how the ion heating rate is affected by the amorphous dielectric metal oxide layer on top of the metal electrode, 5 nm, 10 nm and 20 nm aluminum oxide Al_2O_3 layers are Ebeam evaporated using an Al_2O_3 source at $1\mathring{A}$/s right after the aluminum evaporation without breaking the deposition vacuum (1×10^{-6} torr). The 400 nm Ebeam evaporated aluminum layer has an average grain size of $50 \sim 70$ nm [KB12].

The ion heating measurements are conducted in the cryogenic apparatus at 6 K. Single Sr^+ ion is also loaded by photonionization of a neutral strontium vapor. All tested aluminum ion traps have an ion-electrode distance of 100 μm.

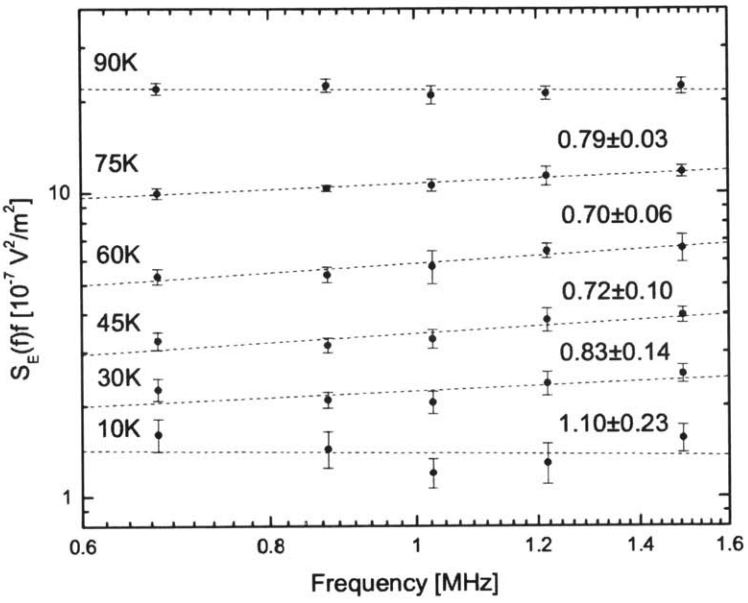

Figure 5-7: Frequency dependence of ion heating rate at different temperatures on 75 µm electroplated gold trap II. $S_E(f) \approx f^{-\alpha}$ thus $S_E(f) f \approx f^{1-\alpha}$. $1-\alpha$ corresponds to the slope of fitted lines.

Table 5.2 shows the summary of electric field noise of the aluminum traps with native oxide layer and with evaporated oxide layer of different thickness [Lac10].

At cryogenic temperature 6 K, aluminum ion traps Al-IIIb and Al-IIIc with native oxide layer have a noise field of approximately 1.1×10^{-14} V^2/m^2/Hz. Using the scaling d^{-4}, for an aluminum trap with ion-electrode distance of 75 µm, the electric field noise spectrum is scaled to 2.6×10^{-14} V^2/m^2/Hz, which is on the same order of magnitude as electroplated gold traps (6×10^{-14} V^2/m^2/Hz). Despite the existence of the native oxide layer, the aluminum traps perform as good as electroplated gold traps at cryogenic temperature.

However, the evaporated amorphous oxide layer does have effect on the ion heating rate. Although the 5 nm evaporated aluminum oxide layer has approximately the same thickness as the native oxide layer, the ion heating rate and the electric field noise have been increased by at least one order of magnitude. This is probably due to

Trap	$S_E(\omega)$ [10^{-15} V^2/m^{2}Hz]	Oxide
Al-IIIa	69.9 ± 10.5	Native oxide
Al-IIIb	10.6 ± 1.3	Native oxide
Al-IIIc	10.7 ± 1.3	Native oxide
$Al_2O_3 - 5$	540 ± 44	evaporated 5 nm oxide
$Al_2O_3 - 10$	$1.55 \times 10^3 \pm 173$	evaporated 10 nm oxide
$Al_2O_3 - 20$	$1.47 \times 10^3 \pm 100$	evaporated 20 nm oxide

Table 5.2: Summary of the electric field noise of the aluminum traps with native oxide layer and with evaporated oxide layer of different thickness. For comparison, $S_E(\omega)$ in all measurements are normalized to S_E (1 MHz). All tested aluminum ion traps have an ion-electrode distance of 100 μm.

the higher defect density in the evaporated aluminum oxide layer that can contribute to the density of tunneling two level systems ρ_{TLS}.

The oxide layer thickness dependence of the ion heating rate can be fitted to $1 - e^{-d/\delta}$ as shown in Figure 5-8. This result agrees with the model we have proposed in Section 4.2.2 on the excess electric field noise due to the presence of the amorphous dielectric layer. The power spectral density of electric field $S_E(\omega)$ is proportional to the surface dipole density ρ_s. With the presence of the thin amorphous dielectric layer, $S_E(\omega)$ is also proportional to ρ_{TLS}, the density of tunneling two level systems inside the dielectric layer. The probability for electrons of being trapped forming tunneling two level systems is proportional to $1 - e^{-\frac{d}{\delta}}$, where d is the thickness of the dielectric layer and δ is the characteristic length of the tunneling. When $d > \delta = 13$ nm, the electric field noise saturates.

5.4 Silver Traps

Silver traps are fabricated by chemical etching evaporated silver film, followed by annealing in oven under vacuum (1×10^{-5} torr) at 720°C to 760°C for one hour. The high annealing temperatures are necessary to reflow the silver and to smooth the electrode edges. The final thickness of the silver electrode is around 1 μm. The silver electrode surface morphology really depends on the annealing temperature. When annealed at 720°C, the silver electrode surface looks shiny with approximately 75%

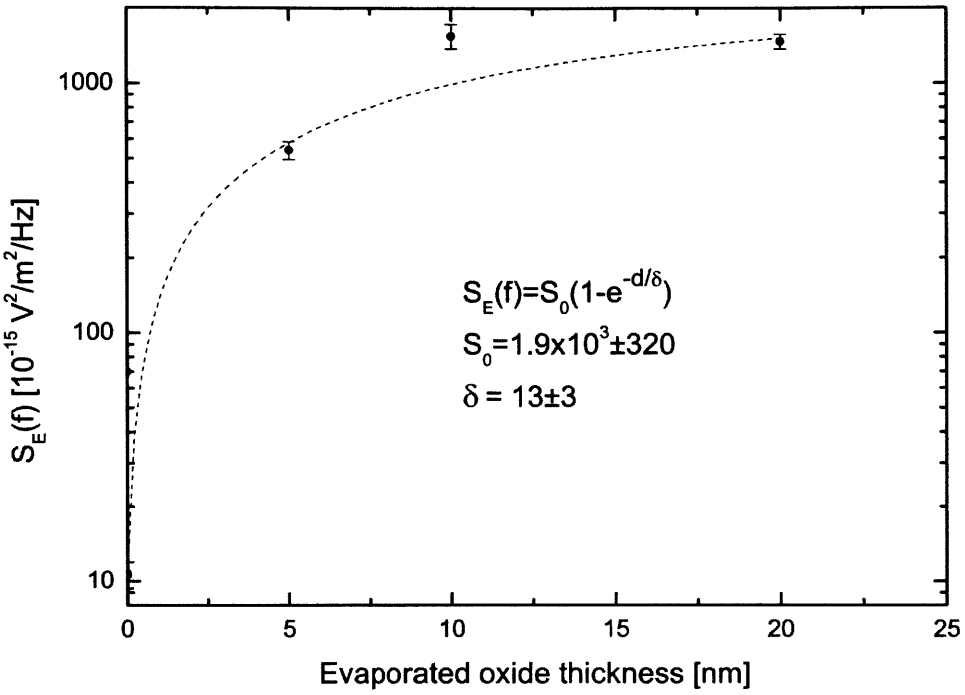

Figure 5-8: Electric field noise dependence on the evaporated oxide thickness. The three points at $d = 0$ correspond to the three aluminum traps with native oxide layer. The electric field noise spectrum can be fitted to $S_E(f) = S_0(1 - e^{-d/\delta})$.

reflection. However, the 760°C annealed one has a dull surface with only 5% reflection [Lab08]. As shown in Figure 3-10, recrystallization is observed on both 720°C and 760°C annealed silver surfaces. The 760°C annealed silver has slightly bigger grain than the 720°C annealed one, which agrees with the principle that grain grows during the recrystallization. The average grain size is seen to be $2 \sim 3$ μm from SEM photos. Silver annealing test is also done on sapphire substrates for comparison. However, the 760°C annealed silver on sapphire substrate is similar to the 720°C annealed one on quartz substrate, although sapphire substrate has better thermal conductivity than quartz substrate. This abnormal annealing behavior is due to the copper diffusion. Large amount of copper atoms have been observed to diffuse into the quartz substrate by changing the substrate color, when the silver trap sits directly on a copper oven during annealing at 760°C. The thermal conductivity of quartz substrate has been dramatically increased by copper diffusion. No obvious copper diffusion is observed in

quartz substrate of 720°C annealed silver. The sapphire substrate of 760°C annealed silver also has less amount of copper diffusion since diffusion becomes harder in densely packed sapphire crystal structure.

Seven traps are fabricated at different scales with ion-electrode distance of 75 μm, 100 μm and 150 μm. Four traps are annealed at 760°C and three are annealed at 720°C. Ion is loaded by the ablation of $SrTiO_3$ target. The ion heating measurement at cryogenic temperature 6K shows that the 720°C annealed silver traps have electronic field noise spectrum $2 \sim 3$ orders of magnitude higher than 760°C annealed ones with the same ion-electrode distance. The main difference in resistivity between these two annealed silver traps is from the surface scattering. As discussed in Section 4.2.1, the resistivity of the 760°C annealed silver is approximately 5 times larger than the 720°C annealed one, resulting in a larger thermal electric noise, which does not agree with our experiment result. It indicates that thermal electronic noise only has small contribution to the total ion heating, and patch potential noise plays the most important role. The patch potential noise is closely related to the patch size. The same order of magnitude of grain size in 760°C and 720°C annealed silver traps still cannot explain the 2 orders of magnitude difference in noisy electric field spectrum; however, it could possibly be explained by our model if grain orientation is taken into account.

As discussed in Section 4.2.2, $S_p(\omega) = \langle(\delta p)^2\rangle \frac{k_B T}{\omega} D(\bar{\epsilon})$ and the variance of dipole $\langle(\delta p)^2\rangle = \frac{1}{N}\left[\sum_{i=1}^{n} P_i p_i^2 - \left(\sum_{i=1}^{n} P_i p_i\right)^2\right]$. Different grain orientations will result in different surface work functions and corresponding different additional dipole potentials caused by adsorbates. To simplify the problem, we only investigate how grain orientations affect the variance of surface work function.

Evaporated silver films exhibit two primary crystalline grain orientations (111) and (100) [CVT95]. The work function is 4.46 eV for (111) and 4.22 eV for (100)[MC82]. Before annealing, with the presence of titanium as the adhesion layer, silver films have 100% (111) grain structure. During annealing, the (111) grain structure will gradually change to (100) grain structure. When the annealing temperature is higher than 260°C, for 1 μm thick silver film, after one hour annealing, approximately 50%

of (111) grain structure will change to (100) grain structure [SPB13]. For 720°C annealed trap, the possibility of (111) is $P_1^{(720)} \approx 0.5$ and the possibility of (100) is $P_2^{(720)} \approx 0.5$. For 760°C annealed trap, due to the copper diffusion in the quartz substrate, higher annealing temperature results in one dominant crystalline grain structure (100). Assume the grain size for 760°C and 720°C annealed traps are the same, and assume N are the same. According to our model, the possibility of grain with a particular orientation (111) affects the ion motional heating. For example, if we take $P_1^{(760)} = 0.0025$, $\frac{\langle(\delta p)^2\rangle_{720}}{\langle(\delta p)^2\rangle_{760}} \approx 100$. As long as $P_1^{(760)} < 0.0025$, the electric field noise could possibly differ by at least two orders of magnitude. The actual value of $P_1^{(760)}$ is unknown which can be tested by X-ray diffraction.

The ion heating rate measurement at room temperature is conducted on 760°C annealed silver traps with ion-electrode distance of 150 μm. The electric field power spectral density is approximately $15 \pm 5 \times 10^{-8}$ V^2/m^2/Hz. Using the d^{-4} scaling, the trap with ion-electrode distance of 75 μm has an electric field noise of $24 \pm 8 \times 10^{-7}$ V^2/m^2/Hz. For a 760°C annealed silver trap with ion-electrode distance of 75 μm, the noisy electric field spectrum is approximately 6×10^{-12} V^2/m^2/Hz at cryogenic temperature. The ion heating rate is approximately reduced by 6 orders of magnitude when cooled from room temperature to cryogenic temperature.

Tests on the ion-electrode distance dependence of the ion heating rate are conducted on the four 760°C annealed traps at cryogenic temperature 6 K. As shown in Figure 5-9, it is hard to determine whether the scaling fits to d^{-2} or d^{-4}, since different traps are involved and ion heating rate difference cannot only be attributed to the ion-electrode distance.

5.5 Niobium Traps

The niobium trap is fabricated by the dry etching process. 400 nm niobium is DC magnetron sputtered onto a sapphire substrate. After lithography, RIE with CF_4 and O_2 is used to dry etch the electrode gap. The 400 nm sputtered niobium layer has an average grain size of $30 \sim 100$ nm [GMS95] depending on the sputtering condition.

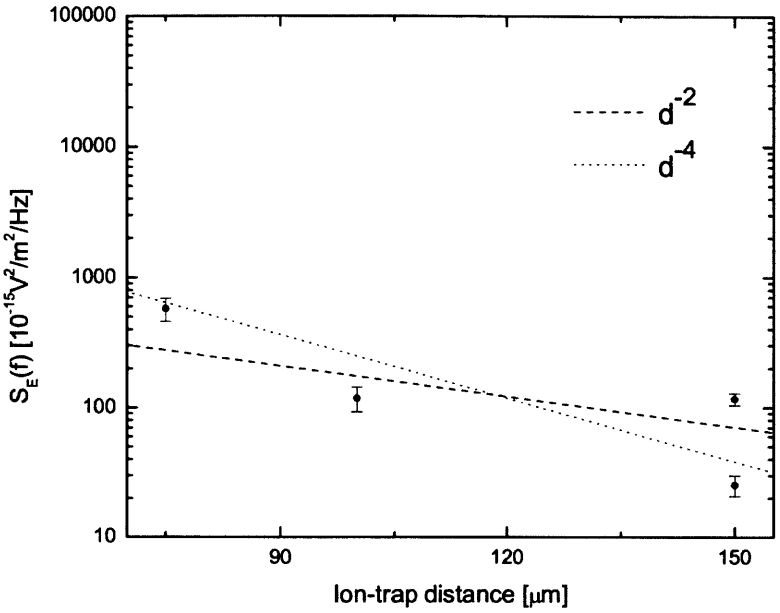

Figure 5-9: The ion-electrode distance dependence of the ion heating rate on four 760°C annealed silver traps. It is hard to determine whether the scaling fits to d^{-2} or d^{-4}.

The tested niobium ion trap has an ion-electrode distance of 100 μm. The ion heating measurements are conducted in the cryogenic apparatus at 6 K. The noisy electric field spectrum $S_E\,(1\text{ MHz})$ is approximately $25 \pm 4 \times 10^{-15}$ V^2/m^2/Hz.

5.6 Discussion

The heating rates at cryogenic temperature 6 K for Au, Ag, Al, Nb ion traps are listed in Table 5.3 for comparison. $S_E\,(f)$ in all measurements are normalized to $S_E\,(1\text{ MHz})$. Using the d^{-4} scaling, all the heating rates are corresponding to the ion-electrode distance of 75 μm.

As shown in Table 5.3, for gold, aluminum, and niobium traps, both ion heating rates and grain sizes are within the same order of magnitude. However, for the evaporated silver traps with annealing at 760°C, the grain size is one order of magni-

Trap	$S_E(\omega)$ $[10^{-15}\ \mathrm{V^2/m^2Hz}]$	Grain size
Electroplated gold	60	307 nm
Evaporated silver with annealing at 760°C	6×10^2	2 μm
Evaporated silver with annealing at 720°C	4×10^4	2 μm
Evaporated aluminum	26	$50 \sim 70$ nm
Sputtered niobium	80	$30 \sim 100$ nm

Table 5.3: Summary of the electric field noise of the electroplated gold traps, evaporated silver traps with annealing at 760°C and at 720°C, evaporated aluminum traps and DC sputtered niobium trap. For comparison, $S_E(\omega)$ in all measurements are normalized to S_E (1 MHz). Using the d^{-4} scaling, all the heating rates are corresponding to the ion-electrode distance of 75 μm.

tude bigger. The total number of grains would be two orders of magnitude smaller. According to $\langle(\delta p)^2\rangle = \frac{1}{N}\left[\sum_{i=1}^{n} P_i p_i^2 - (\sum_{i=1}^{n} P_i p_i)^2\right]$, the electric field noise could possibly be two orders of magnitude higher, which is consistent with what we have observed in our measurements.

In conclusion, our extended patch potential model for ion motional heating dependence on grain size and grain orientation is suitable to explain the ion heating behaviors we have observed in our measurements. Since patch potential is a surface phenomenon, it is determined by the grain orientation, patch size, surface adsorption, surface oxidation and surface contamination which are strongly related to the fabrication process. By dealing with suitable fabrication process, the excess ion heating could possibly be suppressed.

Grain size and grain orientation are possibly two factors affecting ion heating rate, which have not been investigated before. According to the extended patch potential model we have proposed in Section 4.2.2, there could be several ways to suppress the ion heating. One possible way is to increase the total number of grains N. In fabrication process, for thin film, vapor deposition of metal at lower temperature can reduce the grain size increasing N. When electroplating is chosen to deposit thick film, pulse electroplating with high current density will reduce grain size. As for the deposition method, sputtering will achieve smaller grains than Ebeam evaporation. Another possible way is to properly choose electrode materials which have the same work function regardless of the grain orientations. For example, molybdenum could

be a promising candidate.

Trap cleaning also leads irreversible changes to the ion heating rate. Thus ultrasonic bath and solvent residues should be carefully avoided.

Chapter 6

Fabrication of Multilayer Ion Traps with SU8

The surface electrode linear Paul trap can be simplified to a symmetric surface electrode point Paul trap consisting of three concentric electrodes, which has the advantage of allowing ion height variation by applying two in phase RF potentials on separate RF electrodes [Kim09]. Thus it gives us an opportunity to study the ion heating rate scaling dependence systematically using the same trap. How to route the conducting wires to the concentric electrodes without flying wires is the main issue in the microfabrication of surface electrode point Paul trap. This chapter details the process of fabricating such a multilayer point Paul trap using SU8.

This chapter begins with the theory of surface electrode point Paul trap, followed by an ion height variation scheme proposed by Tony Kim [Kim09] in Section 6.1. A multilayer structure with SU8 is then introduced to solve the main concern of point Paul trap fabrication in Section 6.2. We present the challenges in the microfabrication of multilayer point Paul trap with SU8 and detail the fabrication process in Section 6.3. We finally use a fabrication flow diagram to summarize the fabrication process in Section 6.4.

6.1 Surface Electrode Point Paul Trap

The surface electrode linear Paul trap design can be simplified to a symmetric surface electrode point Paul trap. Compared to the five wires of alternating potentials lying in the same plane in the linear Paul trap design, the surface electrode point Paul trap consists of several concentric electrodes with varying widths. The outer ground electrode can be divided into four symmetric parts to which DC voltages are applied for better compensation. The electrode configuration for the point Paul trap is shown in Figure 6-1.

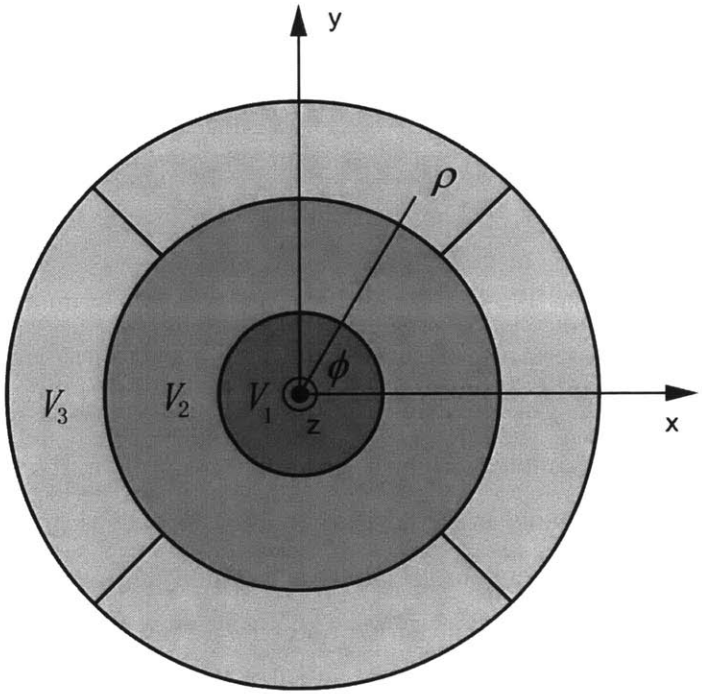

Figure 6-1: Schematic of a surface electrode point Paul trap with three concentric electrodes. The outer ground electrode is divided into four symmetric parts for better compensation via DC voltages.

For simplicity, we only consider the geometry of point Paul trap with three electrodes in a cylindrical coordinate system. z denotes the vertical direction, and ρ denotes the radial direction.

At $z = 0$, the boundary conditions are

$$\phi(\rho, 0) = \begin{cases} 0 & \rho < a \\ V\cos(\Omega t) & a \leq \rho \leq b \\ 0 & \rho > b \end{cases} \tag{6.1}$$

where V is the amplitude of the applied RF voltage, and Ω is the RF frequency. a and $b - a$ are the widths of the concentric electrodes.

In the $z > 0$ half space, the electric potential can be expanded to

$$\phi(\rho, z) = V\cos(\Omega z)\int_0^\infty e^{-kt} J_0(k\rho)\left[bJ_1(kb) - aJ_1(ka)\right]dk \tag{6.2}$$

where $J_0(k\rho)$ and $J_1(k\rho)$ are Bessel functions.

The ion height z_0 is given by

$$z_0 = \sqrt{\frac{b^{4/3}a^{4/3}}{b^{2/3} + a^{2/3}}} \tag{6.3}$$

The idea and implementation of ion height variation and radial translation in surface electrode point Paul trap were proposed by Tony Hyun Kim [Kim09]. Ion height variation is achieved by applying different amplitudes of RF potentials on separate electrodes. In the case of surface electrode point Paul trap with three electrodes, ion height variation is achieved by adding a RF voltage to the center previously grounded electrode.

At $z = 0$, the boundary conditions will change to

$$\phi(\rho, 0) = \begin{cases} \epsilon V\cos(\Omega t + \theta) & 0 < \rho < a \\ V\cos(\Omega t) & a \leq \rho \leq b \\ 0 & \rho > b \end{cases} \tag{6.4}$$

where ϵ and θ are the amplitude and phase difference between two RF electrodes.

A qualitative analysis is shown in Figure 6-2. Consider applying two in phase RF

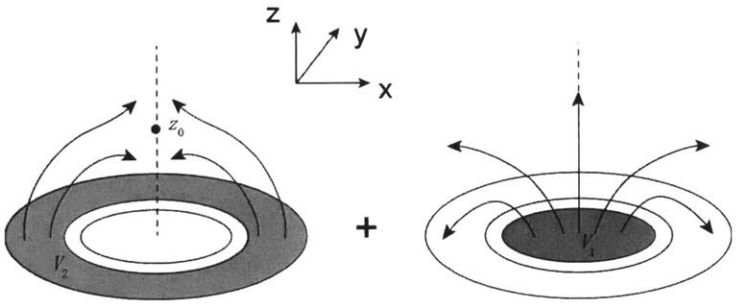

Figure 6-2: Schematic diagram of the superposition of electric fields generated by two RF electrodes. On the left side, the ring electrode generates a quadrupole potential with ion height z_0. On the right side, the center electrode generates electric field varying the ion height along z axis.

voltages to the two RF electrodes separately. As shown in Figure 6-2, when $z < z_0$, along the central trap axis, the electric field due to the outer RF ring has a different direction from the field due to the center RF electrode. When $z > z_0$, they have the same directions. Thus, the presence of the center RF electrode is to bring the RF node closer to the electrode surface. On the contrary, if two out of phase RF voltages are applied, the ion will be pushed away from the electrode surface.

By applying two different RF voltages to the center RF and the outer RF ring, the electric potential in Equation 6.2 will change to

$$\phi(\rho, z) = V\cos(\Omega t)\int_0^\infty e^{-kz} J_0(k\rho)\left[bJ_1(kb) - (1-\epsilon)\,aJ_1(ka)\right]dk \tag{6.5}$$

Taking the derivative of Equation 6.5, ion height z_0 is given by

$$z_0 = \sqrt{\frac{b^2a^{4/3}(1-\epsilon)^{2/3} - a^2b^{4/3}}{b^{4/3} - a^{4/3}(1-\epsilon)^{2/3}}} \tag{6.6}$$

Ion height can easily be varied by choosing different ϵ.

Thus, this surface electrode point Paul trap with three electrodes has the advantage of allowing ion height variation without introducing excess micromotions. This can give one an opportunity to study the ion heating rate scaling dependence systematically using the same trap, which can rule out those factors affected by fabrication

processes.

6.2 Multilayer Structure of Surface Electrode Point Paul Trap and Trap Design

As shown in Section 6.1, the surface electrode point Paul trap can have better control over the trapped ion due to it symmetric geometry. However, this symmetric geometry can cause a packaging problem. For the surface electrode linear Paul trap, the RF and ground electrodes are wire bonded at the ends of the electrodes, which are far away from the trapping center area. In the case of point Paul trap, the linear RF and ground electrodes are replaced by the concentric electrodes. If wires are directly wire bonded from the concentric electrodes to the CPGA pads, they will easily get in the way of cooling and manipulating lasers. In addition, the electric fields from the conducting wires are non-symmetric, which results in excess micromotions of the trapped ion. Thus how to route the conducting wires to the concentric electrodes without flying wires is the main concern of point Paul trap fabrication.

A multilayer structure is the solution to this question. A printed circuit board gives us a good example of this multilayer structure. Double-sided boards use vias to connect traces on opposite sides of the substrate. The substrate is a dielectric insulating layer. Conducting layers are normally made of thin copper foils. Bond thin copper foils on both sides of the substrate, pattern them with photoresist and then etch them to get desired copper traces. Plated through holes are used to connect copper traces on opposite sides. Figure 6-3 shows the Eagle design that we sent to Hughes Circuits Company for a surface electrode point Paul trap [Kim09].

There are several different dielectrics that can be chosen as the insulating substrate. The PCB boards we ordered from Hughes Circuits use Rogers as the low-loss dielectrics, and a mechanical drilling procedure is used to get through holes for vias. Lucent and Sandia groups [Sti07] use the PECVD grown silicon oxide, and use plasma-thermal inductively coupled plasma to etch through accordingly.

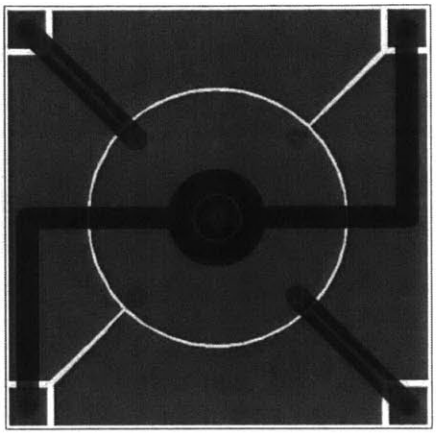

Figure 6-3: Eagle design that we sent to Hughes Circuits Company for a surface electrode point Paul trap. The electrodes on the top side are in red, the vias are in green and the copper traces on the bottom side are in blue.

Here, we describe the use of cured SU8 layer as the insulating substrate. SU8 is an epoxy-based negative, near-UV photoresist. It was originally developed and patented by IBM to pattern high aspect ratio structures. Now it is widely used in the fabrication of microfluid devices and microelectromechanical systems (MEMS).

There are several advantages of choosing SU8 as the insulating substrate. The thickness of the SU8 layer can vary from 1 µm to 200 µm. It is easy to get the desired thickness simply by choosing proper SU8 series and controlling the spinning speed. However, in order to get a thick PECVD oxide insulating substrate, several layers of oxide have to be grown in sequence for stress relief. Through hole structure can be accurately achieved by exposing and developing, compared with the PCB implementation which is lacking in precise electrode definitions. PCB boards also have limitation in the smallest electrode spacing, for example the smallest electrode gap that Hughes Circuits could provide us is 75 µm.

In addition to the advantages of flexibility in layer thickness and good imaging capability, SU8 also has outstanding chemical and physical properties. When exposed, the long molecular chains of SU8 cross link causing the solidification of the material. Thus the highly cross-lined structure gives good chemical resistance. In addition, cured cross-lined SU8 has very low level of outgassing, enabling its application in

fabrication of ion traps tested at room temperature in ultra high vacuum system. The cured SU8 film has a volume resistivity of $2.8 \times 10^{16}\Omega$cm and a relative permittivity of 4.1 at 1GHz [Mic].

Figure 6-4 shows the mask design for the insulating SU8 layer and conducting electrodes and traces on both sides of it. Cross line structures are used for mask alignment.

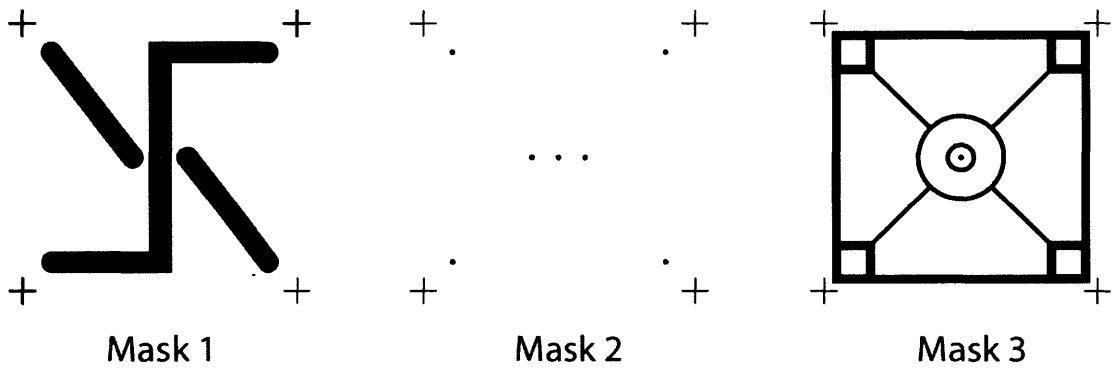

Figure 6-4: Mask design for the multilayer point Paul trap with SU8. Mask 1 is for the bottom layer conducting traces. Mask 2 is for the insulating SU8 layer. Mask 3 is for the top layer conducting electrodes. The center ground and concentric RF electrodes are routed to the pads on the four corners.

6.3 Multilayer Point Paul Trap with SU8 Fabrication Process

The idea of fabricating a multilayer trap with SU8 is inspiring; however, there are several challenges to the fabrication process. Since SU8 is a very viscous polymer, bubbles are often observed after coating or during prebake process. The bubbles in the insulating substrate will deteriorate the ion trap performance by changing electric field distribution. Efforts are also needed to reduce stress and cracking. Adhesion is another issue. Either the multilayer trap may need to be tested at cryogenic temperatures or be operated after baking the UHV system at 200°C for several weeks. Because both processes involve a large range of temperature, the thermal expansion

mismatch between SU8 layer and other materials makes it important to get a decent adhesion. Vias are also an issue. Due to the limited access to chemical-mechanical planarization (CMP) which is normally used after electroplating to make a vias, an alternative way to realize the vias is needed.

In this section we detail the fabrication process, including fabricating bottom layer electrodes, patterning SU8 layer and fabricating top layer electrodes. The efforts we have made to tackle those challenges are presented.

6.3.1 Bottom Layer Electrode

Bottom layer electrodes are fabricated on a single crystal quartz substrate. The quartz substrate is die saw cut and piranha cleaned for 15 min. We use the standard NR9-3000PY recipe to pattern the substrate with mask 1 shown in Figure 6-4 for bottom layer electrodes. After the lithography, lift-off is used to transfer the pattern. 300 nm silver and 10 nm titanium adhesion layer are evaporated onto the patterned quartz substrate by Ebeam-Au located in Technology Research Laboratory (TRL). The evaporation chamber pressure is 2×10^{-6} torr. The evaporation rate of titanium is 1Å/sec and the rate of silver is 3Å/sec. Lift-off is accomplished by immersing in acetone.

6.3.2 SU8 Application

SU8 negative photoresist has several series. Most of them use gamma butyrolactone as the primary solvent. They are produced for different thickness purpose. In our experiment, in order to get a 25 µm thick insulating spacer, we choose SU8-2025. The SU8-2000 series are different from other SU8 series by using cyclopentanone as solvent, and have improved properties.

As mentioned above, the existence of bubbles in the insulting SU8 layer will deteriorate the ion trap performance. Most of bubbles already exist in SU8 before its application on the substrate, especially small bubbles. The high viscosity of SU8 makes bubbles never be able to float out of the solution. In order to eliminate those

bubbles, SU8 is sealed in a small light-resistant brown bottle and baked in an oven at 70°C for one hour. The bottle must be well sealed to prevent the depletion of the solvent. The heat can reduce the viscosity enabling bubbles to rise out. Photoresist must be cooled to room temperature before opening the bottle. The pouring out process can also induce bubbles. Tests are conducted by pouring photoresist to a 1" × 1" quartz substrate at different heights. Results show that when the pouring height is smaller than 1 cm, bubble numbers can be greatly reduced. Tests also show that there still are bubbles which are created in the initial and the final application processes. Thus bubbles can mostly be eliminated by starting and ending the pouring out process outside of the substrate.

Prior to the SU8 application, substrate must be cleaned and dehydrated. Dehydration step is crucial to the adhesion of SU8 layer. Adhesion is checked by using the tape test. After evaluating different dehydration temperatures, dehydration times and rehydration times, it is found that different dehydration temperatures and times do not make significant difference as long as the substrate is dehydrated at a temperature higher than 150°C for more than 10 min. However, the rehydration time matters. If rehydration time is longer than 5 min, the tape test will fail on the developed SU8 layer.

In our experiment, we spin coat SU8-2025 at 500 rpm for 10 s, ramp up to spin speed 3000 rpm in 10 s and continue spinning for 50 s. We remove edge beads by using a squirt of acetone with a q-tip for better contact of the mask in later exposure. A 25 μm thick SU8 is achieved.

After photoresist application, the substrate with SU8 layer will be removed from the spinner and left on a flat room temperature surface for relaxation to improve uniformity.

6.3.3 Soft Bake

The purpose of a soft bake is to reduce the remaining solvent level in photoresist. A hotplate must be carefully leveled to achieve the photoresist layer uniformity. We soft bake the SU8-2025 in a two step baking process. We use the hotplate to soft bake,

since it provides a temperature gradient inside the thick SU8 layer, which helps the solvent diffuse and evaporate at the surface.

In order to avoid mask contamination and improve the photoresist adhesion, a long soft bake time is desired. However, when the soft bake time is too long, thermal cross-linking happens during baking, which results in a lower development rate and makes the through hole structure impossible. In addition, the very low solvent concentration makes the photoresist film brittle and easy to form cracks inside. After soft bake, wafer is cooled down slowly to reduce the retained stress.

After the soft bake, a rehydration step is required. Water is eliminated from SU8 film during the soft bake; however, a small concentration of water is necessary for a decent developing rate and a good contrast. For a thick SU8 film, it takes several hours for the water in air to diffuse toward the substrate.

Here are our working soft baking parameters. Bake wafer on the 65°C hotplate for 3 min then move it to a 95°C hotplate without cooling or stopping, for another 3 min soft bake. At the end of soft baking process, turn off the 95°C hotplate, let the wafer sit on the cooling 95°C hotplate for 2 min, at the end of 2 min, the temperature of the hotplate is 78°C. Then move the wafer back to the 65°C hotplate and bake for 1 min. Remove the wafer from the hotplate and place it on a level surface and allow it to relax from internal stress and to rehydrate for at least 10 hours.

6.3.4 Exposure

Negative SU8 photoresist is sensitive to 365 nm light and can be exposed with I-line. Exposure dose depends on the photoresist film thickness. Thicker film requires higher dose. Exposure dose is also related to the previous soft bake process, since long soft bake time results in low solvent concentrations which requires higher exposure dose. Different mask pattern requires different exposure dose. According to the design of mask 2 shown in Figure 6-4, the unexposed areas for vias get partially exposed by diffracting light from the nearby exposed areas. Thus longer development time is needed to make the through hole structure. Insufficient exposure can result in dissolving of resist and peeling of SU8 after development.

In our experiment, SU8-2025 is exposed with MA-4 which is calibrated to 9.3 mW/cm^2. Use hard contact and multi-exposure mode with mask 2. A total exposure time of 30 s is divided into 3 cycles of 10 s with a 30 s waiting time in between, which prevents an over heating of the photoresist by a high dose and allows the heat to dissipate away.

We also tried using a Heidelberg μ101 to do the exposure. Besides the difficulty in focusing due to the thickness of SU8 layer, N_2 formed during exposure will not be able to outgas due to the high light intensity, and it will form bubbles which cause a bumpy photoresist surface.

6.3.5 Post Exposure Bake

The purpose of post exposure bake is to cross link SU8's long molecular chains and to make them insolvable in the developer. The cross-linking process is first initiated during exposure and completed in post exposure bake step. When dealing with a thick photoresist layer, post exposure bake parameter window becomes smaller. Post exposure bake temperature and time need to be carefully handled. In order to reduce the residual stress and improve the adhesion, cooling scheme is necessary and can affect the photoresist pattern quality. Similar to the soft bake process, insufficient post exposure bake can results in dissolving of photoresist and bad adhesion. However, if it is over post exposure baked, the through hole structure can not be well developed. In addition, the photoresist film is more susceptible to cracks due to the low development rate.

Tests are done to test the effect of the cooling scheme. Without the cooling step, cracks can not be avoided after development. We need a slow and long cooling scheme to relief the stress; however, at the same time, a long cooling step will accompany an over post exposure bake.

Here are our working post exposure bake parameters. Bake wafer on the 65°C hotplate for 1 min then move it to the 95°C hotplate without cooling or stopping, for the 3 min post exposure bake. At the end of post exposure bake process, turn off the 95°C hotplate, let the wafer sit on the cooling 95°C hotplate for 2 min, at the end of 2 min, the temperature of the hotplate is 78°C. Then move the wafer back to the

65°C hotplate and bake for 1 min. Remove the wafer from the hotplate and place it on a level room temperature surface.

6.3.6 Development

We use 1-Methoxy-2-propanol acetate (PM Acetate) as developer. If wafer is soaked in PM Acetate for development, there will be a negative SU8 sidewall which is not good for vias purpose. To achieve a vertical sidewall, agitation is required in development. Agitation is carried out with spinner. During spinning, the centrifugal force will push the developer into the deep hole, thus through hole structure can achieve vertical sidewall.

Mount the wafer to the spinner. Spray PM Acetate to the wafer surface without spinning. Spin the wafer at 500 rpm for 30 s. Repeat the spray and spinning steps for 2 times. Rinse the wafer with Isopropanol to check whether it is completely developed. If there is still partially dissolved SU8 present, it will show a white milky color. Rinse with Isopropanol carefully and dry the Isopropanol with N_2 gun.

6.3.7 Hard Bake

Hard bake is the final cure step to solidify the remaining photoresist. It can further improve the adhesion. In our experiment, the final multilayer surface electrode point Paul trap will be baked at 200°C to achieve an ultra high vacuum. Thus a final hard bake temperature 250°C is used to ensure the stability of SU8 at 200°C. In addition, after the hard bake, the cured cross-lined SU8 will have very low level of outgassing.

6.3.8 Top Layer Electrode Sputtering

As shown in Section 3.3, there are two schemes to transfer the pattern of electrodes. One is lift-off and the other is etch. To do lift-off, lithography has to be done directly on SU8. Although SU8 is said to be chemically stable, development in KOH based developer RD6 can affect the adhesion of SU8 to substrate. Lithography test is done by using negative photoresist NR9-3000PY. Following the standard NR9-3000PY recipe,

after development, the adhesion between SU8 layer and the underneath bottom conducting layer is deteriorated. Although the SU8 layer is not peeled off, it can not pass the tape test. However, the etch scheme can somehow avoid this problem by adding a metal layer between the developer and the SU8 layer, which makes less KOH based developer diffuse inside to affect the adhesion. In addition, this metal layer can also work as a mask to prevent the underneath SU8 layer from the UV exposure in the lithography of the top layer electrodes. Thus for the top layer electrodes, metalization is done before the lithography.

For the top layer electrode metalization, either evaporation or sputtering can be used. As shown in Section 3.3.2, Ebeam evaporation evaporates source materials in a high vacuum which allows the vapor particle to reach the substrate without scattering. The vapor particles arrive at the substrate almost at the same angle, which results in a bad step coverage. Thus Ebeam evaporation is not appropriate for vias. On the contrary, sputtering is operated at a higher pressure. A plasma at higher pressure knocks the source material off the target. And these energetic atoms reach the substrate at random angles, which results in a better step coverage.

Aluminum is sputtered onto SU8 layer using the Sputter AJA located in Exploratory Materials Laboratory (EML). Before the sputtering starts, the system is purged with 12 sccm Ar gas for 3 min to significantly reduce the water concentration inside the chamber. After pumping for 45 min, the pressure goes to 2×10^{-5}torr. Set the Ar gas flow to 12 sccm, ignite the DC gun with the pressure mode 10 mtorr. Once the plasma is on, reduce the pressure to 3 mtorr and ramp up the power to 150 W. The sputtering rate is calibrated to $1.7\mathring{A}$/s. A total layer of 800 nm aluminum is sputtered onto the SU8 layer.

6.3.9 Top Layer Electrode Patterning and Dry Etch

For the top layer electrode, the lithography recipe is different from the standard NR9-3000P recipe due to the large topography structure. When spin coating on a topography structure, the photoresist on the hills is much thinner than the photoresist in the valleys. In our experiment, the photoresist inside the vias is much thicker than

on the rest of the area. The exposure dose that is sufficient for the pattern on the hills will be insufficient for the pattern in the valleys. Thus exposure dose should be increased to satisfy the needs of the pattern in the valleys, while the gap width of the mask to be exposed on the hills should be increased to compensate for the over exposure. Soft bake and post exposure bake times also need to be increased, since more heat is required in the valley areas. Longer baking and larger exposure dose result in longer development time. After the development, hard bake is conducted to achieve a better selective etch in the following dry etch step.

Due to the limited access to the reactive ion etching gas sources, aluminum is the most promising option. That is the reason why we choose aluminum as the top layer conducting material. Sputtered aluminum is dry etched in the right RIE chamber of the plasmatherm located in EML. A base pressure of 1×10^{-4} torr is achieved by turbo pump. Set gas flow BCl_3 = 5 sccm, gas flow Cl_2 = 5 sccm, and gas flow Ar = 3 sccm. When the chamber pressure is 5 mtorr, turn on the 50 W RF power. The dry etch rate of aluminum is 8.3$\mathring{A}$/s. Before starting the real RIE dry etch, do a 10 min dummy run using the same recipe without any samples to stabilize the process parameters.

6.4 Fabrication Summary

The fabrication process is summarized in the fabrication flow diagram shown in Figure 6-5. The bottom layer conducting traces are made of evaporated silver with titanium as the adhesion layer on the single crystal quartz substrate using lift off. The 25 µm thick cured SU8 layer works as the insulating layer with through holes made by lithography. Aluminum is then sputtered on top of the SU8 layer, achieving the vias and top conducting layer. The top layer electrode is then patterned by lithography and dry etched by RIE. Figure 6-6 shows the optical picture of a multilayer surface electrode point Paul trap made with SU8.

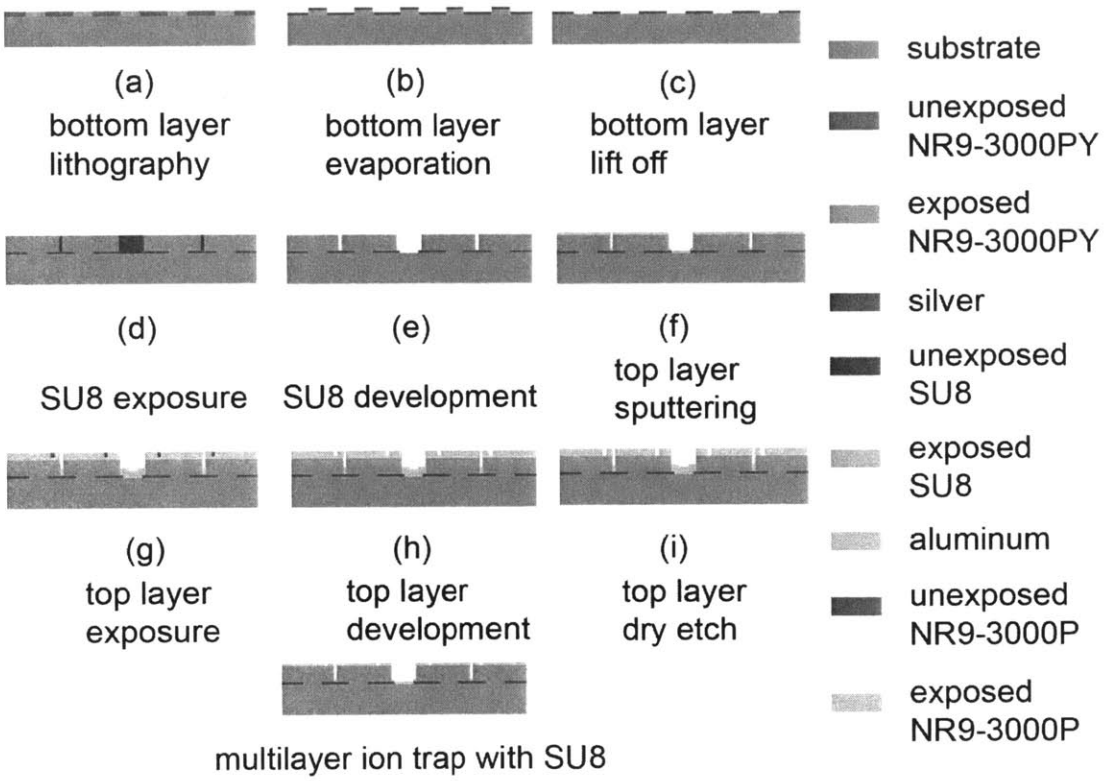

Figure 6-5: Fabrication flow diagram of a multilayer surface electrode point Paul trap with SU8.

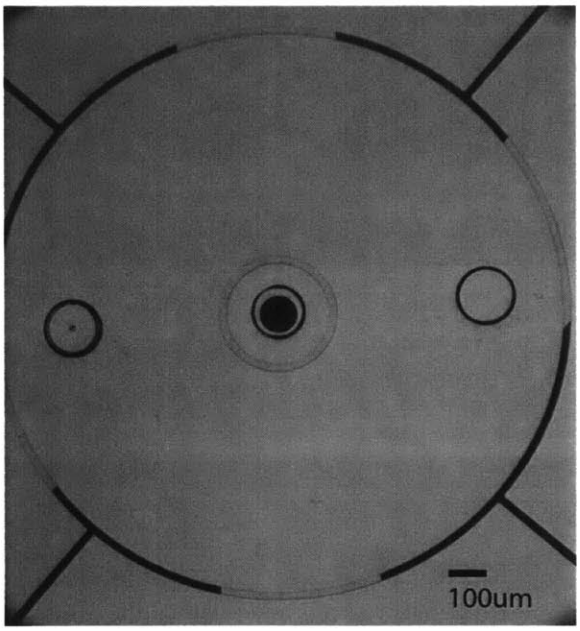

Figure 6-6: Optical picture of a multilayer surface electrode point Paul trap with SU8. The center dark circle is clear for optical access. The three equal size holes are vias. The middle one is connecting the center ground electrode to the bottom layer conducing trace. The other two are connecting the RF electrode.

Chapter 7

Conclusions and Future Work

Trapped ion quantum computers use the superposition of the atomic state and quantum motional state to encode information, and use laser-ion interactions to manipulate the qubit state. Thus the decoherence of the quantum motional state needs to be suppressed to preserve the superposition state necessary for the quantum computing. A lot of research has been done on the heating sources of the motional state caused by the fluctuating electric field.

This thesis presents the detailed fabrication of several series of surface electrode linear Paul traps made from different electrode materials, followed by the ion motional heating experiment results of these traps. This thesis asserts that the fluctuating patch potential model is suitable to explain the ion motional heating behavior, and since the patch potential is a surface phenomenon, it is determined by the grain orientation, patch size, surface adsorption, surface oxidation and surface contamination which are strongly related to the fabrication process. By dealing with proper fabrication process, the excess ion heating can potentially be suppressed.

To study the material dependence of the ion motional heating rate, we fabricated gold, silver, aluminum and niobium traps and subjected them to different fabrication process. Gold traps are DC electroplated on silver seed layer with titanium as the adhesion layer on single crystal quartz substrate. Silver traps are Ebeam evaporated and then chemical wet etched. The final silver traps are annealed at 720°C and 760°C in vacuum. Aluminum traps are Ebeam evaporated and use lift-off tech-

nique. Aluminum oxide of various thickness are purposely deposited within the same evaporation process. Niobium traps are sputtered and then RIE dry etched. These different fabrication processes for different electrode materials result in various surface morphology and grain structure.

Ion motional heating rate measurements are then conducted both at cryogenic temperature and at room temperature. We extended the fluctuating patch potential theory to explain the ion heating behavior taking grain structure and surface oxidation into account. For gold traps, we studied the temperature dependence of ion heating by varying temperature in ranges of 6 K to 120 K and 300 K to 400 K. We also studied the frequency dependence of of ion heating at different temperatures. For silver traps, we found that silver traps annealed at 720°C and 760°C can have the electric field noise differ by two orders of magnitude due to the different surface grain structure. For aluminum traps, we found that the electric field noise saturates when the thickness of the amorphous dielectric layer is larger than the characteristic length of the tunneling.

In conclusion, we found grain size is a factor that potentially affects ion motional heating rate, which has not been investigated before. This provides directions for future work. To study the grain size effect on the ion motional heating, one can fabricate gold traps by DC electroplating at different current densities. Small plating current will result in larger grain size. With pulse electroplating, fine grain size can be achieved. To study the grain orientation effect, molybdenum can be a promising candidate for electrode material which has same work function regardless of the grain orientations.

We also studied the ion-electrode distance dependence by using traps with different ion heights. However, this test scheme has its limitation, since different traps are involved. Traps must be microfabricated strictly following the same fabrication process to get rid of the excess ion heating due to factors that are affected by fabrication details. In the second part of this thesis, we introduced a surface electrode point Paul trap which has an advantage of varying ion height by applying two in phase RF potentials on separate RF electrodes [Kim09]. We presented a process for

fabricating such a multilayer point Paul trap using SU8. This work could shed new light on the fabrication of ion traps by taking advantages of modern microfabrication technologies.

Bibliography

[AGWK99] P. H. Eberhard A. G. White, D. F. V. James and P. G. Kwiat. Non-maximally entangled states: Production, characterization, and utilization. *Phys. Rev. Lett.*, 83:3103, 1999.

[AM70] M. Shatzkes A.F. Mayadas. Electrical-resistivity model for polycrystalline films: The case of arbitrary reflection at external surfaces. *Physics Review B*, 1:1382, 1970.

[ASNS11] P. F. Weck A. Safavi-Naini, P. Rabl and H. R. Sadeghpour. Microscopic model of electric-field-noise heating in ion traps. *Phys. Rev. A*, 84:023412, 2011.

[Bak06] W. Bakr. Towards a cryogenic planar ion trap for $Sr-88$. Master's thesis, Massachusetts Institute of Technology, Cambridge, MA, 2006.

[Bat67] George Batchelor. *An Introduction to Fluid Dynamics.* Cambridge University Press, Cambridge, UK, 1967.

[BCL+07] K. R. Brown, R. J. Clark, J. Labaziewicz, P. Richerme, D. R. Leibrandt, and I. L. Chuang. Loading and characterization of a printed-circuit-board atomic ion trap. *Phys. Rev. A*, 75:015401, 2007.

[Ber02] D. J. Berkeland. Linear paul trap for strontium ions. *Rev. Sci. Inst*, 73:2856, 2002.

[BKRB08] J. Benhelm, G. Kirchmair, C. F. Roos, and R. Blatt. Towards fault-tolerant quantum computing with trapped ions. *Nature Physics*, 4:463, 2008.

[BMB+98] D. J. Berkeland, J. D. Miller, J. C. Bergquist, W. M. Itano, and D. J. Wineland. Minimization of ion micromotion in a paul trap. *J. Appl. Phys.*, 83:5025, 1998.

[BOV+09] R. B. Blakestad, C. Ospelkaus, A. P. VanDevender, J. M. Amini, J. Britton, D. Leibfried, and D. J. Wineland. High-fidelity transport of trapped-ion qubits through an x-junction trap array. *Phys. Rev. Lett.*, 102(15):153002, 2009.

[BZ88] R. Blatt and P. Zoller. Quantum jumps in atomic systems. *European Journal of Physics*, 9:250, 1988.

[Cam97] Charles T. Campbell. Ultrathin metal films and particles on oxide surfaces: structural, electronic and chemisorptive properties. *Surface Science Reports*, 27:1, 1997.

[CBB+05] J. Chiaverini, R. B. Blakestad, J. Britton, J. D. Jost, C. Langer, D. Liebfried, R. Ozeri, and D. J. Wineland. Surface-electrode architecture for ion-trap quantum information processing. *Quantum Inf. Comput.*, 5:419, 2005.

[CDB91] J. B. Camp, T. W. Darling, and R. E. Brown. Macroscopic variations of surface potentials of conductors. *J. Appl. Phys.*, 69:7126, 1991.

[CFRB06] K. Kim M. Riebe C. F. Roos, M. Chwalla and R. Blatt. 'designer atoms' for quantum metrology. *Nature*, 443:316, 2006.

[CPO] Charged Particle Optics programs, www.electronoptics.com.

[CVT95] R. Carel C. V. Thompson. Texture development in polycrystalline thin films. *Materials Science and Engineering*, B32:211, 1995.

[Cya] Cyantek. http://www.cyantek.com/gold-etchants.php.

[CZ95] J. I. Cirac and P. Zoller. Quantum computations with cold trapped ions. *Phys. Rev. Lett.*, 74:4091, 1995.

[DBIW89] F. Diedrich, J. C. Bergquist, W. M. Itano, and D. J. Wineland. Laser cooling to the zero-point energy of motion. *Phys. Rev. Lett.*, 62:403, 1989.

[DDJ00] G. K. Brennen D. Deutsch and P. S. Jessen. Quantum computing with neutral atoms in an optical lattice. *Fortschritte der Physik*, 48:925, 2000.

[Deh67] H G Dehmelt. *Advances in Atomic and Molecular Physics, volume 3.* Academic Press Inc, New York, 1967.

[Deu89] D. Deutsch. Quantum computational networks. *Proc. Roy. Soc. London Ser. A*, 425:73, 1989.

[DGCH97] A. F. Fahmy D. G. Cory and T. F. Havel. Ensemble quantum computing by nmr spectroscopy. *Proceedings of the National Academy of Science*, 94:1634, 1997.

[DH81] P. Dutta and P.M. Horn. Low frequency fluctuations in solids: 1/f noise. *Rev Mod Phys*, 53:497, 1981.

[DHL+04] L. Deslauriers, P. C. Haljan, P. J. Lee, K-A. Brickman, B. B. Blinov, M. J. Madsen, and C. Monroe. Zero-point cooling and low heating of trapped 111cd+ ions. *Phys. Rev. A*, 70:043408, 2004.

[DHP13] A.C. Wilson D.T.C. Allcock D. Leibfried D.J. Wineland D.A. Hite, Y. Colombe and D.P. Pappas. Surface science for improved ion traps. *MRS Bulletin*, 38:826, 2013.

[DiV00] D.P. DiVincenzo. The physical implementation of quantum computation. *Fortschrite Der Physik-Progress of Physics*, 48:771, 2000.

[DOS+06] L. Deslauriers, S. Olmschenk, D. Stick, W. K. Hensinger, J. Sterk, and C. Monroe. Scaling and suppression of anomalous heating in ion traps. *Phys. Rev. Lett.*, 97:103007, 2006.

[EH05] K. Osuch E. Huger. Making a noble metal of pd. *Europhysics Letters*, 71:276, 2005.

[Fey82] R. P. Feynman. Simulating Physics with Computers. *Intl. J. Theor. Phys.*, 21:467, 1982.

[Flo83] Gaston Floquet. Sur les quations diffrentielles linaires coefficients priodiques. *Ann. Ecole Norm Sup.*, 12:47–88, 1883.

[Fut] Futurrex. http://futurrex.com/en/products/negative-photoresists.html.

[GC97] N. Gershenfeld and I. Chuang. Response to comment. *Science*, 277:1689, 1997.

[GJ91] C. Guet and W. R. Johnson. Relativistic many-body calculations of transition rates for Ca^+, Sr^+, and Ba^+. *Phys. Rev. A*, 44:1531, 1991.

[GMS95] S. Calatroni G. M. Schucan, C. Benvenuti. Niobium films produced by magnetron sputtering using an ar-he mixture as discharge gas. Proceedings of the 1995 Workshop on RF Superconductivity, 1995.

[Gro97] L.K. Grover. Quantum computers can search arbitrarily large databases by a single query. *Phys. Rev. Lett.*, 79:4709, 1997.

[Hou08] M. G. House. Analytic model for electrostatic fields in surface-electrode traps. *Phys. Rev. A*, 78, 2008.

[JBS90] W.P. Pratt J. Bass and P.A. Schroeder. The temperature-dependent electrical resistivities of the alkali metals. *Review of Modern Physics*, 62:645, 1990.

[JC71] D. L. Jacobson and A. E. Campbell. Molybdenum work function determined by electron emission microscopy. *Metallurgical and Materials Transactions B*, 2:3063, 1971.

[KB12] Horst-Gunter Rubahn Kirill Bordo. Effect of deposition rate on structure and surface morphology of thin evaporated al films on dielectrics and semiconductors. *Materials Science*, 18:3088, 2012.

[Kie96] D. Kielpinski. *Entanglement and Decoherence in a Trapped-Ion Quantum Register.* PhD thesis, University of Colorado, Boulder, Colorado, 1996.

[Kim09] T. Kim. An optical-fiber interface to a trapped-ion quantum computer. Master's thesis, Massachusetts Institute of Technology, Cambridge, MA, 2009.

[Kir07] E. Kirilov. *Development of Necessary Ion Traps, Vacuum and Laser Systems for photoionization, laser cooling and quantum state engineering of trapped Strontium ions.* PhD thesis, University of California, Los Angeles, Los Angeles, California, 2007.

[Lab08] J. Labaziewicz. *High Fidelity Quantum Gates with Ions in Cryogenic Microfabricated Ion Traps.* PhD thesis, Massachusetts Institute of Technology, Cambridge, MA, 2008.

[Lac10] Nathan S. Lachenmyer. Measurements of electric field noise and light-induced charging in al and cu surface electrode ion traps at cryogenic temperatures. Bachelor's Thesis, 2010.

[LDM+03] D. Leibfried, B. DeMarco, V. Meyer, D. Lucas, M. Barrett, J. Britton, W. M. Itano, B. Jelenkovic, C. Langer, T. Rosenband, and D. J. Wineland. Experimental demonstration of a robust, high-fidelity geometric two ion-qubit phase gate. *Nature*, 422:412, 2003.

[LGA+08] J. Labaziewicz, Y. Ge, P. Antohi, D. Leibrandt, K. R. Brown, and I. L. Chuang. Suppression of heating rates in cryogenic surface-electrode ion traps. *Phys. Rev. Lett.*, 100:013001, 2008.

[Lid05] David R. Lide. *CRC Handbook of Chemistry and Physics, 86th Edition.* CRC Press, New York, NY, 2005.

[Lid08] David R. Lide. *CRC Handbook of Chemistry and Physics, 89th Edition.* CRC Press, New York, NY, 2008.

[LKOW07] D. Leibfried, E. Knill, C. Ospelkaus, and D. J. Wineland. Transport quantum logic gates for trapped ions. *Phys. Rev. A*, 76:032324, 2007.

[LLC+09] D.R. Leibrandt, J. Labaziewicz, R.J. Clark, I.L. Chuang, R.J. Epstein, C. Ospelkaus, J.H. Wesenberg, J.H. Bollinger, D. Leibfried, D. Wineland, D. Stick, J. Stick, C. Monroe, C.-S. Pai, Y. Low, R. Frahm, and R.E. Slusher. Demonstration of a scalable, multiplexed ion trap for quantum information processing. *Quantum Inf. Comput.*, 9(11):0901, 2009.

[LWGS05] V. Letchumanan, M. A. Wilson, P. Gill, and A. G. Sinclair. Lifetime measurement of the metastable 4d $^2D_{5/2}$ state in $^{88}Sr^+$ using a single trapped ion. *Phys. Rev. A*, 72:012509, 2005.

[Mac47] Norman William MacLachlan. *Theory and Application of Mathieu Functions.* Clarendon Press, Oxford, 1947.

[Mad02] Marc J. Madou. *Fundamentals of Microfabrication: The Science of Miniaturization.* CRC Press, Boca Raton, FL, 2002.

[Mat68] Emile Mathieu. Mmoire sur le mouvement vibratoire dune membrane de forme elliptique. *Journal des Mathmatiques Pures et Appliques*, pages 137–203, 1868.

[Mat79] R. A. Matula. Electrical resistivity of copper, gold, palladium, and silver. *Journal of Physical and Chemical Reference Data*, 8:1147, 1979.

[Mat98] Donald M. Mattox. *Handbook of physical vapor deposition (PVD) processing.* Noyes Publications, Westwood, NJ, 1998.

[MC82] C H B Mee M. Chelvayohan. Work function measurements on (110), (100) and (111) surfaces of silver. *Journal of Physics C: Solid State Physics*, 15:2305, 1982.

[MDH11] J. A. Broersma W. K. Hensinger M. D. Hughes, B. Lekitsch. Microfabricated ion traps. *Contemporary Physics*, 52:6:505, 2011.

[MDRS12] S. E. Nigg L. Sun L. Frunzio S. M. Girvin M. D. Reed, L. DiCarlo and R. J. Schoelkopf. Realization of three-qubit quantum error correction with superconducting circuits. *Nature*, 482:382, 2012.

[Mic] Microchem.

[Mil93] H.C. Miller. Flashover of insulators in vacuum: review of the phenomena and techniques to improved holdoff voltage. *IEEE Transactions on Electrical Insulation*, 28:512, 1993.

[MMK+95] C. Monroe, D. M. Meekhof, B. E. King, W. M. Itano, and D. J. Wineland. Demonstration of a fundamental quantum logic gate. *Phys. Rev. Lett.*, 75:4714, 1995.

[MMK+96] D. M. Meekhof, C. Monroe, B. E. King, W. M. Itano, and D. J. Wineland. Generation of nonclassical motional states of a trapped atom. *Phys. Rev. Lett.*, 76:1796, 1996.

[MvdS99] H. J. Metcalf and P. van der Straten. *Laser Cooling and Trapping.* Springer-Verlag, New York, 1999.

[Neu55] J Von Neumann. *Mathematische Grundlagen der Quantenmechanik.* Springer, Berlin, 1955.

[NL71] W. Kohn N.D. Lang. Theory of metal surfaces: Work function. *Physics Review B*, 3:1215, 1971.

[NPT99] Y. Nakamura, Y. A. Pashkin, and J.S. Tsai. Coherent control of macroscopic quantum states in a single-Cooper-pair box. *Nature*, 398:786, 1999.

[Nyq28] H. Nyquist. Thermal agitation of electricity in conductors. *Phys. Rev.*, 32:110–113, 1928.

[Pau90] W. Paul. Electromagnetic traps for charged and neutral particles. *Rev. Mod. Phys.*, 62:531–540, 1990.

[PBIW96] M. E Poitzsch, J. C. Bergquist, W. M. Itano, and D. J. Wineland. Cryogenic linear ion trap for accurate spectroscopy. *Rev. Sci. Instr.*, 67:129, 1996.

[Per04] Nestor Perez. *Electrochemistry and corrosion science.* Kluwer Academic Plublishers, Boston, MA, 2004.

[PGCZ] T. Pellizari, S. A. Gardiner, J. I. Cirac, and P. Zoller. Decoherence, continuous observation, and quantum computing: A cavity qed model.

[Phi87] W. A. Phillips. Two-level states in glasses. *Reports on Progress in Physics*, 50:1657, 1987.

[PS53] W. Paul and H. Steinwedel. Ein neues massenspektrometer ohne magnetfeld. *Z. Naturforsch. A*, 8:448, 1953.

[RDG09] T. Coudreau R. Dubessy and L. Guidoni. Electric field noise above surfaces: A model for heating-rate scaling law in ion traps. *Phys. Rev. A*, 80:031402, 2009.

[RK10] Kashmiri L. Mittal Rajiv Kohli. *Developments in Surface Contamination and Cleaning: Particle Deposition, Control and Removal.* Elsevier, Oxford, UK, 2010.

[RO92] F. Rossi and G. I. Opat. Observations of the effects of adsorbates on patch potentials. *J. Phys. D*, 25:1349, 1992.

[Rog] Rogers.

[RZR+99] Ch. Roos, Th. Zeiger, H. Rohde, H. C. Nägerl, J. Eschner, D. Leibfried, F. Schmidt-Kaler, and R. Blatt. Quantum state engineering on an optical transition and decoherence in a paul trap. *Phys. Rev. Lett.*, 83:4713, 1999.

[SCR+06] S. Seidelin, J. Chiaverini, R. Reichle, J. J. Bollinger, D. Liebfried, J. Britton, J. H. Wesenberg, R. B. Blakestad, R. J. Epstein, D. B. Hume, J.D. Jost, C. Langer, R. Ozeri, N. Shiga, and D. J. Wineland. Microfabricated surface-electrode ion trap for scalable quantum information processing. *Phys. Rev. Lett.*, 96:253003, 2006.

[Sha48] C. E. Shannon. A mathematical theory of communication. *Bell System Technical Journal*, 27, 1948.

[Sho94] P. W. Shor. Algorithms for quantum computation: Discrete log and factoring. In S. Goldwasser, editor, *Proceedings of the 35th Annual Symposium on the Foundations of Computer Science*, page 124, Los Alamitos, CA, 1994. IEEE Computer Society.

[SHO+06] D. Stick, W. K. Hensinger, S. Olmschenk, M. J. Madsen, K. Schwab, and C. Monroe. Ion trap in a semiconductor chip. *Nature Physics*, 2:36, 2006.

[Son52] E.H. Sondheimer. The mean free path of electrons in metals. *Advances in Physics*, 1:1, 1952.

[SPB13] Lindsay Timian Adam Silvernail Elizabeth A. Ellis Shefford P. Baker, Brandon Hoffman. Texture transformations in ag thin films. *Acta Materialia*, 61:7121, 2013.

[Ste03] A. M. Steane. Overhead and noise threshold of fault-tolerant quantum error correction. *Phys. Rev. A*, 68:042322, 2003.

[Sti07] D. L. Stick. *Fabrication and Characterization of Semiconductor Ion Traps for Quantum Information Processing.* PhD thesis, University of Michigan, Ann Arbor, Michigan, 2007.

[TKK+00] Q. A. Turchette, D. Kielpinski, B. E. King, D. Liebfried, D. M. Meekhof, C. J. Myatt, M. A. Rowe, C. A. Sackett, C. S. Wood, W. M. Itano, C. Monroe, and D. J. Wineland. Heating of trapped ions from the quantum mechanical ground state. *Phys. Rev. A*, 61:063418, 2000.

[Tra] Transene. http://www.transene.com/aluminum.html.

[TST97] K.M. O'Hara T.A. Savard and J.E. Thomas. Laser-noise-induced heating in far-off resonance optical traps. *Phys Rev A*, 56(2):1095–1098, 1997.

[Tur36] A. M. Turing. On computable numbers, with an application to the entscheidungsproblem. *Proc. London Math. Soc.*, 42:230, 1936.

[War97] W.S. Warren. The usefulness of nmr quantum computing. *Science*, 277:1688, 1997.

[WB35] E. Wigner and J. Bardeen. Theory of the work functions of monovalent metal. *Physics Review*, 48:84, 1935.

[WI79] D. J. Wineland and W. M. Itano. Laser cooling of atoms. *Phys. Rev. A*, 20:1521, 1979.

[WMI+98] D. J. Wineland, C. Monroe, W. M. Itano, D. Leibfried, B. E. King, and D. M. Meekhof. Experimental issues in coherent quantum-state manipulation of trapped atomic ions. *J. of Res. of the National Inst. of Standards and Technology*, 103:259, 1998.

[WMT10] X. Zhang W. Ma and K. Takahashi. Electrical properties and reduced debye temperature of polycrystalline thin gold films. *Journal of physics D: Applied Physics*, 43:465301, 2010.